EXPERIMENTAL MEASUREMENTS OF FLUID MIXING AT THE SCALED UPPER PLENUM OF HIGH TEMPERATURE GAS COOLED REACTORS

A Dissertation

by

ANAS MOHAMMED F ALWAFI

Submitted to the Office of Graduate and Professional Studies of
Texas A&M University
in partial fulfillment of the requirements for the degree of

DOCTOR OF PHILOSOPHY

Chair of Committee,	Yassin A. Hassan
Co-Chair of Committee,	N.K. Anand
Committee Members,	Kalyan Annamalai
	Thien Nguyen
	Rodolfo Vaghetto
Head of Department,	Michael Nastasi

May 2021

Major Subject: Nuclear Engineering

ABSTRACT

The High Temperature Gas-cooled Reactor (HTGR) is one of the promising reactors in the Generation IV nuclear reactors. In this research, experimental measurements were done at $1/16^{th}$ scaled upper plenum of a HTGR that was scaled, designed and assembled at Texas A&M University. The goal was to investigate the flow mixing, thermal stratification and jet impingement in the upper plenum of HTGR under the Loss of Forced Coolant accident and provide high fidelity experimental database for validating CFD and system codes. Isothermal and non-isothermal cases were the primary investigation cases. Plumes—non-isothermal—will result in the formation of stratified layers with more uniform heat transfer, while jets—isothermal—will impinge on structures and have the potential to lead to more localized hot spots. Time-resolved particle image velocimetry (TR-PIV) and Planar laser-induced fluorescence (P-LIF) measurements were performed in the central plane of the jet/plume flow at the upper plenum. For the isothermal case, various jet Reynolds numbers ranging from 3,413 to 12,819 were performed, and for the non-isothermal case, one case was performed at total power of $0.4kW$. From the TR-PIV velocity snapshots, statistical characteristics of the jet/plume flow, such as the mean velocity, root-mean-square fluctuating velocity and Reynolds stress, were presented. Furthermore, two-point velocity cross-correlations, spectral analysis, and squared coherent functions were performed on the TR-PIV velocity vector fields. From the P-LIF temperature snapshots, a convergence of the statistical results was achieved, and the statistical results were calculated and profiles of the mean temperature were plotted.

DEDICATION

To the memory of my father who passed away during the beginning of my graduate journey.

To my great mother Amina.

To my lovely wife Sarah.

To my children Omar & Lina.

I am honored to dedicate this work to all of you.

ACKNOWLEDGMENTS

I would first like to thank my chair and advisor, Dr. Yassin Hassan. I learned a lot from his guidance and experience. It was a great honor to work with him. He was always available to share his knowledge and support my research work.

I would also like to thank my co-chair Dr. N.K. Anand for his support throughout my research. His critique and suggestions were valuable.

I would like to extend my acknowledgment to my committee member Dr. Thien Nguyen as he mentored me thru my research work.

Thanks to my colleagues in the Thermal-Hydraulics Research Laboratory for their help and support.

I also would like to thank my family for their encouragement and support during my study.

I would like to acknowledge my sponsor King Abdulaziz City for Science and Technology (KACST) for their financial support along with the Saudi Arabian Cultural Mission (SACM) in the USA.

CONTRIBUTORS AND FUNDING SOURCES

Contributors

This work was supported by a dissertation committee consisting of Dr. Yassin Hassan, Dr. Thien Nguyen and Dr. Rodolfo Veghetto of the Department of nuclear engineering and Dr. N.K. Ananad and Dr. Kalyan Annamalai of the Department of mechanical engineering.

All work conducted for the dissertation was completed by the student independently.

Funding Sources

Graduate study was supported by a scholarship from King Abdulaziz City for Science and Technology (KACST), Saudi Arabia.

NOMENCLATURE

ABWR	Advance Boiling Water Reactors
BWR	Boiling Water Reactor
CFD	Computational Fluid Dynamics
DCC	Depressurized Conduction Cooldown
HTGR	High Temperature Gas-cooled Reactor
LOCA	Loss-of-Coolant Accident
LOFA	Loss-Of-Reactor Core Accident
MHTGR	Modular High Temperature Gas Cooled Reactor
P-LIF	Planar Laser Induced Fluorescence
PCC	Pressurized Conduction Cooldown
PWR	Pressurized Water Reactors
RCCS	Reactor Cavity Cooling System
TR-PIV	Time Resolved Particle Image Velocimetry
V&V	Validation and Verification
D_j	jet diameter (mm)
N	number of samples
T	time-averaged temperature ($^{\circ}C$)
T_m	maximum local temperature ($^{\circ}C$)
U, V	horizontal and vertical time-averaged velocities (m/s)
V_c	maximum axial velocity (m/s)
V_m	maximum local axial velocity (m/s)
V_{avg}	mean flow velocity at the inlet of the jet (m/s)
${}^{k}L_x, {}^{k}L_y$	integral length scales (mm)
f	sampling frequency (Hz)
u', v'	horizontal and vertical fluctuating velocities (m/s)

u'_{rms}, v'_{rms}	root-mean-square fluctuating horizontal and vertical velocities (m/s)
x, y	horizontal (transverse) and vertical (axial) directions
$x_{1/2}$	jet half-width (mm)
$C_{xy}(f)$	squared coherent function between points x and y
$P_{xy}(f)$	power spectral density between points x and y
R_{uu0}, R_{vv0}	velocity-velocity spatial cross-correlation coefficients
R_{uu}, R_{vv}	velocity-velocity spatial-temporal cross-correlation coefficients
Re	jet Reynolds number
ϵ_N	absolute difference between the statistics
η	separation length (mm)
ν	kinematic viscosity of water (m^2/s)
τ	time delay (s)

TABLE OF CONTENTS

Page

LIST OF FIGURES

FIGURE Page

LIST OF TABLES

TABLE Page

1. INTRODUCTION [1]

Energy is essential to most people around the world. Without access to energy, most of the world would find it almost impossible to cope. As a result, energy demand and consumption are increasing rapidly. The U.S. Energy Information Administration (EIA) estimates a 50% increase in energy consumption by 2050 EIA [2019], as seen in Figure 1.1. This increase will require a large increase in energy production thus investment in building new power plants is important to meet this future demand. One of the potential options for decision makers to consider is nuclear power. The cost of nuclear power plants is competitive with other sources of power. While a large capital cost is requires to start up the plants, in the long run, it is cost-effective [WNA, 2008]. In addition to being cost-effective, nuclear power plants are one of the most environmentally friendly sources of energy. The plants do not produce direct carbon dioxide in contrast with fossil fuel plants which have negative impacts on the environments from the discharge of toxic gases [EIA, 2019]. Thus, many countries are turning to nuclear power as one of their energy sources. For example, the United Arab Emirates (UAE) just launched their first nuclear power plant in Barakah which will supply up to 25% of the UAE power production. Moreover, Saudi Arabia, with one of the largest oil reserves in the world, is negotiating the building of two nuclear reactors with a capacity of 17 GWe each [WNA, 2019].

[1] Part of the data reported in this chapter is reprinted with permission from "Time-resolved particle image velocimetry measurements of a single impinging jet in the upper plenum of a scaled facility of high temperature gas-cooled reactors" by Anas Alwafi, Thien Nguyen, Yassin Hassan, and N.K Anand, 2019. International Journal of Heat and Fluid Flow, 76, 113-129, Copyright 2019 by Elsevier.

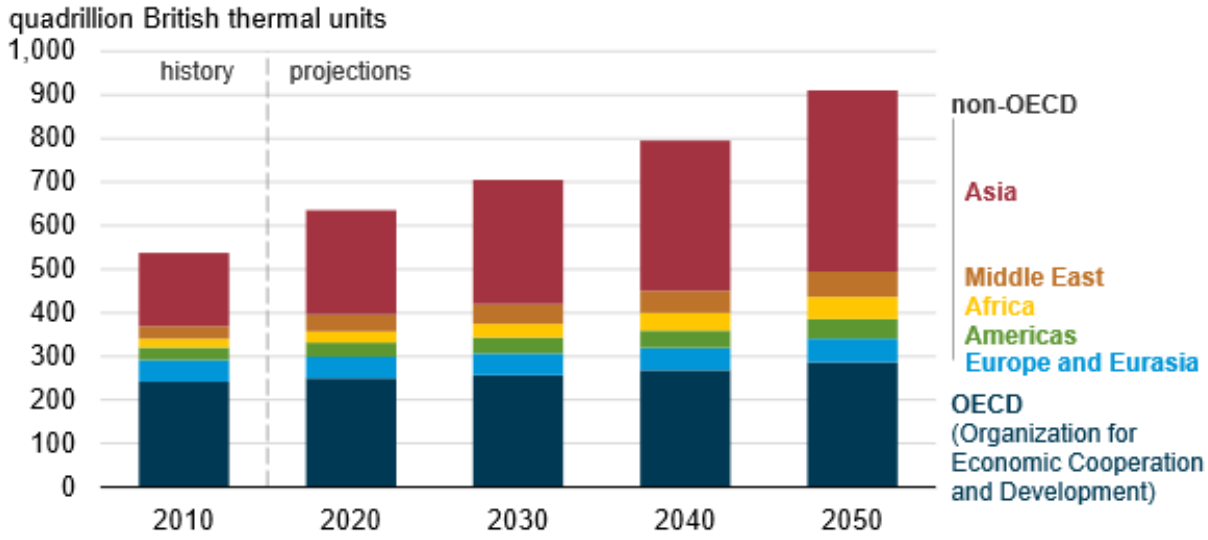

Figure 1.1: Estimation of the global energy consumption by region from 2020 to 2050, reprinted from [EIA, 2019]

1.1 Generation IV nuclear energy systems

The first nuclear reactor was built at the university of Chicago in 1942, and 8 years after that, in 1950, the EBR-1 reactor, considered a prototype, was the first reactor to generate electricity. During the 1970s and 1980s, commercial nuclear power plants were built to generate electricity in several countries. Reactor types including Boiling Water Reactors (BWR) and Pressurized Water Reactors (PWR). BWR and PWR are considered Generation II reactors and the majority of the currently operational reactors are one of those two. The development of nuclear reactors does not stop there. The Advance Boiling Water Reactor (ABWR) is one of the Generation III reactors developed. Currently, Generation IV reactors are the future of nuclear reactor science. Figure 1.2 shows the history and the evolution of nuclear power reactors [NIRS, 2016].

In December 2002, the U.S. Nuclear Energy Research Advisory Committee and

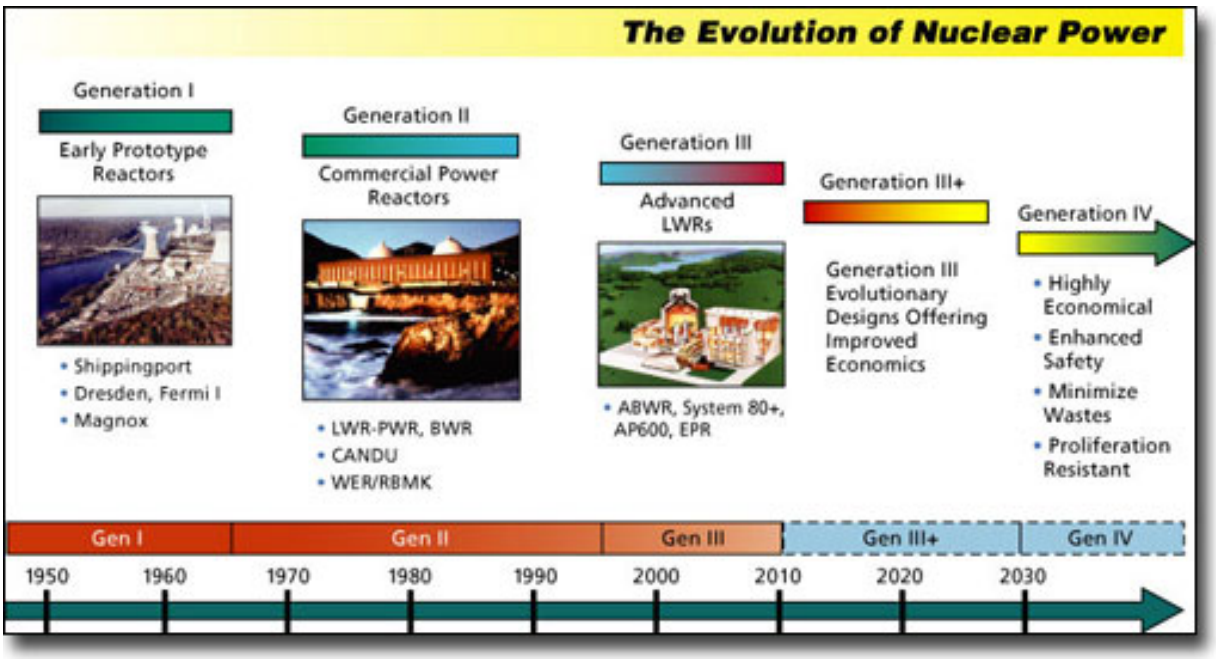

Figure 1.2: History of the nuclear power reactors, reprinted from [NIRS, 2016]

the Generation IV International Forum established a technology roadmap for Generation IV nuclear energy systems. The primary objective of this roadmap is to analyze and select the most promising developments to be future candidates for new reactors, and to represent an international collaboration focusing on reactor research and development. One of the candidates is the High Temperature Gas-cooled Reactor (HTGR). Its core outlet temperature reaches 1,000 °C or higher, allowing it to generate more energy. Using helium gas as a coolant and graphite as a moderator, the HTGR is designed with a greater than 50% efficiency and a thermal power between 600 to 800 MW thermal [Ball et al., 2008].

1.2 Research background

Given that the HTGR is a cutting-edge technology, investigating its safety is key to ensuring the success of this reactor type. The U.S. Department of Energy (DOE) and

the Idaho National Lab (INL) are developing a safety code for the reactor to be used under normal operations and accidental scenarios [Oh et al., 2006]. The U.S. Nuclear Regulatory Commission (U.S. NRC) established a report of next-generation nuclear plant Phenomena Identification and Ranking Tables (PIRTs) with the goal of identifying safety-related phenomena and ranking their importance and the related knowledge behind them for the Modular High Temperature Gas Cooled Reactor (MHTGR). Two primary accidental scenarios ranked using the PIRTs are the depressurized conduction cooldown (DCC) and the pressurized conduction cooldown (PCC) [PIRT, 2008]. In the DCC or the Loss-of-Coolant Accident (LOCA), the primary coolant undergoes a quick depressurization, thus causing a reactor scram. With the pump failing, natural circulation occurs between the reactor vessel and the confinement leading to a rejection of the heat by natural circulation. Meanwhile, the PCC or Loss-Of-Reactor Core Accident (LOFA) occurs when a force loss happens during a reactor scram due to power loss. During a reactor scram, blowers and pumps cease working, but the primary system remains at full pressure. Here, natural convection will move the heat from the core to the reactor cavity cooling system (RCCS). At the upper plenum of the reactor, the mixing of hot plumes that come from the heated coolant channel (a.k.a. the fuel) of the reactor core will occur [Anderson et al., 2008; McCreery and Condie, 2006]. Hot gas flow is discharged from the core region as a free shear flow into the upper plenum (hemisphere), where it moves upward and impinges on the upper plenum. If the flow rate is momentum-driven, stemming from relatively large heat fluxes, a jet will be generated. If the flow rate remains density-gradient driven in the plenum, the gas flows gently upward and merges in the upper regions of the plenum, and thus a plume will be generated. In certain situations, the flow may emerge from the core coolant channels as a jet, and

subsequently evolve to a plume, prior to reaching the nearest structure, as it moves upward. The fundamental mechanism of a jet and a plume is different. Mixing in jet flows is associated with the inertia of turbulent eddies, while buoyancy forces in plume flows produce inertia leading to mixing. A buoyant jet or forced plume is a combination of both momentum and buoyancy.

1.3 Research objectives

For the PCC and DCC scenarios, the flow characteristics of the hot jets or plumes discharging from the reactor core to the HTGR hemispherical vessel structure is a figure of merit from both the operational and safety perspectives. The proper understanding of the thermal-hydraulic characteristics of flow mixing and heat transfers of jets/plumes in the upper plenum is important. High-fidelity experimental data with high spatial and temporal resolutions are essential to assess and validate the performances of simulations using the system codes and computational fluid dynamics (CFD) models currently in use by the nuclear industry. The main objectives of this research are to study the flow and heat transfer characteristics of isothermal and non-isothermal single jets mixing in the upper plenum volume and impinging on the top wall. This was done by conducting high spatial and temporal resolution measurements of velocity and temperature fields related to flow mixing and heat transfer in the upper plenum when the jets/plumes emerge from the core.

1.4 Outlines

Chapter 2 reviews literature on the impingement jet and unique characterizations of different regions in impingement jets. An overview of the two measurements used for this research is also provided, namely time-resolved particle image velocimetry (TR-PIV) and

Planar-Laser Induced Fluorescence (P-LIF).

Chapter 3 provides an overview of the experimental facility and the importance of each part along with the experimental procedures for both the isothermal and non-isothermal cases, with its uncertainty.

Chapter 4 shows the experimental results for both isothermal and non-isothermal cases. The statistical results obtained from TR-PIV measurements are presented and the analysis of two-point velocity cross-correlation and the spectral analysis are discussed. After that, the result obtained from P-LIF measurements are presented.

Finally, Chapter 5 provides a summary of this research along with conclusions and future studies recommendations.

2. LITERATURE REVIEW

2.1 Impinging jet

The impinging jet is a well-established approach used in many different industrial applications to produce high transfer coefficients for heating, cooling, and drying surfaces. It is used to cool down hot turbine blades, reactor cores, and many other items used in manufacturing processes. Researchers have studied both the experimental and numerical analysis of the impinging jet process to understand the complexity of the flow characteristics of the turbulence behavior of the jets (Martin [1977], Lee and Lee [2000], and Nguyen et al. [2019a]).Impinging jets can be driven by either the momentum of the source, an isothermal jet, or the bounce of the source's non-isothermal plume. Impinging jets have received significant attention in literature, including notable research by Corrsin [1943], Gardon and Akfirat [1965], Button and Wilcock [1978], Jambunathan et al. [1992], and Viskanta [1993] among many others.

There are three main regions created by any impinging jet: the free jet region, the stagnation region and the wall jet region. Figure 2.1 illustrates the structure of the impinging jet [Geers, 2004].

2.1.1 Free jet region

As flow exits from the nozzle, the shear-driven force produces an entrainment of mass, momentum and energy. The velocity at the potential core remains constant and equal to the jet exit velocity; hence, this is where the maximum velocity of the jet occurs. Further downstream, the velocity starts to decrease with an increase in the total mass flow rate.

During this process, the jet starts to lose some of its kinetic energy as the velocity profile expands downstream and narrows along both sides of the jet. Thus, a non-uniform velocity profile is present. The length of the potential core depends on several characteristics such as jet nozzle geometry and velocity of the flow.

After the flow passes the potential core zone, it enters the developing zone. In this zone, the axial velocity profile begins to decay and turbulence increases. At the fully developed zone, the velocity profile is fully developed and a transition to the stagnation region started [Shukla and Dewan, 2017] and [Geers, 2004]. Note that throughout the free jet region, there is no effect on the impingement plane.

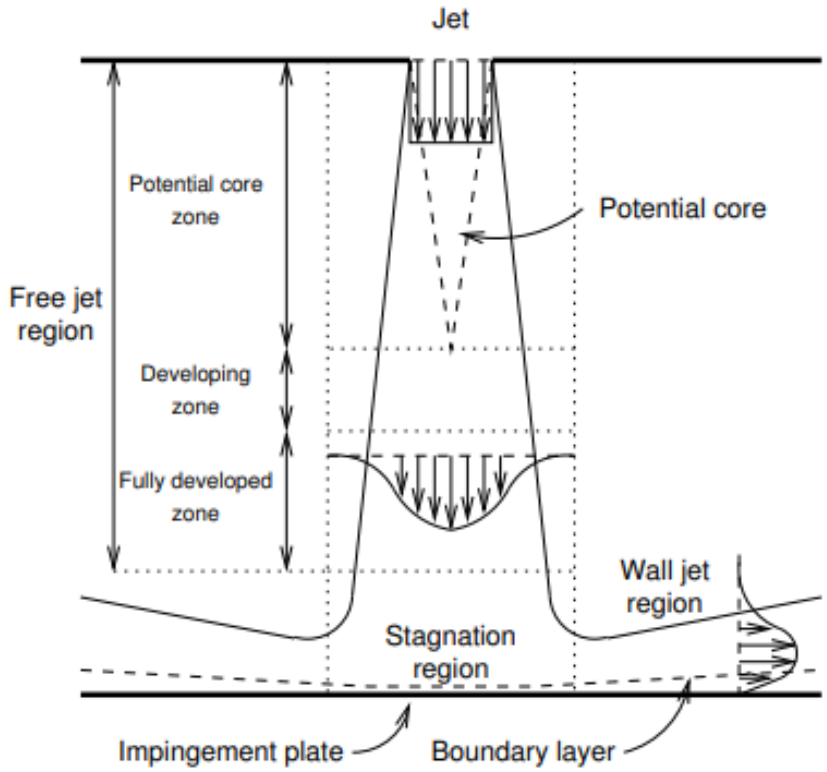

Figure 2.1: Impinging jet structure with three main regions, reprinted from [Geers, 2004]

2.1.2 Stagnation region

At the stagnation region, axial momentum and normal stress are converted into static pressure. The flow velocity significantly decelerates as it approaches the impingement plane and it starts to change from the axial to radial direction. The radical component increases from zero to its maximum value [Nishino et al., 1996] and[Schabel and Martin, 2010].

2.1.3 Wall jet region

Flow at the wall jet region starts to increase with an increased distance along the stagnation region. Then the static pressure and ambient pressure become identical.

One application of jet impingement in the field of nuclear reactors occurs when the jet impinges an upper plenum wall of the nuclear reactor core, such as the High Temperature Gas-cooled Reactor (HTGR). Figure 3.4 shows the impinging jet structure at the upper plenum of a typical reactor.

2.2 Time-resolved particle image velocimetry (TR-PIV)

Particle Image Velocimetry (PIV) is a non-intrusive technique to measure the velocity at a particular area at an instant time [Raffel et al., 2013]. It was first used more than 20 years ago and has developed since. As well as being non-intrusive, PIV is one of the most accurate velocity measurement methods. It can provide both temporal and spatial resolutions. Moreover, and unlike other velocity measurement techniques, PIV gives a velocity profile of the whole field. This is helpful for understanding the flow behavior not only at a particular point but in the system as a whole [Adrian, 2005] and [Jahanmiri, 2011]. There

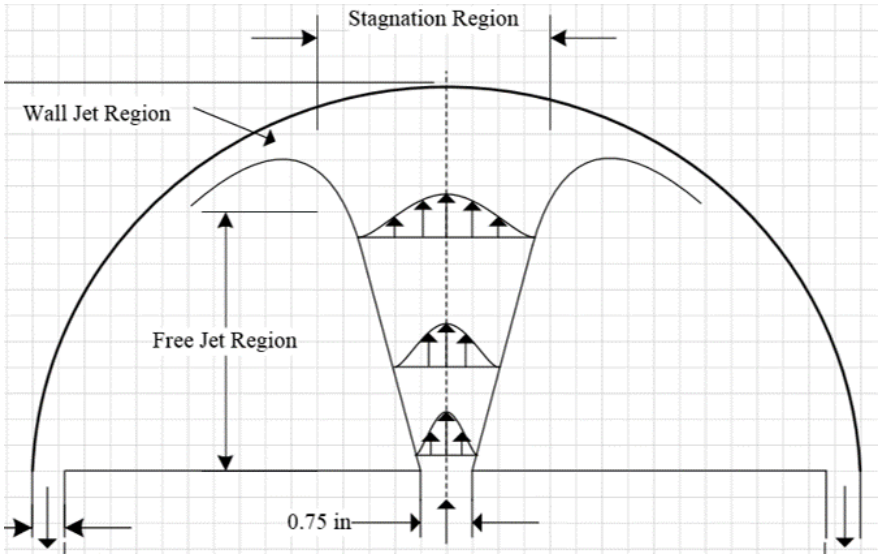

Figure 2.2: Impinging jet structure at the upper plenum of a typical reactor

are several applications and fields in which PIV can be used. For example, it can be used to analyze the behavior of blood in a mechanical circulatory and respiratory support system prior to use for high risk heart disease patients. [Pauls et al., 2018], and Humphreys et al. [1993] used it to study the air interactions on the wing of an airplane.

The main principle of the PIV is calculating the velocity by using this equation:

$$\upsilon = \frac{\Delta x}{\Delta t} \tag{2.1}$$

where υ is the velocity, Δx is the displacement of a particle at location x from t_0 to t_1, aka Δt. This was done using special elements (see Figuer 2.3). The required elements for a typical TR-PIV system are as follows.

- **Particles**: PIV detects the displacement of particles to calculate the velocity. The particles used should behave identically to the fluid. Particles used must be small enough to follow the flow without preventing it, and at the same time must be large

enough to be seen by the camera. The size and type of particles depends upon many factors such as the speed of the flow, the type of flow and the geometry of the system. In addition, particles should be reflecting spherical particles that are homogenously distributed with uniform displacement. The appropriate density of particles will depend on the flow.

- **Light source**: Detecting Particles are detected using a high-frequency laser light source to observe reflecting light from particles. The light source provides a light sheet to focus on particles in an interesting area and eliminate noise from particles in other areas.

- **High speed camera**: The main goal of is to capture the quick movements of small particles with high frequency. This imposes several requirements for the high-speed camera that depend mainly on experimental setup and needs.

- **Calibration**: The pre-processing data of the TR-PIV gives the velocity of a pixel per time step that must be converted to units of distance per unit time, such as meter per second. The frequency of the high-speed camera is used to convert time from frames into seconds. To convert pixels into units of distance, a calibration image with a known object dimension is required. This image can then be used to find the conversion value.

- **Image processing**: Image processing or post-processing is the final step in acquiring velocity data. This can be done using a commercial software or in-house built software. Image processing takes each image and divides it into small interrogation areas, which

are cross-correlated using the equation:

$$C(s) = \int \int I_1(X) \times I_2(X - s) dX \tag{2.2}$$

where I_1 and I_2 are the first and second integration windows. This equation generates a peak and based on this, a velocity vector is produced. By doing this many times, a map of vectors for the whole system is derived that illustrates flow characteristics [Raffel et al., 2013], [Jahanmiri, 2011] and [Alwafi, 2015].

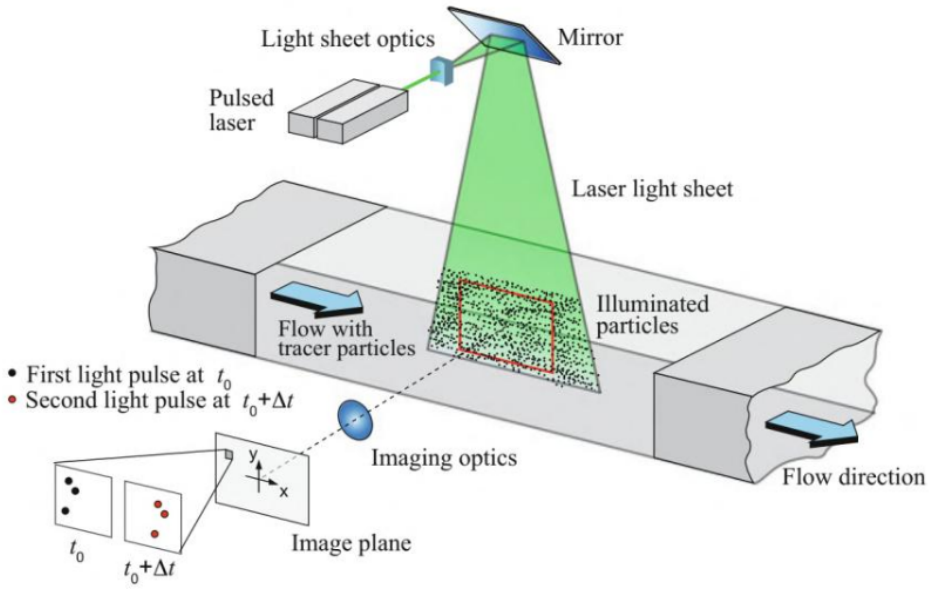

Figure 2.3: Typical PIV arrangement with main parts in an experiment, reprinted from [Raffel et al., 2013]

2.3 Planar laser-induced fluorescence (PLIF)

Tango et al. [1968] were among the first to use exciting of an atom when shot by a laser to visualize flow. Subsequent research eventually led to an ability to measure

temperature as the change of color density in fluorescence when hit by a laser [Coolen et al., 1999], [Ross et al., 2001] and [Thomson and Maynes, 2001].

Laser-induced fluorescence (LIF) is a non-intrusive method that provides a temperature profile for a given area. The main idea behind this technique is that fluorescence particles are excited by a laser source. The excited particles fluoresce at different wavelengths depending on temperature. This occurs by first the absorption of the laser photon and then the emission of a fluorescence photon from the excited state.

Dye is the main component of PLIF measurements; choosing the dye is important and depends on research needs. For example, Rhodamine B is widely used as a temperature-dependent dye to measure the temperature, while Rohamine-110 is used as temperature-independent dye for other flow measurements such as doing simultaneous PIV and LIF measurements [Sakakibara and Adrian, 2004], [Estrada-Pérez et al., 2011], and [Alkhudhiri, 2019]. Other studies use two temperature-dependent dyes to estimate measurement uncertainty [Sutton et al., 2008].

P-LIF can be combined with Tr-PIV system to provide instantaneous. Figuer 2.4 shows the principle of both PIV and LIF system.

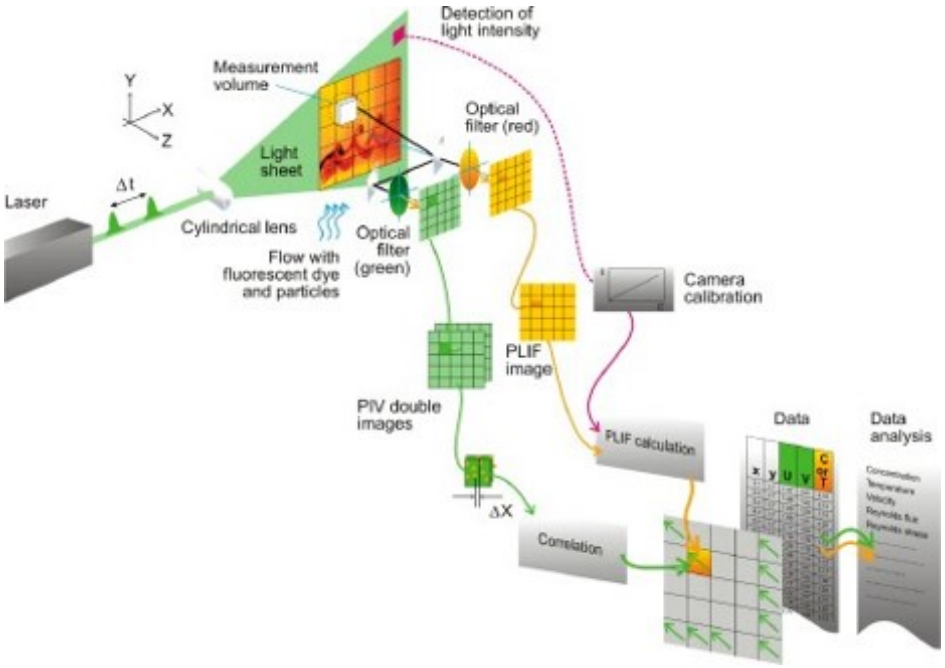

Figure 2.4: Typical instantaneous P-LIF and TR-PIV system and work principle

3. EXPERIMENTAL FACILITY AND SETUP [1]

3.1 Upper plenum experimental facility

This section provides a brief description of the experimental facility. The Thermal-Hydraulic Research Laboratory at Texas A&M University hosts a $1/16^{th}$ scaled version of the reference Generation IV MHTGR reactor. The study by McCreery and Condie [2006] provides the guidelines for the scaling facility and in turn McVay et al. [2015] and Park [2016] provide the preliminary velocity measurements and a detailed facility description of the plume/jet behavior at the upper plenum. The goal of the scaling was to match the scaled properties, the Richardson (Ri) and Reynolds numbers (Re), using water in place of helium as the operating fluid. The Reynolds numbers (Re), as seen in Equation 3.1 is defined as the ratio of inertial forces to viscous forces and the Richardson numbers (Ri) is defined as the ratio of buoyancy to flow shear (Equation 3.2).

$$Re = \frac{VD}{\nu} \tag{3.1}$$

$$Ri = \frac{g\beta\Delta TD}{V^2} \tag{3.2}$$

where V is the mean velocity (m/s), D is the diameter of the pipe (m), ν is the kinematic viscosity ($m2/s$), g is the gravity (m/s^2), β is the thermal expansion coefficient ($1/K$) and ΔT is the difference in temperature (K). Equations 3.3 and 3.4 give the modified

[1] Part of the data reported in this chapter is reprinted with permission from "Time-resolved particle image velocimetry measurements of a single impinging jet in the upper plenum of a scaled facility of high temperature gas-cooled reactors" by Anas Alwafi, Thien Nguyen, Yassin Hassan, and N.K Anand, 2019. International Journal of Heat and Fluid Flow, 76, 113-129, Copyright 2019 by Elsevier.

equations:

$$\frac{Ri_m}{Ri_p} = \frac{\left(\frac{\Delta\rho}{\rho}\right)_m}{\left(\frac{\Delta\rho}{\rho}\right)_p} \frac{V_p^2 D_m}{V_m^2 D_p} \tag{3.3}$$

$$\frac{Re_m}{Re_p} = \left[\frac{(\frac{\Delta\rho}{\rho})_m}{(\frac{\Delta\rho}{\rho})_p}\right]^{0.5} \left[\frac{D_m}{D_p}\right]^{1.5} \frac{\nu_p}{\nu_m} \tag{3.4}$$

where m and p are the model and the prototype upper plenums. Table 3.1 shows the comparison of the main dimensions between the MHTGR and the $1/16^{th}$ prototype test facility, while Figure 3.1 is showing a sketch of the scaled facility [McCreery and Condie, 2006], [McVay et al., 2015], [Park, 2016] and [Alwafi, 2015].

Table 3.1: Dimensions for the Modular High Temperature Gas Cooled Reactor (MHTGR) and the $1/16^{th}$ prototype test facility. See Figure 3.1 for the nomenclature of each dimension. Reprinted from [McCreery and Condie, 2006], and [McVay et al., 2015]

Dimension	MHTGR (m)	$1/16^{th}$ prototype (m)
Bottom of the lower plenum	-2.8826	-
Bottom of the lower reflector L_{RB}	-1.9825	0.05625
Bottom of the core L_{CB}	0	0.18016
Top of the core L_{CT}	7.93	0.6758
Top of the upper reflector L_{RT}	9.516	0.7749
Top of the upper plenum shield L_T	12.6656	0.9718
Height of upper plenum	3.1496	0.197
Reactor vessel inner diameter D_{RV}	6.534	0.4083
Core barrel inner diameter D_{CID}	5.95	0.37
Coolant channel diameter D_C	0.01588	0.01905
Number of coolant channels	11000	25
Coolant channel flow area [m2]	2.177	0.00713
Coolant Channel pitch	0.0322	0.03861
Pitch to diameter ratio	2.03	2.03

Figure 3.2 illustrates the overview of the test facility, including the facility design

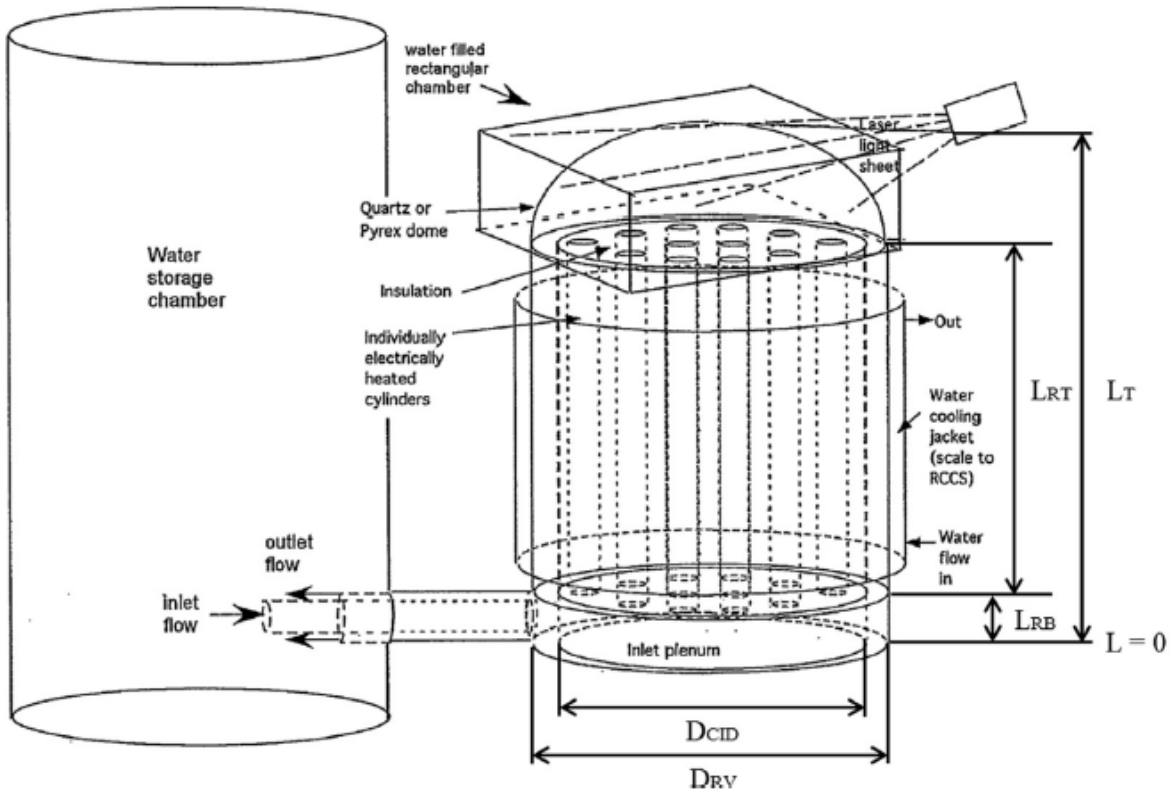

Figure 3.1: A sketch of the scaled upper plenum facility done by McCreery and Condie [2006], McVay et al. [2015], see Table 3.1 for the dimensions. Reprinted from [McVay et al., 2015]

with its main parts, a flow chart, a sketch of the facility including the lower and upper plena, and the core connecting the two plena (the primary components of the facility).

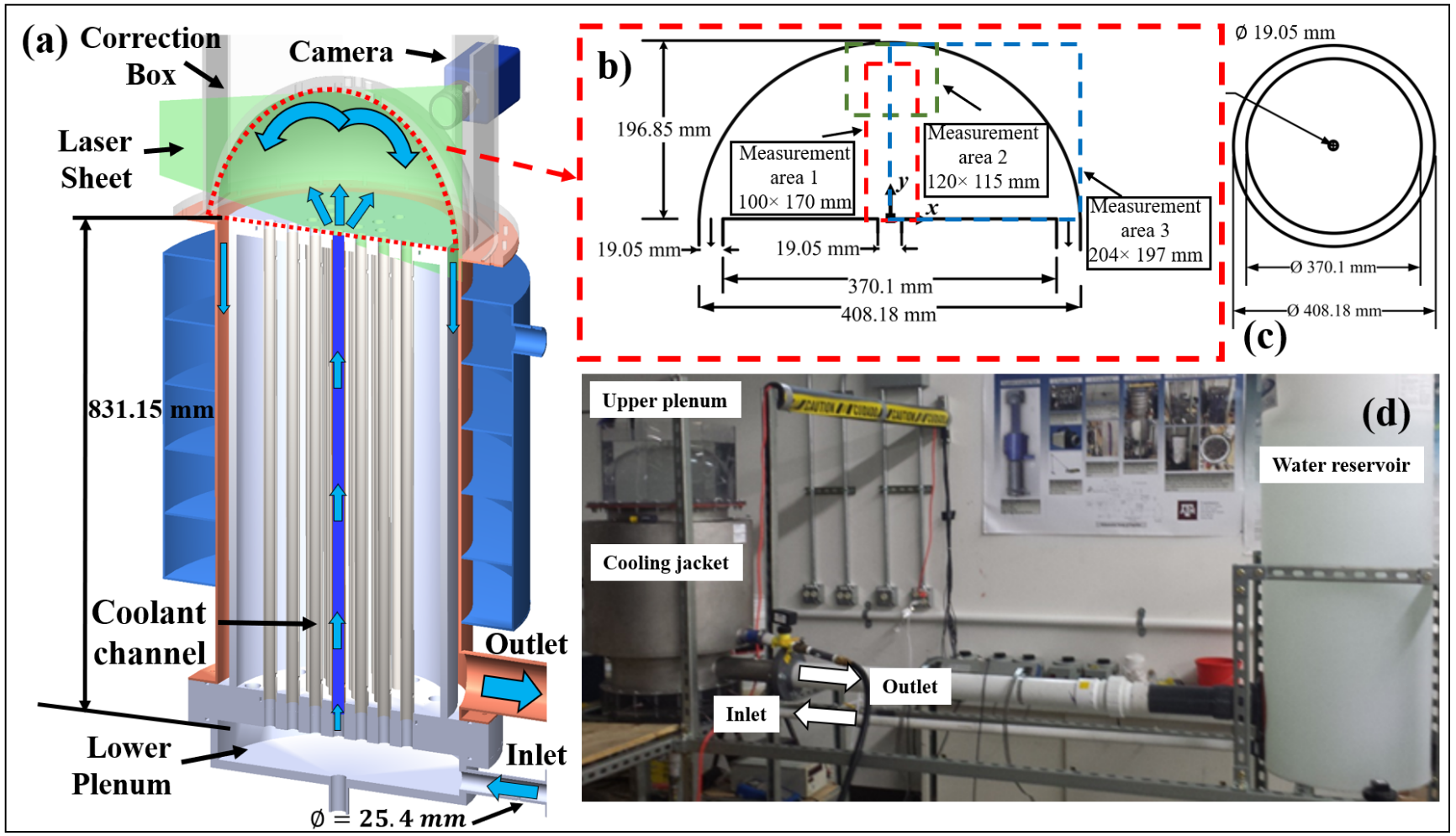

Figure 3.2: An overview of the experimental facility that is $1/16^{th}$ scaled of the MHTGR; a) a cross-section of the core, upper and lower plena, and TR-PIV experiment setup for a single jet and plume; b) the upper plenum dimensions and the TR-PIV test areas (Green and red for the jet and blue for the plume); c) the core layout, with the single opened channel in this study;, and (d) a photo of the experiment facility.

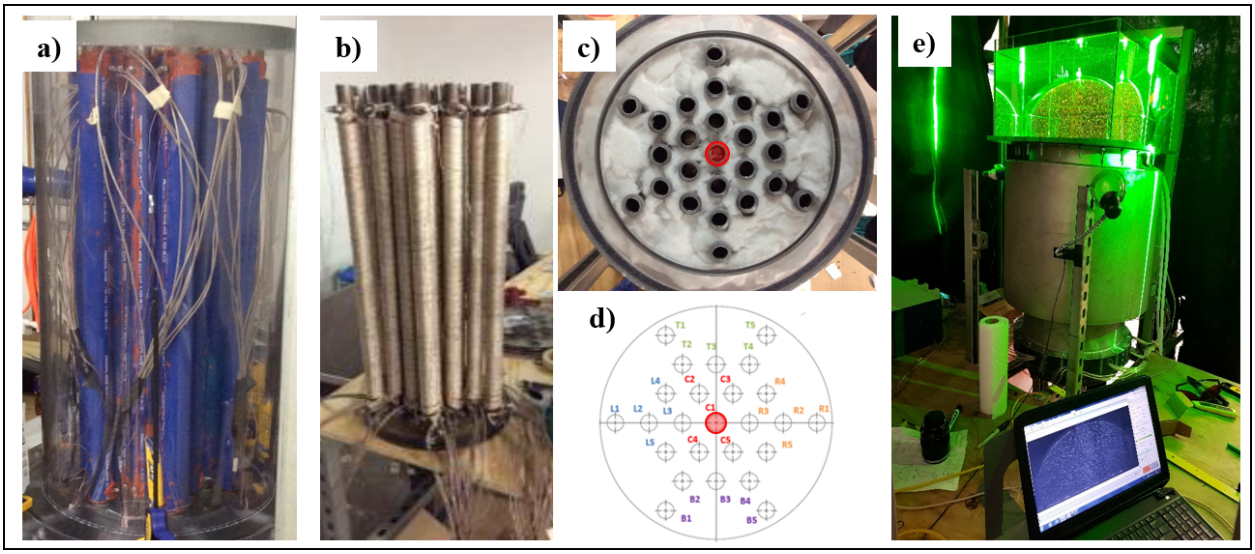

Figure 3.3: A detailed description of the $1/16^{th}$ scaled core; a) the isolated coolant channels inside the core; b) heating tapes around each coolant channel before they were isolated;c) and d) top view of the the core layout, $C1$ (the red dot) is the single opened channel in this study; and d) a photo of the experiment facility during a test

- **The core**

  As the current core design of the HTGR contains 1,020 fuel blocks arranged in a hexagonal shape, the core of the scaled facility contains 25 blocks that are built from 25 pipes (diameter $D_j = 19.05$ mm) to simulate the coolant channels. The coolant channels of the scaled facility were also arranged in a hexagonal shape and into five groups, whose locations were the top (T), bottom (B), right (R), left (L), and center (C), as seen in Figure 3.3, c and d. Each coolant channel was wrapped with heating tape connected to a variable autotransformer to control power going into the system. Figure 3.3 a,b shows the heating tape arrangement.

  The cooling jacket is located around the core. The primary goal of the cooling jacket is to cool down the core by removing the heat and thus maintain a steady state condition.

It is made of stainless steel with a series of baffles that allow cold water to enter and effectively cool the core.

- **The upper plenum**

  The upper plenum is the test area where the flow was discharged from the core coolant channel. It is a hemisphere with a diameter of 408.18 mm and a height of 196.85 mm. The initial design was a polycarbonate cylinder connected to a hemisphere and adjoined parts created as optical distortion for laser illumination. After that, another upper plenum was fabricated as a single body of clear cast acrylic, which provided more optical clearance to the interior volume of the fluid. To mitigate optical distortions caused by the hemisphere curvature, a square correction box, containing the operation fluid, was installed around the hemisphere, as seen in Figure 3.4.

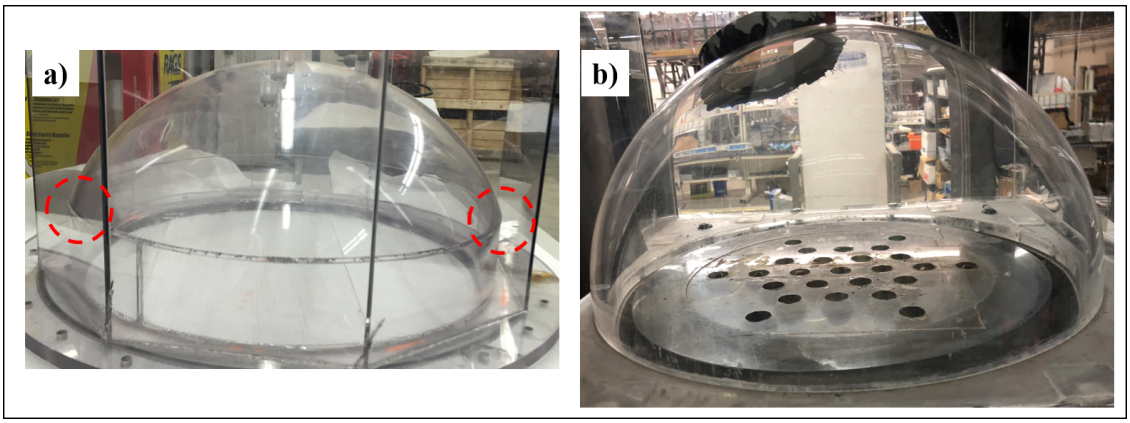

Figure 3.4: The design of the upper plenum; a) the old design where the adjoined parts creating optical distortion for laser illumination; b) the current design, a single piece with smooth curvature allowing full optical access to the plenum

3.1.1 Test procedure

The facility is a closed loop: the water first fills the water tank, then goes to the upper plenum via the coolant channels and circulates back to the water tank. As previously mentioned, two cases, isothermal and non-isothermal, were considered for this research. Each procedure is presented below.

3.1.1.1 Isothermal case

In the isothermal case, the flow characteristics of a single, central jet discharging, and subsequent mixing of fluid at the upper plenum for various Reynolds numbers was experimentally investigated. For this scenario, The Reynolds number Re (Equation 3.1) was calculated using ν = the kinematic viscosity of water at the average inlet temperature (see Table 3.2), and V = the mean bulk flow velocity at the inlet of the upper plenum (aka V_{avg}).

Figure 3.5 shows a flow chart of the test procedure. After filling the facility with DI water at the room temperature, a centrifugal pump is used to create the flow. The pump flow rate is regulated using a variable frequency converter and is measured by a flowmeter. A steady state is achieved when the flow maintains a stable flow rate. When the steady state is achieved, the TR-PIV system (discussed in Section 3.2) is used to record images during a given time.

Table 3.2: Mass flow rate, Reynolds numbers, and the averaged inlet temperature for different experimental sets for the isothermal case.

Set	Mass flow rate [kg/s]	Reynolds number [Re]	Average inlet temperature [° C]
1	0.05	3,413	
2	0.089	5,963	
3	0.118	7,912	19.74
4	0.158	10,622	
5	0.19	12,819	

3.1.1.2 Non-isothermal case

The non-isothermal case uses natural circulation and heat as needed. For this test, the facility was filled with water and the heat turned on slowly using the variable autotransformer until it reached a total power of $0.4kW$. This power level was chosen to satisfy the scaling requirement (see McCreery and Condie [2006] and McVay et al. [2015] for further details) about the scaling. The thermocouples around the system were used to monitor the temperature of the system. When the system was near to a steady state, the cooling jacket was turned on. A steady state was achieved by having the core inlet and outlet differ by $0 \pm 0.5°C$. Once the steady state was achieved, the TR-PIV and PLIF were used to measure the velocity and temperature fields simultaneously (Figure 3.5, b).

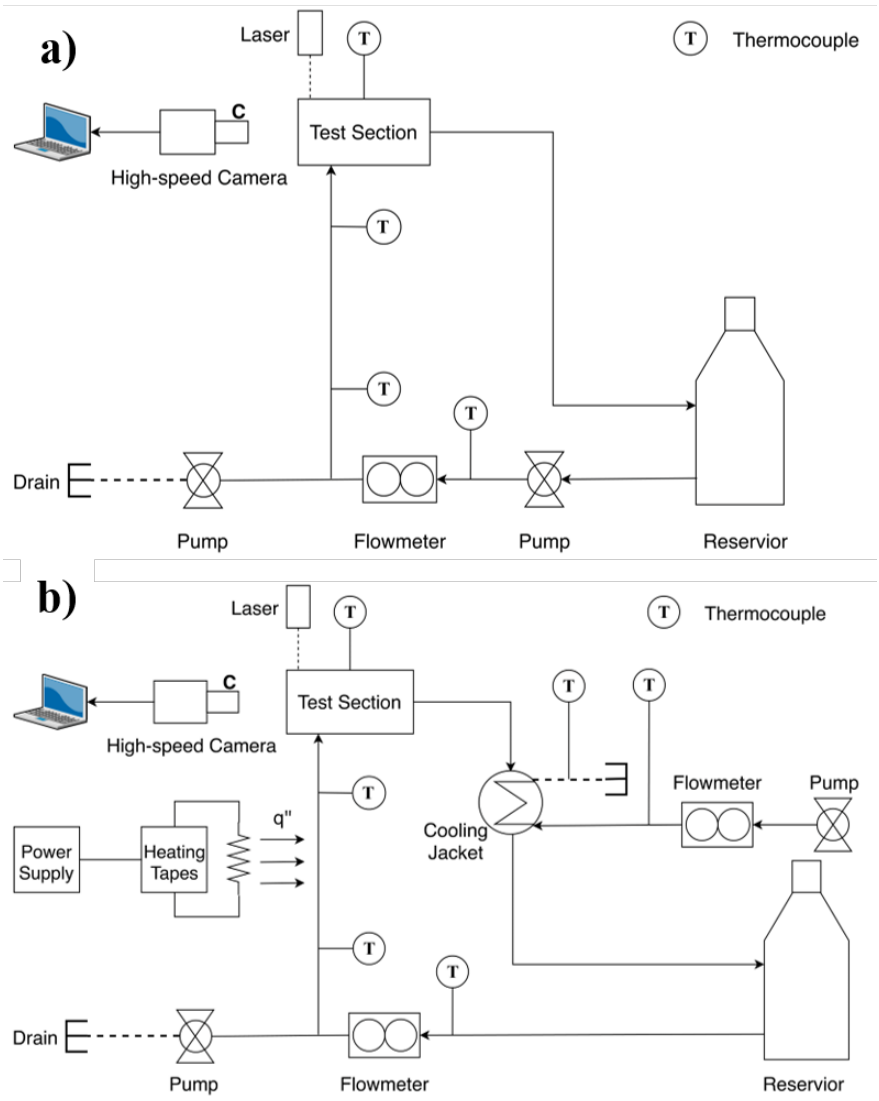

Figure 3.5: Flow chart of the test procedure for a) isothermal case; b) non-isothermal case

3.2 Time-resolved PIV measurements

The PIV system consisted of a 10 W continuous laser with a wavelength of 527 nm, and a Phantom M310 high-speed camera. The laser beam was adjusted using a combination of optics to create a 1.5-mm-thick laser sheet. The camera recorded experimental images of 1,280 $\times$ 800 pixels at various frame rates, ranging from 400 Hz to 700 Hz, corresponding to different Re numbers. The seeding particles were polyethylene microsphere particles with an

average diameter of 13 μm and a density of 1.002 g/cm^3. The seeding particles were mixed with DI water, injected into the system, and circulated within the flow loop prior to the image capture. As shown in Figure 3.2(b), there are four TR-PIV measurement areas. The first measurement area (region 1) is close to the jet inlet, the second (region 2) is close to the upper plenum top wall, the third measurement area (region 3) is a half view of the upper plenum, and the fourth measurement area (region 4) is a full view of the upper plenum. They encompassed as 100×170 mm^2, 120×115 mm^2, 204×197 mm^2, and 408×197 mm^2 (width $\times$ height), i.e., approximately $5.25D_j \times 9D_j$, $6.3D_j \times 6D_j$, $10.7D_j \times 10.3D_j$, and $21.4D_j \times 10.3D_j$ respectively. Regions 1, 2 and 4 represent isothermal cases, whereas region 3 is the non-isothermal case.

The origin of the coordinate system was at the center of the jet outlet, where the x and y coordinates represent the horizontal (transverse) and vertical (axial) directions, respectively, in the PIV measurement plane. In the current research, the flow characteristics of a single jet/plume mixing in the upper plenum were characterized by the TR-PIV measurements.

During the PIV measurements, the camera operated in a single-frame mode and captured a sequence of 8,341 images for each experimental trial. For each studied Reynolds number, two experimental trials were performed yielding 16,682 images which were used to compute the flow statistics. All the PIV images were processed by using an in-house code featuring advanced multipass, multigrid processing based on a robust phase correlation (RPC) [Eckstein and Vlachos, 2009a,b], and previously applied to studies of Nguyen et al. [2017], Goth et al. [2018], Nguyen et al. [2019b] and Nguyen et al. [2019b].

The post-processing analysis starts with transfer of the raw images from the high

speed camera to a workstation computer. A preliminary examination of the images reveals noise, such as the laser reflection from the upper plenum surface (Figure 3.6, a). To improve post-processing of the images, a background subtraction analysis was performed to reduce noise. This was done by finding the background of each experimental trial (8,341 images) and then subtracting that background from all images, as seen in Figure 3.6. The resulting images show only the particles, thus reducing the uncertainty of the PIV estimate.

The PIV integration windows started at 64×64 pixels, and ended at 32×32 pixels; the initial and final passes had a 50% and 75% window overlap, respectively. The velocity vectors were calculated from the correlation map with a Gaussian peak fit for sub-pixel accuracy [Raffel et al., 2013]. Within each pass, statistical validations were calculated to replace any vector errors. Subsequently, the median filter was applied and the standard deviations of the neighboring vectors were used to filter any unexpected vectors [Hassan and Philip, 1997; Westerweel, 1994]. The velocity components corresponding to the x and y directions were U and V, respectively, for the time-averaged velocities; u' and v', respectively, for the fluctuating velocities.

3.2.1 TR-PIV calibration

TR-PIV post processing preliminary results are given in pixel and time step units. To convert this to SI units, such as meters and seconds, a calibration method is required. The main idea of calibration is to find an object inside the system with known measurements and convert the number of pixels to meter units. In this study an aluminum column with a known distance marked was placed inside the upper plenum after tests were performed (Figure 3.7). It was installed at the center of the jet inlet along the same line as the laser

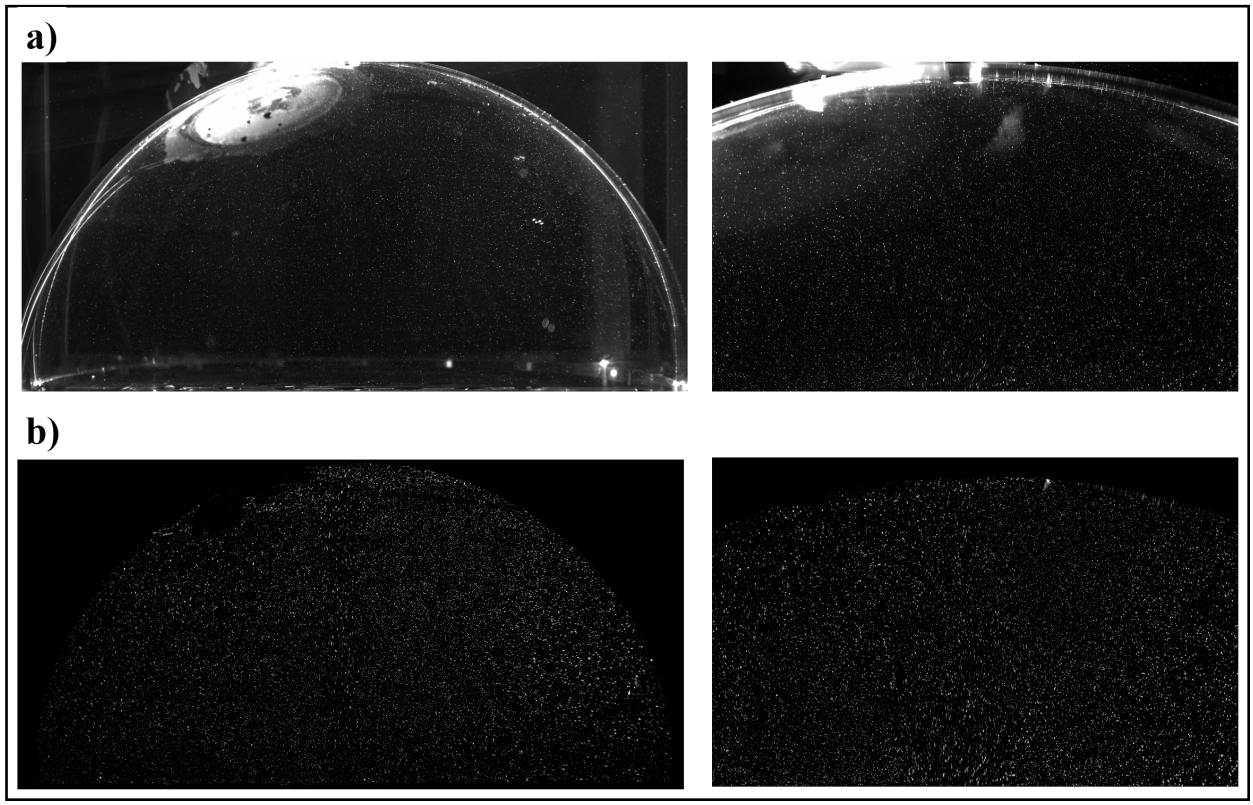

Figure 3.6: Analysis of the background removal a) raw images from the camera, where the laser reflector, noises, can been seen b) images after applying the background subtraction. Left: full view of the upper plenum and Right: Measurement area 2, close to the top upper plenum

sheet. The distance of the known column was calculated in pixels and then converted to meters.

3.2.2 TR-PIV uncertainty

For all the post-processing TR-PIV measurements, spurious vectors were detected during the validation steps and the number of erroneous vectors that failed the validation in the final pass was less than 5% of the total PIV velocity vectors. The performance and uncertainty of the RPC algorithm were extensively accessed in the studies of Timmins et al. [2012], Wilson and Smith [2013], Charonko and Vlachos [2013], and Boomsma et al. [2016].

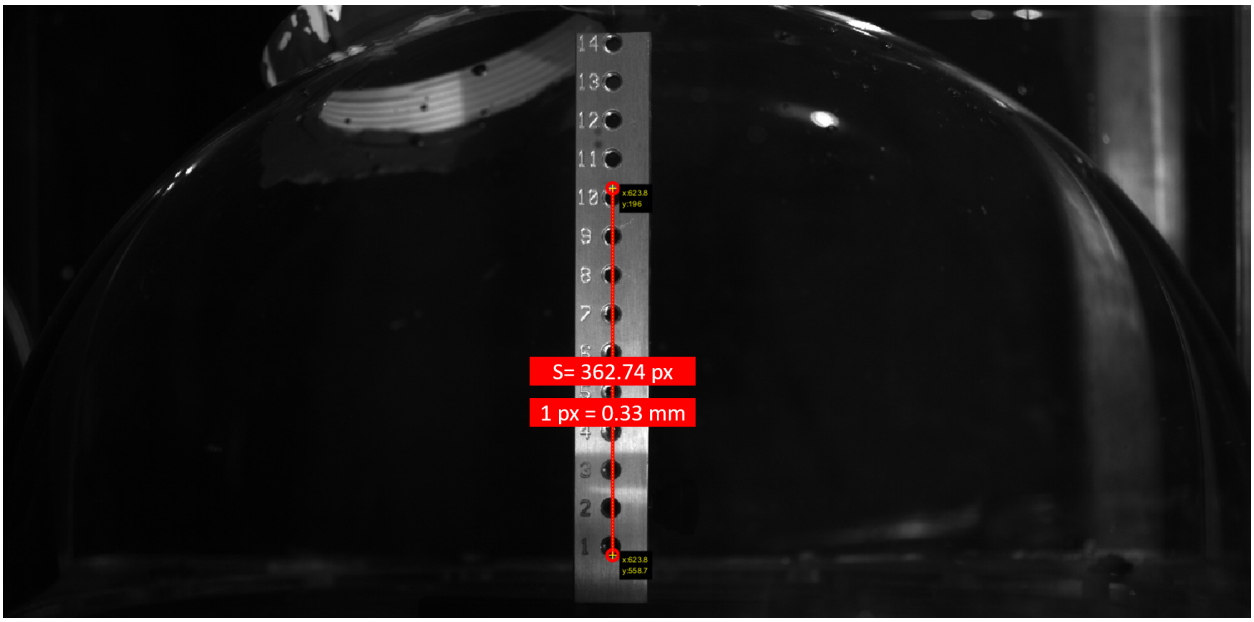

Figure 3.7: Calibration image showing an aluminum column with a known distance and known pixel different to convert the distance from pixel to meter

These authors estimated the overall uncertainty of the RPC code as approximately 0.1 pixels. Using the approaches proposed by Sciacchitano and Wieneke [2016], the uncertainties for the first- and second-order PIV statistical results were estimated, including the mean velocities, root-mean-square fluctuating velocities, and Reynolds stress. Sciacchitano and Wieneke [2016] calculated the uncertainty of the mean velocity $U_{\bar{u}}$ as:

$$U_{\bar{u}} = \frac{\sigma_u}{\sqrt{N}} \tag{3.5}$$

where N is the total number of measured variables, and σ_u is the measurement errors and it is caluclated as:

$$\sigma_u^2 \approx \sigma_{u,fluct}^2 + \bar{U}_u^2 \tag{3.6}$$

where $\sigma^2_{u,fluct}$ is the true velocity fluctuations, and $\bar{U}^2_u$ is the mean-square of U_u.

Also, Sciacchitano and Wieneke [2016] calculated the stander deviation U_{σ_u} and the Reynolds shear stress $U_{R_{uv}}$ uncertainties as:

$$U_{\sigma_u} = \frac{\sigma_u}{\sqrt{2(N-1)}} \tag{3.7}$$

$$U_{R_{uv}} = \sigma_u \sigma_v . \sqrt{\frac{1+\sigma^2_{uv}}{N-1}} \tag{3.8}$$

The estimated uncertainties of the PIV statistics summarized in Table 3.3 are the maximum values normalized by the jet velocity U_c, and those values correspond to various Reynolds numbers, i.e., Re_1 = 3,413, Re_2 = 5,963, Re_3 = 7,912, Re_4 = 10,622, and Re_5 = 12,819 for region 1 isothermal case. The values from Table 3.3 showed that the mean velocities, root-mean-square (r.m.s) fluctuating velocities, and Reynolds stress exhibited uncertainties less than 1% for all studied Reynolds numbers. Sciacchitano et al. [2015] and Neal et al. [2015] reported that the quantification of uncertainties for instantaneous velocities and velocity derivatives is still challenging because these quantities are related to various experimental parameters and image processing techniques, such as image density, time delay, calibration, interrogation window, and cross-correlation algorithms.

3.3 Planar LIF measurements

The LIF system has almost the same equipment as the PIV system, a 10 W continuous laser with a wavelength of 527 nm and the Phantom M310 high-speed camera, but a fluorescent dye was used instead of particles. For this research, PIV and LIF were run

Table 3.3: Estimated uncertainties, e_{Re_1}, e_{Re_2}, e_{Re_3}, e_{Re_4}, and e_{Re_5}, for statistical results obtained from TR-PIV measurements at Reynolds numbers Re_1 = 3,413, Re_2 = 5,963, Re_3 = 7,912, Re_4 = 10,622, and Re_5 = 12,819, respectively. The values shown here are maximal and normalized by the jet velocity U_c.

	U	V	u'_{rms}	v'_{rms}	$u'v'$
e_{Re_1} (%)	0.106	0.221	0.075	0.156	0.020
e_{Re_2} (%)	0.097	0.242	0.068	0.172	0.018
e_{Re_3} (%)	0.106	0.282	0.075	0.199	0.019
e_{Re_4} (%)	0.133	0.371	0.095	0.262	0.026
e_{Re_5} (%)	0.208	0.562	0.147	0.398	0.039

simultaneously, so the laser source and its thickness (1.5 mm) for LIV was the same as for the PIV measures.

When the system was near to steady state, the fluorescent dye Rhodamine B was inserted into the system and allowed to circulate before running the LIF system. At steady state, the camera recorded experimental images of 768×768 pixels at frame rates of $100Hz$. Region 3, as seen in Figure 3.2,b was used for the PLIF measurement area. Figure 3.8 shows an image from one of the LIF tests. The change of intensity indicates change in temperature. The plume is clearly seen as it comes out from the single coolant channel into the upper plenum.

3.3.1 PLIF calibration

To calculate temperature, the relationship between temperature and Rhodamine B intensity is required. This is given by the equation:

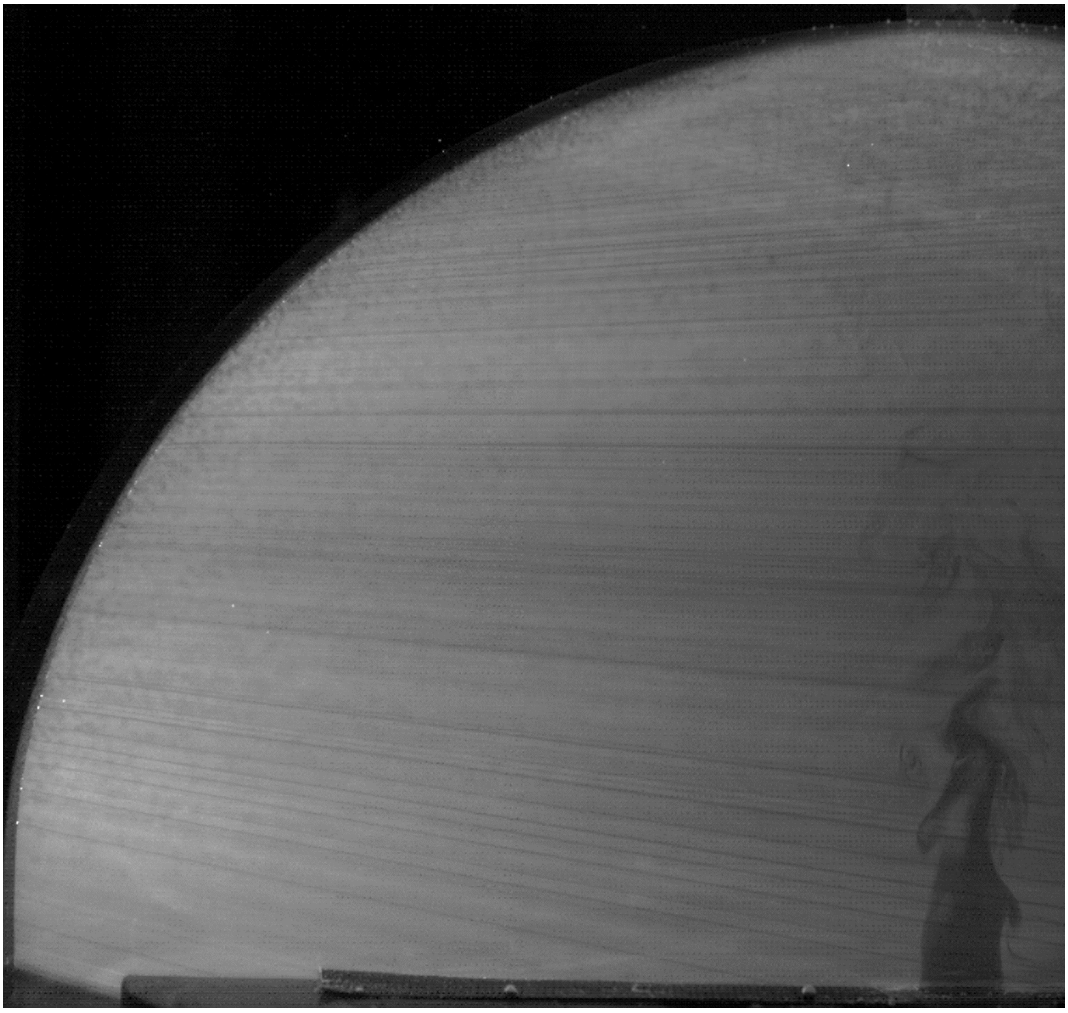

Figure 3.8: An image of one of the PLIF test for measurement area 3

$$I = I_0 W(T) \tag{3.9}$$

where I_0 is the laser intensity and $W(T)$ is a function of temperature [Alkhudhiri, 2019] and [Jones, 2010]. A calibration analysis was done each day of the experiments and prior to the LIF experiment. For this case, the calibrations were performed by injecting Rhodamine B at a concentration of $0.4mg/3.8L$ of water. An electrical stainless-steel heating tube was then inserted into the upper plenum with a pump to circulate water inside the upper plenum.

Images were taken at seven different temperature points (20, 23, 26, 29, 32, 35, and 39°C) using the high-speed camera and the 10 W continuous laser. A thermometer was used to monitor the temperature inside the upper plenum. The range of temperature points was chosen to match working conditions. In-house code was used to calibrate the system using Equation 3.9. The relationship between temperature and laser intensity for LIF experiment is seen in Figure 3.9. Temperature increases as the intensity of the Rhodamine B decreases. It shows a nearly linear relationship, as expected.

An in-house code was used to calibrate the system by using Equation 3.9. Figure 3.9 shows the relationship between the temperature and the laser intensity for LIF experiment. It shows when the temperature increases the intensity of the Rhodamine B decreases. It shows almost a linear relationship and this is what was expected.

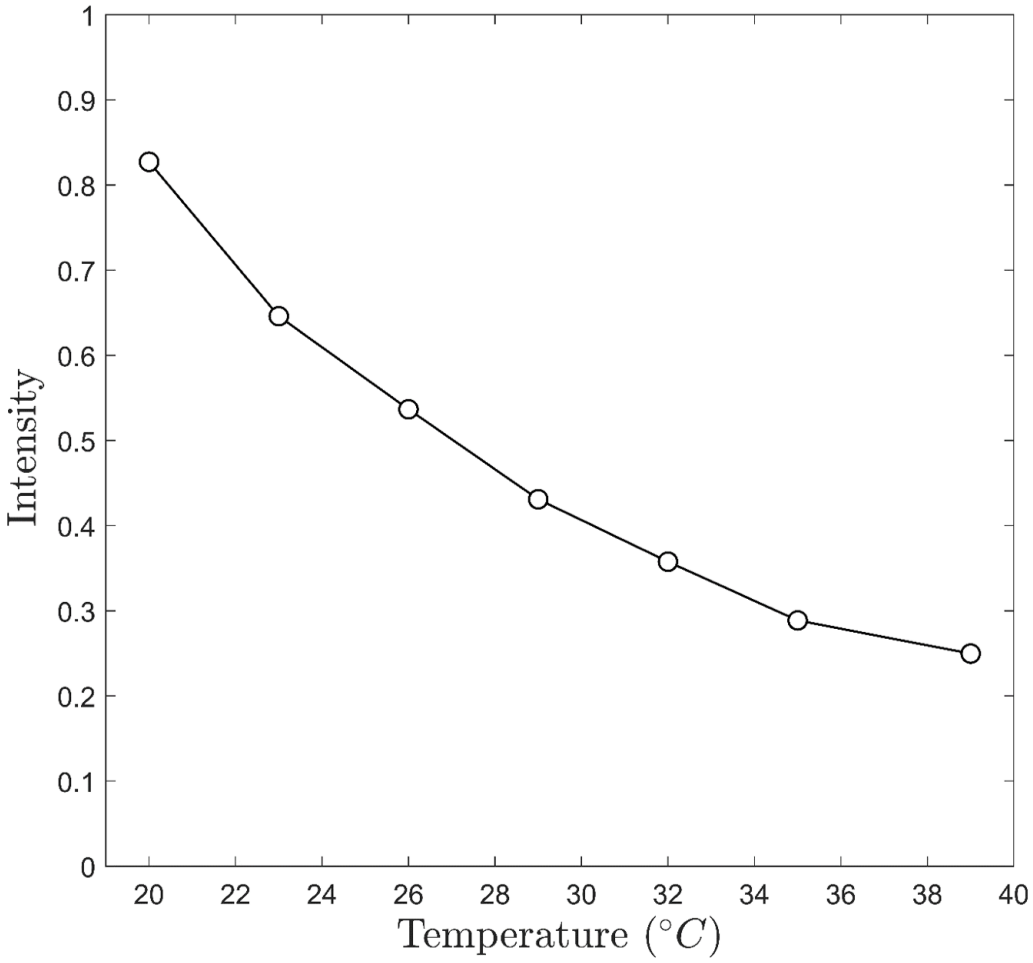

Figure 3.9: LIF Calibration curve showing the relationship between the temperature and the Rhodamine B intensity

4. EXPERIMENTAL RESULTS [1]

4.1 Results from TR-PIV measurements

Preliminary tests were performed for the isothermal case using the TR-PIV system. The whole field of the upper plenum was used as the measurement area, as the goal was to detect the flow when entering, impinging on, and then exiting the upper plenum. Figures 4.1, 4.2 and 4.3 show the color contours of the mean velocity, the transverse velocity, u, the r.m.s. fluctuating axialv'_{rms} and transverse u'_{rms} velocities in m/s, and Reynolds stress $< u'v' >$ in m^2/s^2. Figure 4.3,a shows mean velocity with the streamlines. Two main vortices are visible on each side of the upper plenum; they lack the expected symmetry because the upper plenum is not fully symmetric due to fabrication limitations. Velocity near the jet inlet should be maximal and decrease downstream; however, this is not the case here because the location of the PIV camera is far from the upper plenum and thus it cannot detect the high-speed particles near the inlet. This can also be seen in Figure 4.2 for v'_{rms} where the maximum fluctuation is near the jet inlet. On the other hand, Figures 4.1, b and 4.2, b show u and u'_{rms} better than the transverse velocities. The shifting of the flow direction from horizontal to transverse can be seen near the wall where the flow impinged on the upper plenum wall.

The TR-PIV full view of the upper plenum provides acceptable preliminary results, giving an overview of the flow behavior inside the upper plenum. However, this is not suitable

[1]Part of the data reported in this chapter is reprinted with permission from "Time-resolved particle image velocimetry measurements of a single impinging jet in the upper plenum of a scaled facility of high temperature gas-cooled reactors" by Anas Alwafi, Thien Nguyen, Yassin Hassan, and N.K Anand, 2019. International Journal of Heat and Fluid Flow, 76, 113-129, Copyright 2019 by Elsevier.

for deep analysis nor can it be used for CFD code validation, as it is missing necessary details because of the camera location. For a deeper analysis, farther tests were done with the camera located: near the jet inlet in measurement area 1, and near the upper plenum wall in measurement area 2 (Figure 3.2,a).

4.1.1 Convergence of statistical results computed from TR-PIV velocity fields

For each studied Reynolds number of the isothermal case, N_{max} = 16,682 instantaneous velocity vector fields were obtained from the TR-PIV measurements that could be used to compute the flow statistics. The first- and second-order statistical results computed from the TR-PIV velocity fields, such as the mean velocity, and r.m.s fluctuating velocity for different Reynolds numbers are assessed. Several approaches to assess the convergence of PIV statistical results can be reviewed in Nguyen et al. [2017], dos Santos et al. [2019], and Nguyen et al. [2019b]. In the current assessment, the approach used in Nguyen et al. [2017], Goth et al. [2018], and Nguyen et al. [2018] to define $\epsilon_{N_{1-3}}$ as the absolute differences between the statistical values computed using N_1 = 4,000, N_2 = 8,000, N_3 = 12,000, and those computed using N_{max} velocity snapshots was followed. Figures 4.4 and 4.5 illustrate the comparisons of the normalized mean vertical (axial) velocity component, i.e., V/V_m, and the normalized r.m.s fluctuating vertical velocity component, i.e., v'_{rms}/V_m, where V_m is the local maximum axial velocity. The statistical results corresponded to Re_1 = 3,413, Re_2 = 5,963, Re_3 = 7,912, respectively, and the profiles were interpolated along three horizontal lines, i.e., $L_1(y/D_j = 1)$, $L_2(y/D_j = 3)$ and $L_3(y/D_j = 6)$. In Figures 4.4 and 4.5, the shaded areas illustrate the normalized absolute differences, $\epsilon_{N_{1-3}}/V_m$ for the statistical results of V/V_m and v'_{rms}/V_m, respectively, and for various Reynolds numbers. For

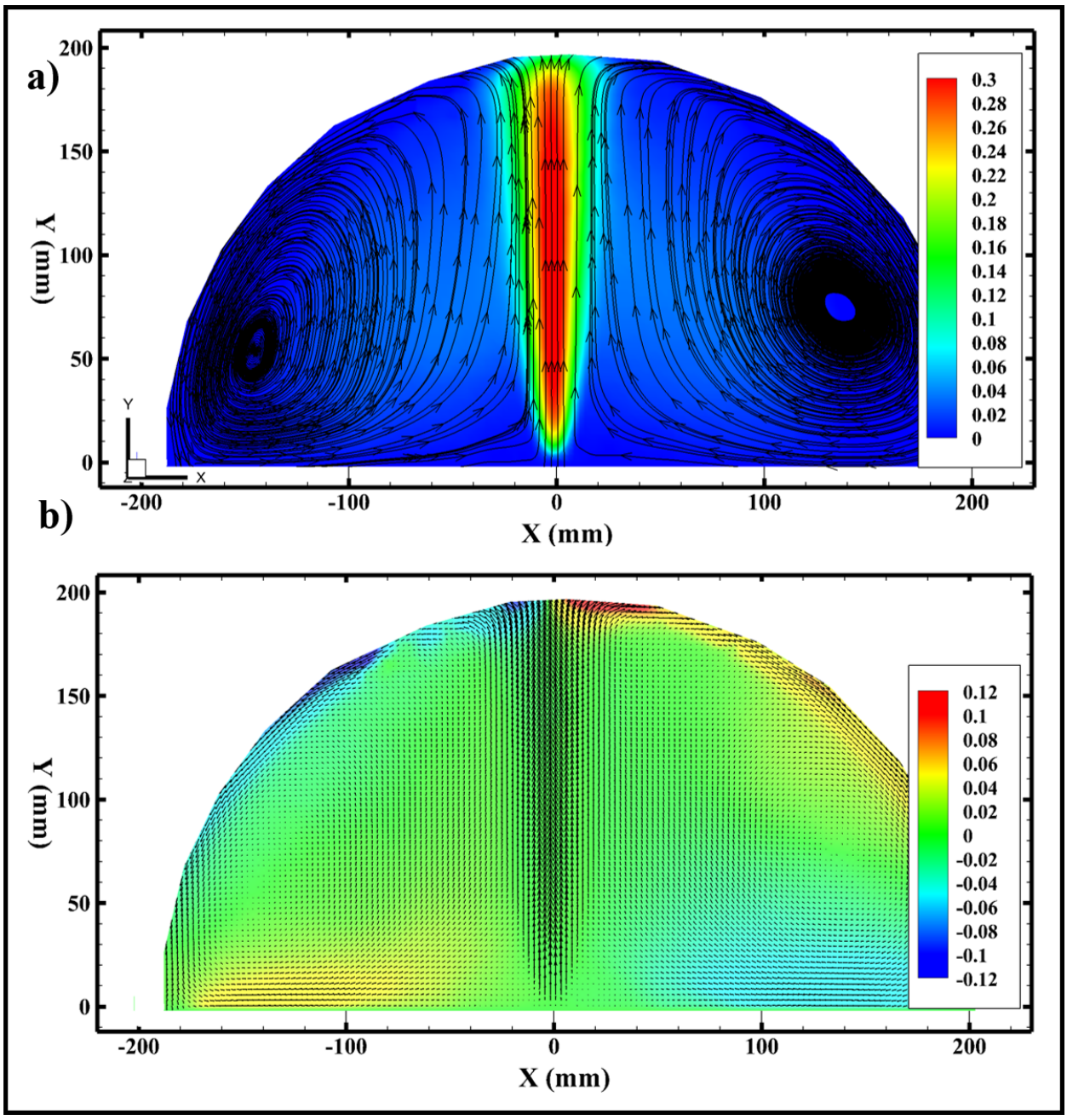

Figure 4.1: TR-PIV results obtained from a single jet mixing in the upper plenum for the full view, measurement area 4. *(a)* Mean velocity vector field and mean velocity magnitude contour (m/s), and color contours of *(b)* transverse velocity u (m/s).

better visualization, the shaded areas were multiplied by arbitrary factors, i.e., $m_1 = 8$ and $m_2 = 5$, as shown in Figures 4.4 and 4.5, respectively. Table 4.1 summarizes the maximum

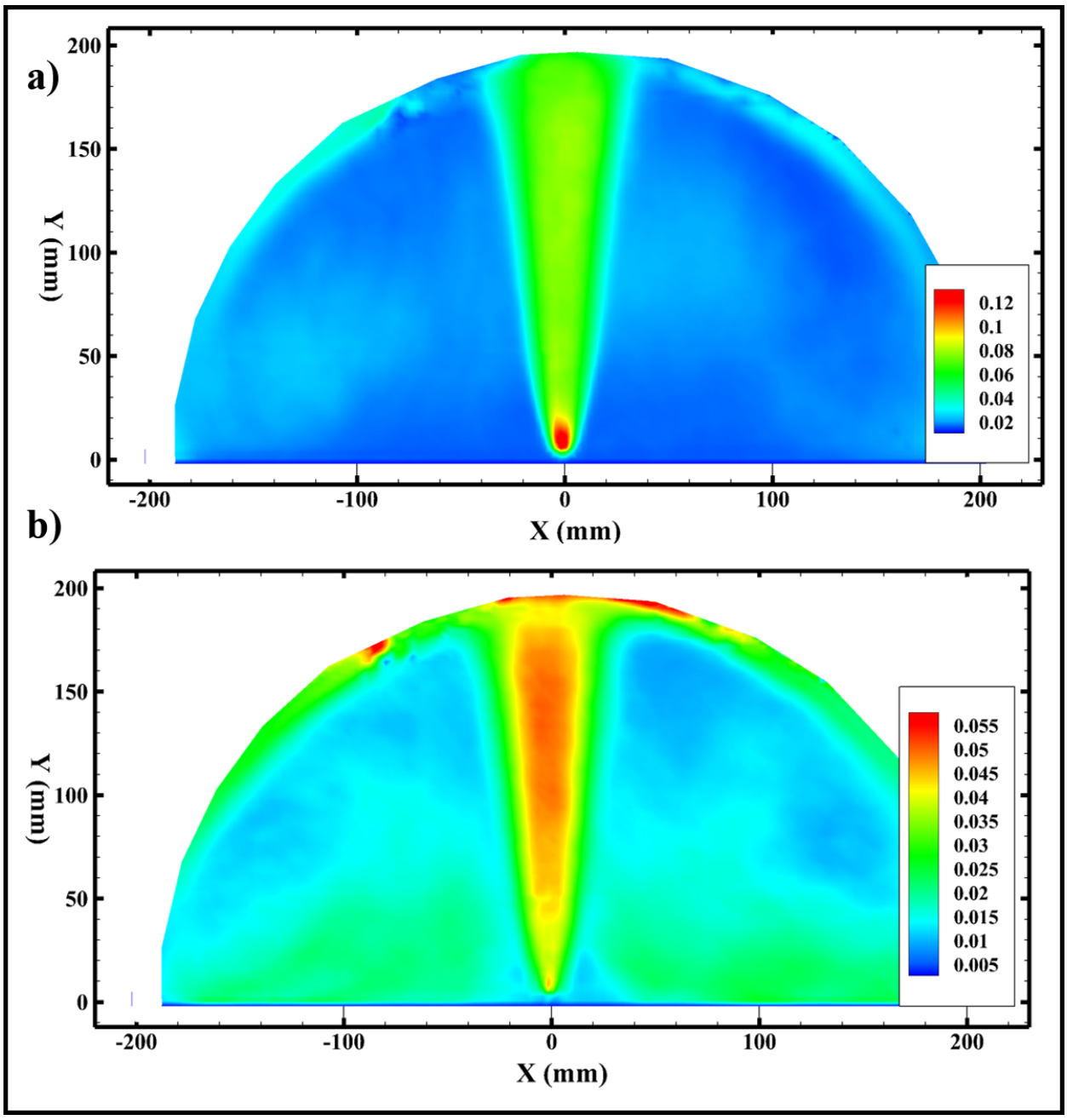

Figure 4.2: TR-PIV results obtained from a single jet mixing in the upper plenum for the full view, measurement area 4. *(a)* r.m.s fluctuating axial velocity v'_{rms} (m/s) and *(b)* r.m.s fluctuating transverse velocity u'_{rms} (m/s).

values of the normalized absolute differences $\epsilon_{N_{1-3}}/V_m$ that were computed for mean velocity components, U and V, the r.m.s fluctuating velocity components, u'_{rms} and v'_{rms}, and for

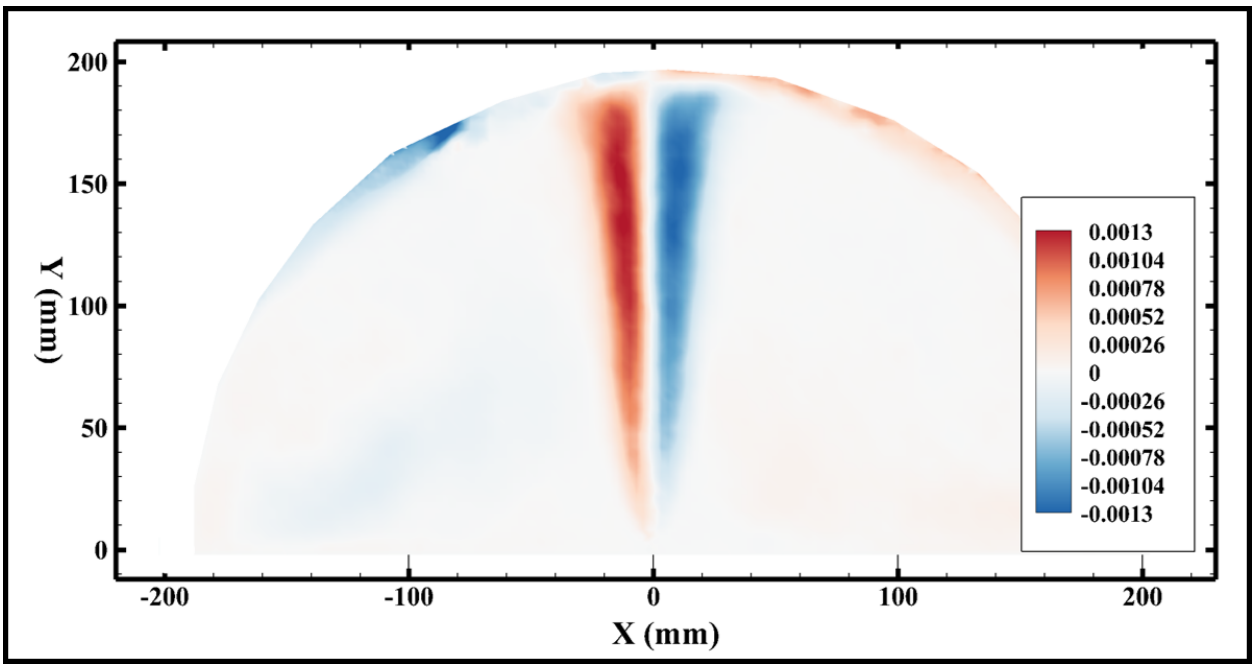

Figure 4.3: TR-PIV results obtained from a single jet mixing in the upper plenum for the full view, measurement area 4, for the Reynolds stress $\langle u'v' \rangle$, (m^2/s^2).

various Reynolds numbers. Figures 4.4 and 4.5, and Table 4.1 show that when the number of velocity snapshots used to calculate the flow statistics increased from N_1 to N_3, the values of $\epsilon_{N_{1-3}}$ noticeably decreased for all the statistical quantities, including the mean and r.m.s velocity components. This confirms the statistical convergences of the results obtained from TR-PIV measurements of a single jet discharging into the upper plenum. All statistical results presented for each studied Reynolds number are calculated using the entire set of N_{max} velocity vector fields.

A second approach was used by Nguyen et al. [2019b] where $\tilde{\varepsilon}_{N_1}, \tilde{\varepsilon}_{N_2}$, and $\tilde{\varepsilon}_{N_3}$ were defined as the spatial average values of the corresponding differences of all the spatial points

in the TR-PIV velocity vector fields by using this equation:

$$\tilde{\varepsilon}_{N_i} = \frac{1}{M}\sum_{j=1}^{M} |(S_j)_{N_i} - (S_j)_{N_{max}}| \tag{4.1}$$

Here, $i = (1, 2, 3)$ is the number of snapshots, M is the total number of the spatial points in the TR-PIV velocity vector fields, and $(S_j)_{N_i}$ is the spatial first- or the second-order statistical results that were computed using the corresponding set of N_{1-3} and N_{max}. Figure 4.6 shows the convergence of the values of $\tilde{\varepsilon}_{N_1}/V_m$, $\tilde{\varepsilon}_{N_2}/V_m$, and $\tilde{\varepsilon}_{N_1}/V_3$ normalized by V_m for Regions 1 and 2 for the TR-PIV statistical results, V, U, v'_{rms}, u'_{rms}, and $u'v'$. Tables 4.2 and 4.3 the values of $\tilde{\varepsilon}_V/V_m\%$, $\tilde{\varepsilon}_U/V_m\%$, $\tilde{\varepsilon}_{v'_{rms}}/V_m\%$, $\tilde{\varepsilon}_{u'_{rms}}/V_m\%$, and $\tilde{\varepsilon}_{u'v'}/V_m\%$ for the mean velocities and the RMS fluctuation velocities obtained from the TR-PIV measurements along Regions 1 and 2 for the Reynolds numbers Re_1 to Re_5 across the different velocity snapshots N_1, N_2, and N_3. As shown in Figure 4.6 and Tables 4.2 and 4.3, the values $\tilde{\varepsilon}_{N_1}$, $\tilde{\varepsilon}_{N_2}$, and $\tilde{\varepsilon}_{N_3}$ decrease substantially as the number of velocity snapshots applied to calculate the statistical result increase from N_1 to N_3. The maximum error values are at the axial velocity V, as this is the main direction of the flow. At region 1 for Re_5 of $V/V_m\%$ the value is 1.25% for N_1, the maximum error, while the minimum error was found to be less than 0.01% for both Regions 1 and 2 for $u'v'$.

The previous analysis was done for the TR-PIV convergence for the isothermal case, and I now apply the same analysis to the non-isothermal case. A total of $N_{max} =$ 50,000 instantaneous velocity vector fields were obtained from the TR-PIV measurements for computing flow statistics. Using the second technique presented above, the statistical results from the first- and second order velocities were used to study the convergence of

results by comparing them with different numbers of velocity snapshots: N_1 = the first 10,000,, N_2 = the first 15,000 and N_3 = the first 30,000, and N_{max} = the total number of velocity snapshots. Figure 4.7 and Table 4.4 show convergence of the statistical results. The values of $\epsilon_{N_{1-3}}$ decrease as the number of velocity fields increase. The maximum convergence was at $\tilde{\varepsilon}_v/V_m$ for N_1 at 0.55 and the minimum was $\tilde{\varepsilon}_{u'v'}/V_m\%$ at 0.03. Moreover, the values of $\tilde{\varepsilon}_{N_3}/V_m$ detected were approximately half that of the $\tilde{\varepsilon}_{N_1}/V_m$ values for all velocities, i.e. v, u, v'_{rms}, u'_{rms}, and $u'v'$.

In sum, for the isothermal and non-isothermal cases, the statistical results obtained from the TR-PIV converged.

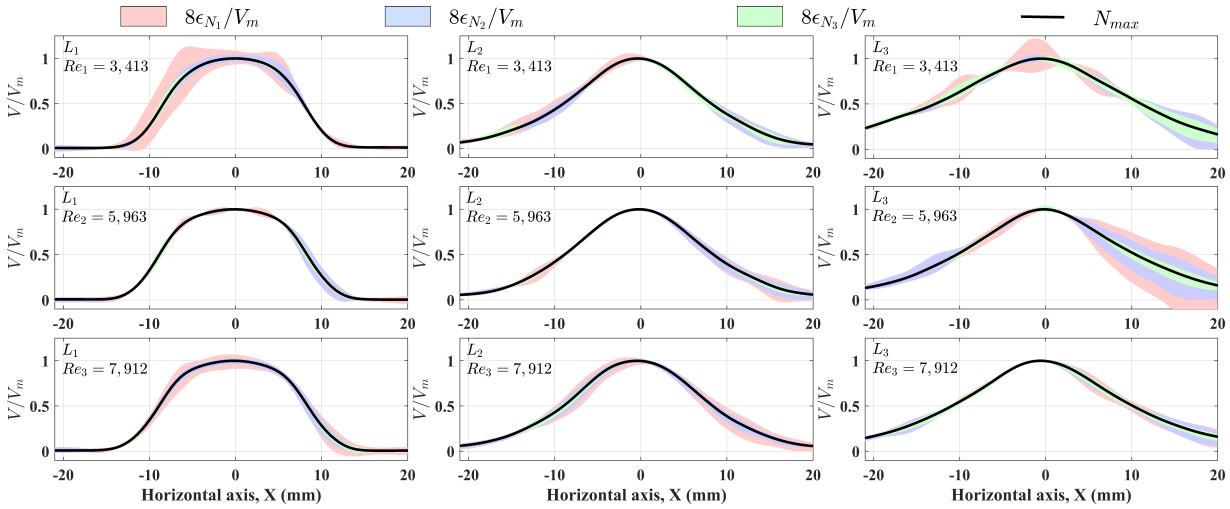

Figure 4.4: Convergence of TR-PIV statistical results for Re_1 = 3,413, Re_2 = 5,963, and Re_3 = 7,912. Profiles of normalized mean vertical velocity, V/V_m, were computed along the lines $L_1(y/D_j = 1)$, $L_2(y/D_j = 3)$ and $L_3(y/D_j = 6)$. Shaded colors show the normalized absolute differences $\epsilon_{N_{1-3}}/V_m$ between the statistics computed using N_{1-3} velocity vector fields and those using the entire N_{max} snapshots. Note that the shaded areas were amplified by $m_1 = 8$ to aid visualization.Values are summarized in Table 4.1

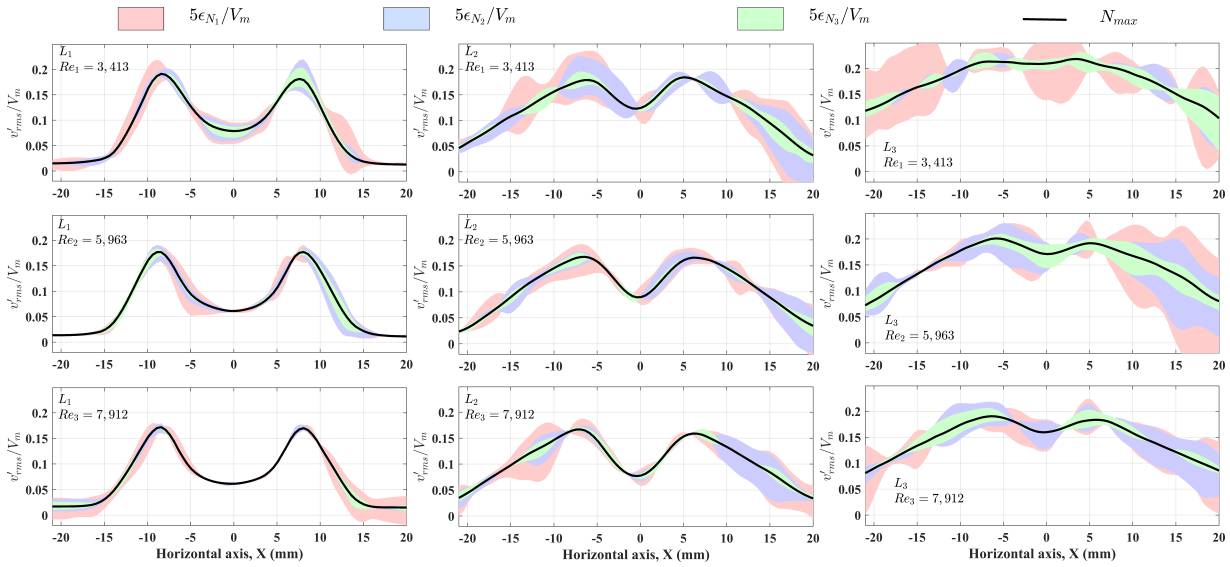

Figure 4.5: Convergence of TR-PIV statistical results for Re_1 = 3,413, Re_2 = 5,963, and Re_3 = 7,912. Profiles of normalized r.m.s fluctuating vertical velocity, v'_{rms}/V_m, were computed along the lines $L_1(y/D_j = 1)$, $L_2(y/D_j = 3)$ and $L_3(y/D_j = 6)$. Shaded colors show the normalized absolute differences $\epsilon_{N_{1-3}}/V_m$ between the statistics computed using N_{1-3} velocity vector fields and those using the entire N_{max} snapshots. Note that the shaded areas were amplified by $m_2 = 5$ to aid visualization.Values are summarized in Table 4.1

4.1.2 Statistical results from the TR-PIV measurements

Having confirmed that the statistical results converged, the statistical results obtained from the TR-PIV measurements for a single jet and plume in isothermal and non-isothermal cases at the upper plenum were analyzed. The statistical results of a single jet mixing in the upper plenum for different Reynolds numbers are presented first and compared to those from other studies using a similar experimental configuration. Next, the statistical results of a single plume mixing in the upper plenum are presented.

First, Figure 4.8 illustrates the mean velocity vector fields, velocity streamlines, velocity magnitude contour, and color contours of the r.m.s fluctuating axial velocity, v'_{rms}, while Figure 4.9 depicts the color contours of the r.m.s fluctuating transverse velocity, u'_{rms},

Table 4.1: Normalized convergences of statistical results computed from TR-PIV velocity measurements for Re_1 = 3,413, Re_2 = 5,963, Re_3 = 7,912, Re_4 = 10,622, and Re_5 = 12,819 along two lines $L_1(y/D_j = 1)$ and $L_2(y/D_j = 3)$. Maximum normalized absolute differences between the mean velocity and r.m.s fluctuating velocity were calculated using N_1 = 4,000, N_2 = 8,000, N_3 = 12,000, and those using N_{max} velocity snapshots.

Set 1, Re_1 = 3,413								
	ϵ_V/V_m (%)		ϵ_U/V_m (%))		ϵ_{urms}/V_m (%)		ϵ_{vrms}/V_m (%)	
Line	L_1	L_2	L_1	L_2	L_1	L_2	L_1	L_2
N_1	1.58	2.53	0.81	1.49	0.91	0.97	0.62	0.86
N_2	1.55	1.62	0.73	0.83	0.93	0.95	0.39	0.59
N_3	0.82	0.69	0.33	0.44	0.55	0.33	0.20	0.22
Set 2, Re_2 = 5,963								
N_1	3.94	1.87	0.82	0.80	1.15	1.70	0.63	1.37
N_2	1.41	1.90	0.74	0.78	0.77	1.28	0.22	0.82
N_3	0.84	1.08	0.43	0.63	0.46	0.53	0.17	0.24
Set 3, Re_3 = 7,912								
N_1	1.77	2.88	1.03	1.01	0.72	1.17	0.66	0.91
N_2	1.29	1.72	0.49	0.46	0.33	0.90	0.40	0.48
N_3	0.52	0.90	0.47	0.32	0.33	0.29	0.28	0.24
Set 4, Re_4 = 10,622								
N_1	2.14	8.23	1.00	2.66	0.97	2.91	0.76	1.11
N_2	1.37	3.80	0.73	1.23	0.43	1.04	0.51	0.67
N_3	0.57	0.76	0.68	0.41	0.37	0.61	0.34	0.21
Set 5, Re_5 = 12,819								
N_1	2.90	6.30	1.16	1.64	0.84	3.41	0.93	1.12
N_2	1.52	3.90	0.63	1.02	0.36	1.62	0.66	0.48
N_3	0.44	1.40	0.33	0.67	0.27	1.41	0.23	0.53

and Reynolds stress, $\langle u'v' \rangle$, computed from TR-PIV measurements for Re_1 = 3,413, Re_3 = 7,912, and Re_5 = 12,819 for near the jet exit, i.e., region 1, and the plenum top wall, i.e.,

Table 4.2: The convergence of the statistical results obtained from the TR-PIV for the isothermal case, regions 1 near the jet inlet, of V, U, v'_{rms}, u'_{rms}, and $u'v'$ normalized by V_m for Re_1 to Re_5. For each Reynolds number, the convergence consisting of the three $\tilde{\varepsilon}_{N_1}/V_m$, $\tilde{\varepsilon}_{N_2}/V_m$, and $\tilde{\varepsilon}_{N_1}/V_3$ were N_1 = 4,000, N_2 = 8,000, and N_3 = 16,000 velocity snapshots.

	$\tilde{\varepsilon}_v/V_m$%			$\tilde{\varepsilon}_u/V_m$%			$\tilde{\varepsilon}_{v'_{rms}}/V_m$%			$\tilde{\varepsilon}_{u'_{rms}}/V_m$%			$\tilde{\varepsilon}_{u'v'}/{V_m}^2$%		
	N_1	N_2	N_3	N_1	N_2	N_3	N_1	N_2	N_3	N_1	N_2	N_3	N_1	N_2	N_3
Re_1	0.66	0.44	0.30	0.38	0.28	0.16	0.39	0.22	0.14	0.30	0.16	0.10	0.02	0.02	0.01
Re_2	0.88	0.53	0.22	0.41	0.27	0.13	0.39	0.27	0.10	0.27	0.16	0.07	0.02	0.01	0.01
Re_3	0.53	0.38	0.20	0.31	0.19	0.12	0.37	0.19	0.10	0.26	0.15	0.08	0.02	0.01	0.01
Re_4	1.40	0.85	0.26	0.50	0.30	0.15	0.55	0.24	0.14	0.31	0.18	0.08	0.03	0.01	0.01
Re_5	1.25	0.93	0.48	0.52	0.39	0.21	0.52	0.40	0.26	0.27	0.20	0.13	0.03	0.02	0.01

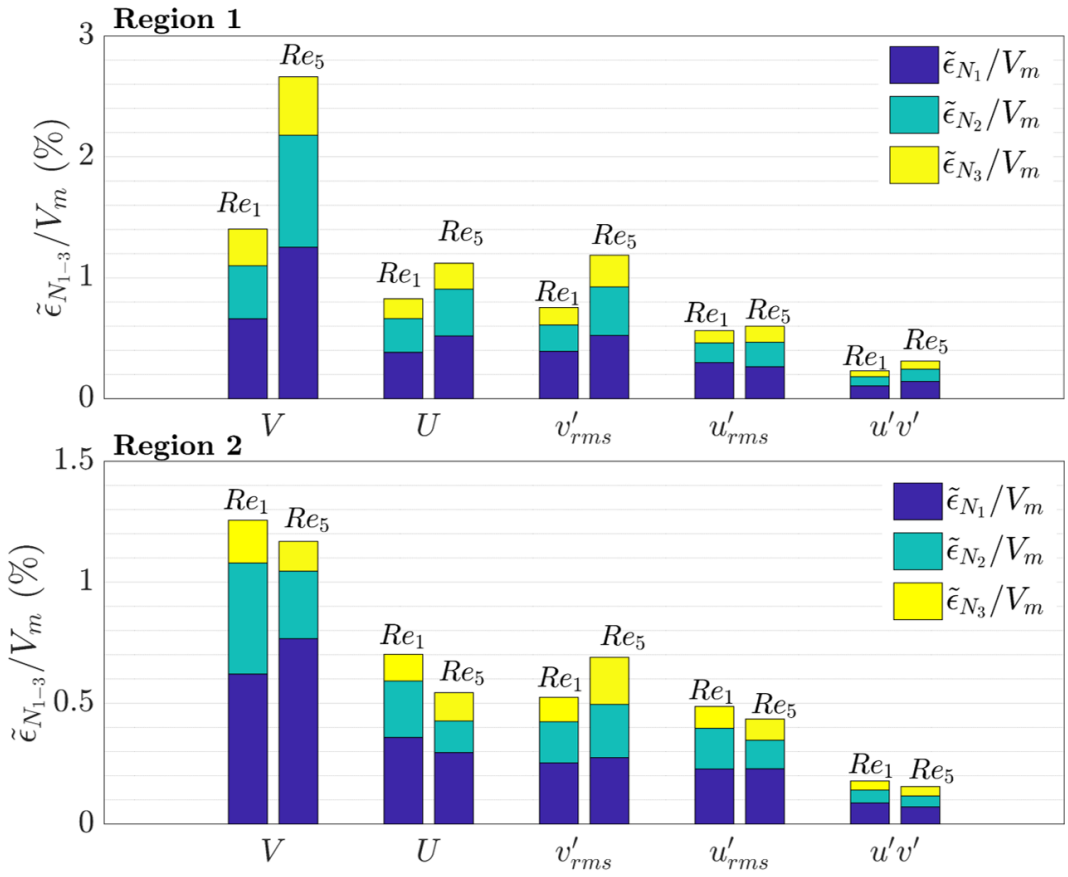

Figure 4.6: The convergence of the statistical results obtained from the TR-PIV of the isothermal case for regions 1 and 2 of V, U, v'_{rms}, u'_{rms}, and $u'v'$ normalized by V_m for Re_1 and Re_5. For each Reynolds number, the stacking bar consisting of the three $\tilde{\varepsilon}_{N_1}/V_m$, $\tilde{\varepsilon}_{N_2}/V_m$, and $\tilde{\varepsilon}_{N_1}/V_3$ were $N_1 = 4{,}000$, $N_2 = 8{,}000$, and $N_3 = 16{,}000$ velocity snapshots. For visualization purposes, the $u'v'$ were multiplied by 5. The values are summarized in Tables 4.2 and 4.3

region 2. As shown, for all studied Reynolds numbers, the jet velocity reached the maximum values, i.e., $V_{c1} = 0.24$, $V_{c3} = 0.54$, and $V_{c5} = 0.88$ m/s for Re_1, Re_3, and Re_5, respectively, at the nozzle exit ($y = 0$), and subsequently gradually decreased farther downstream when the jet started to expand in the transverse direction. Additionally, at higher Reynolds numbers, the jet flow exhibited greater momentum, yielding greater jet penetration depths compared to the jet flow at lower Reynolds numbers. As shown in the color contours of the r.m.s fluctuating velocities and Reynolds stress, shear layers are created owing to a sudden expansion in the

transverse direction. Highly turbulent regions were observed in the jet shear layers that possessed maximum turbulence levels ranging from 14% to 23% of the jet velocity V_c for Re_1 to Re_5 (c.f. Figure 4.8). It is interesting to note that peaks of v'_{rms} were found along the shear

Table 4.3: The convergence of the statistical results obtained from the TR-PIV for the isothermal case, regions 2 near the upper plenum wall, of V, U, v'_{rms}, u'_{rms}, and $u'v'$ normalized by V_m for Re_1 to Re_5. For each Reynolds number, the convergence consisting of the three $\tilde{\varepsilon}_{N_1}/V_m$, $\tilde{\varepsilon}_{N_2}/V_m$, and $\tilde{\varepsilon}_{N_1}/V_3$ were $N_1 = 4{,}000$, $N_2 = 8{,}000$, and $N_3 = 16{,}000$ velocity snapshots.

	$\tilde{\varepsilon}_v/V_m\%$			$\tilde{\varepsilon}_u/V_m\%$			$\tilde{\varepsilon}_{v'_{rms}}/V_m\%$			$\tilde{\varepsilon}_{u'_{rms}}/V_m\%$			$\tilde{\varepsilon}_{u'v'}/{V_m}^2\%$		
	N_1	N_2	N_3	N_1	N_2	N_3	N_1	N_2	N_3	N_1	N_2	N_3	N_1	N_2	N_3
Re_1	0.62	0.46	0.18	0.36	0.23	0.11	0.25	0.17	0.10	0.23	0.17	0.09	0.02	0.01	0.01
Re_2	1.04	0.49	0.28	0.47	0.24	0.15	0.43	0.27	0.10	0.26	0.16	0.09	0.02	0.01	0.01
Re_3	0.77	0.44	0.36	0.40	0.22	0.15	0.29	0.20	0.12	0.27	0.15	0.10	0.02	0.01	0.01
Re_4	0.80	0.62	0.33	0.51	0.29	0.15	0.37	0.31	0.23	0.28	0.18	0.13	0.02	0.01	0.01
Re_5	0.77	0.28	0.29	0.30	0.13	0.12	0.27	0.22	0.20	0.23	0.12	0.09	0.01	0.01	0.01

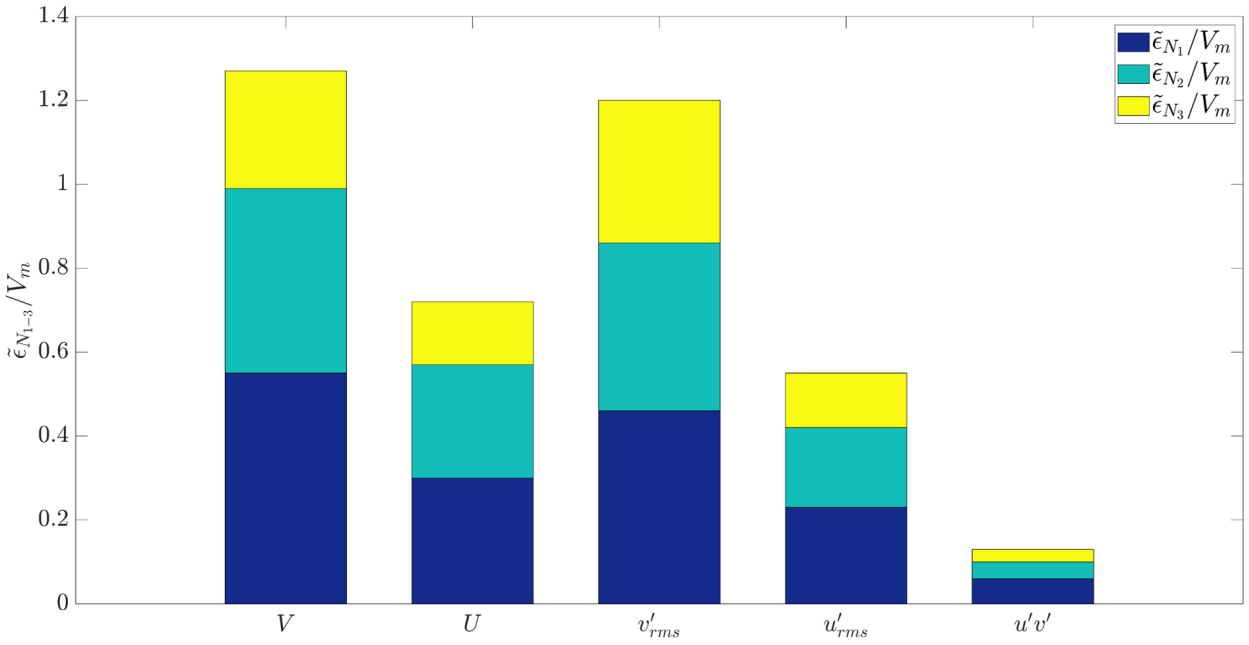

Figure 4.7: The convergence of the statistical results obtained from the TR-PIV of the non-isothermal case of V, U, v'_{rms}, u'_{rms}, and $u'v'$ normalized by V_m. The stacking bar consisting of the three $\tilde{\varepsilon}_{N_1}/V_m$, $\tilde{\varepsilon}_{N_2}/V_m$, and $\tilde{\varepsilon}_{N_1}/V_3$ were $N_1 = 10{,}000$, $N_2 = 15{,}000$, and $N_3 = 30{,}000$ velocity snapshots. For visualization purposes, the $u'v'$ were multiplied by 2.5. The values are summarized in Table 4.4

layers in the vicinity of the jet nozzle, while peaks of u'_{rms} were identified farther downstream, i.e., approximately at $y/D_j = 2.3$ for Re_1, $y/D_j = 4.99$ for Re_3, and $y/D_j = 7.45$ for Re_5 and near the plenum wall where the jet impinged. It is seen that near the outlet, the jet flow develops as a free jet and there is no effect of the jet impingement. Detailed comparisons with other studies of free jets will be discussed later in this paper. Farther downstream at approximately $y/D_j = 8$, the jet flow is influenced by the impingement at the top wall indicated by the appearance of the stagnation region, i.e., a flow region with very small velocity magnitude (≈ 0) in the vicinity of the wall. The color contour of Reynolds stress shown in Figure 4.9 displays the shear layers with positive and negative peaks appearing nearly at the same elevation. The signs of the Reynolds stress $\langle u'v' \rangle$ indicate the rotational signs of a counter-vortex pair formed downstream of the jet nozzle.

Figures 4.10, 4.11, and 4.12 show the mean velocity vector fields with velocity magnitude contour, transverse velocity u'_{rms}, r.m.s fluctuating axial velocity v'_{rms}, r.m.s fluctuating transverse velocity u'_{rms} in (m/s), and Reynolds stress $'v'\rangle$, $(\mathrm{m}^2/\mathrm{s}^2)$ for the non-isothermal plume. As seen in the Figures (4.10, 4.11, and 4.12), the plume velocity reached the maximum values, i.e $V_{cp} = 0.035\ m/s$, far away from the plume inlet, $y/D_j \approx 1.7$, then gradually decreased farther downstream until the plume started to expand in the

Table 4.4: The convergence of the statistical results obtained from the TR-PIV for the non-isothermal case of V, U, v'_{rms}, u'_{rms}, and $u'v'$ normalized by V_m , the convergence consisting of the three $\tilde{\varepsilon}_{N_1}/V_m$, $\tilde{\varepsilon}_{N_2}/V_m$, and $\tilde{\varepsilon}_{N_1}/V_3$ were $N_1 = 10{,}000$, $N_2 = 15{,}000$, and $N_3 = 30{,}000$ velocity snapshots.

	$\tilde{\varepsilon}_v/V_m\%$	$\tilde{\varepsilon}_u/V_m\%$	$\tilde{\varepsilon}_{v'_{rms}}/V_m\%$	$\tilde{\varepsilon}_{u'_{rms}}/V_m\%$	$\tilde{\varepsilon}_{u'v'}/V_m^2\%$
N_1	0.55	0.30	0.46	0.23	0.06
N_2	0.44	0.27	0.40	0.19	0.04
N_3	0.28	0.15	0.34	0.13	0.03

transverse direction after impinging the top upper plenum wall. The transverse velocity u'_{rms} was maximal near the center of the upper plenum wall, where the axial flow hits the wall, and then starts to decrease. Whereas, in the isothermal case, the jet has its maximum velocity near the jet inlet, maximum velocity for the plume was far from the inlet. Turbulent regions were observed at the center of the plume in both directions. The reason behind this behavior might be the low Reynolds number of the flow; for higher Reynolds numbers, such as in the isothermal case, high turbulence is present around the jet shear layers.

In this paragraph, the first- and second-order statistical profiles, such as the mean axial velocity, V, r.m.s fluctuating axial, v'_{rms}, and transverse, u'_{rms}, velocities, and Reynolds stress, $\langle u'v' \rangle$, obtained from TR-PIV measurements for various Reynolds numbers ranging from $Re_1 = 3{,}413$ to $Re_5 = 12{,}819$ of the isothermal and non-isothermal cases are compared.

For the isothermal case, the statistical profiles were interpolated along the horizontal lines $y/D_j = 1$ to $y/D_j = 8$, normalized by the jet velocity, V_c, and compared among those from different Re numbers, and from the studies of Milanovic and Hammad [2010], and Fellouah et al. [2009]. According to Fellouah et al. [2009] and Ball et al. [2012] and as it was discussed in the literature review chapter 2 Section 2.1, the round-free jet discharged into a quiescent environment could be defined by different axial regions, i.e., the near field, the intermediate field, and the far field. The near field of a free jet, typically within $0 \leq y/D_j \leq 7$, is a region of flow establishment where the features of the jet flow and the surrounding mixing zone are interacted. The far field region, i.e., approximately at $y/D_j \geq 30$ [Fiedler, 1998], is the fully-developed region where the jet flow reaches its self-similar region with an appropriate scaling. The intermediate field region lies between the near and far fields, $7 \leq y/D_j \leq 30$ [Fellouah et al., 2009]. Further discussions on the flow regions of jet mixing

in a quiescent environment can be reviewed in Wygnanski and Fiedler [1969], George [1989], Dowling and Dimotakis [1990], Panchapakesan and Lumley [1993], Hussein et al. [1994], Fiedler [1998], Uddin and Pollard [2007], and Ball and Pollard [2008].

In Figure 4.13, the comparisons of mean vertical velocity V/V_c exhibit the development of a jet flow within the near-field region, i.e., $0 \leq y/D_j \leq 7$ [Ball et al., 2012]. The velocity profiles reduced their maximum peaks, and became flatter, and their widths increased farther downstream, indicating the expansion of the jet flow in the axial direction. Additionally, we found that the normalized vertical velocity profiles corresponding to various Reynolds numbers at each axial location follow the same trend and could be depicted by a single curve. The velocity profiles extracted from the studies of Fellouah et al. [2009] for Re = 6,000 and Re = 10,000, and of Milanovic and Hammad [2010] for Re = 14,602 were also overplotted for comparisons. Figure 4.14 shows the comparisons of the r.m.s fluctuating axial velocity, v'_{rms}, profiles along different horizontal lines in the near-field region. Profiles of v'_{rms} depict two local maximum peaks, which appeared at $x/D_j = \pm 0.41$ at $y/D_j = 1$, and started to merge into a single peak farther downstream. The v'_{rms} profiles extracted from the studies of Fellouah et al. [2009] and Milanovic and Hammad [2010] were also plotted for comparisons. As shown, the transverse locations of the v'_{rms} peaks along lines $y/D_j = 1$ and 2 are similar, while the peak locations of the profiles along lines $y/D_j > 3$ are different between the current study and others. Comparisons of r.m.s fluctuating transverse velocity, u'_{rms}, profiles are illustrated in Figure 4.15. The transverse locations and values of u'_{rms} peaks are in good agreement with the work of Fellouah et al. [2009] and Milanovic and Hammad [2010], except those along line $y/D_j = 1$. The peak values of v'_{rms} were found near the jet edge, while the axial locations of u'_{rms} peaks were found farther downstream when the

Reynolds numbers increased, e.g., u'_{rms} reached maximum values at $y/D_j = 2.30$, 3.70, 4.99, 6.35, and 7.45 for Re_1 to Re_5. Figure 4.16 shows the comparisons of Reynolds stress $\langle u'v' \rangle$ profiles along different horizontal lines $y/D_j = 1$ to 8. The Reynolds stress profiles extracted from the study of Fellouah et al. [2009] for Re = 6,000 and 10,000 demonstrate reasonable agreements with the current experimental data, except at $y/D_j = 1$. The large scale vortices cause the momentum of the jet flow to be exchanged around the shear layer. This might have caused the local maximal peaks of the Reynolds stress to be farther downstream, as shown in Fellouah et al. [2009]. It is noteworthy that the results from the studies of Fellouah et al. [2009], and Milanovic and Hammad [2010] were obtained from the experimental studies of a single free jet mixing in the quiescent environment. In our current experimental configuration, the jet flow was discharged from a circular pipe into the volume of the upper plenum where the jet flow impinged to the ceiling height at approximately $11D_j$, and subsequently deflected and developed as a wall jet along the top wall before exiting the plenum. It is reasonable to assume that the jet flow mixing in our study could possess multiple features from the intermediate field of a free jet, and the impinging jet in a closed volume when compared to the flow characteristics of the free jet flow. Therefore, differences in the comparisons of statistical profiles extracted from our current study and others are expected.

For the non-isothermal case, the statistical profiles were interpolated along the horizontal lines $y/D_j \approx 0$ to $y/D_j = 10$, normalized by the jet velocity, V_c. Figure 4.17 shows the profile of normalized mean vertical velocity V/V_c obtained from TR-PIV measurements of a single plume mixing in the upper plenum. Results were interpolated to horizontal lines $y/D_j \approx 0$ to $y/D_j = 10$. The velocity profile started to increase after $y/D_j = 0$ until it reached the maximum at $y/D_j = 3$ and then the peak reduced gradually and near the upper

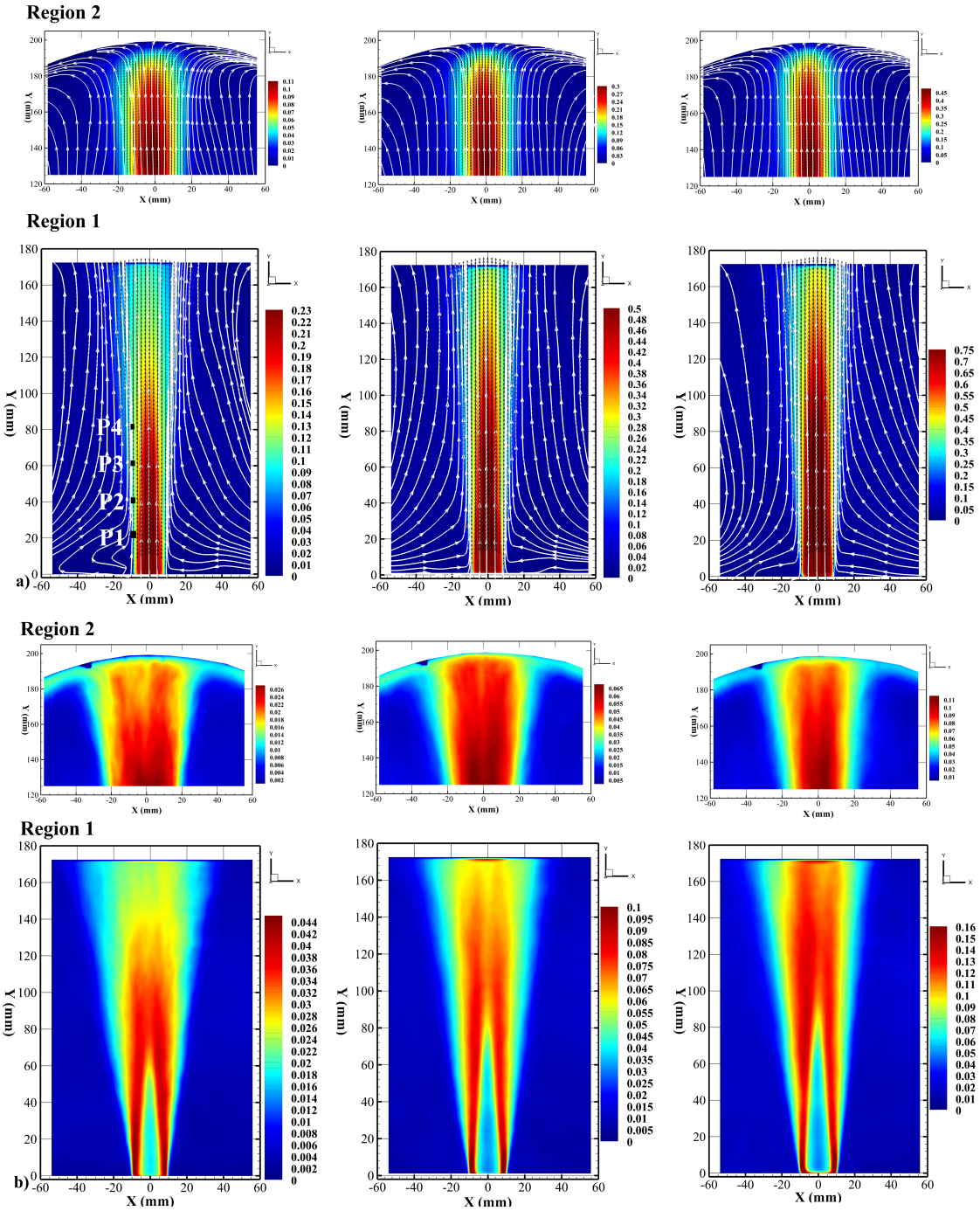

Figure 4.8: TR-PIV results obtained from a single jet mixing in the upper plenum for $Re_1 =$ 3,413 *(left)*, $Re_3 = 7{,}912$ *(center)*, and $Re_5 = 12{,}819$ *(right)*. *(a)* Mean velocity vector fields and mean velocity magnitude contour (m/s), and color contours of *(b)* r.m.s fluctuating axial velocity v'_{rms} (m/s). (Region 1 is close to the jet inlet and Region 2 is close to the upper plenum top wall).

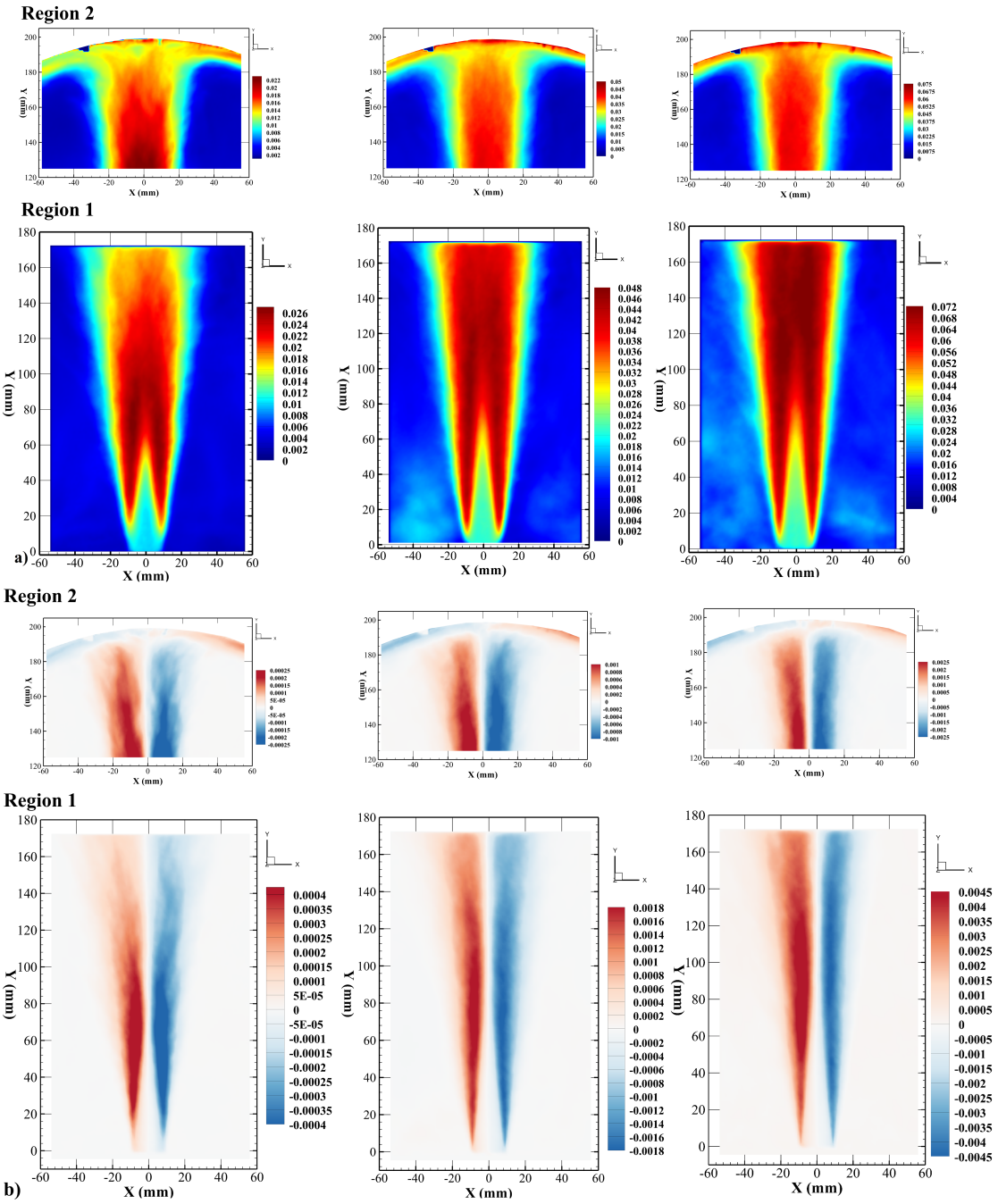

Figure 4.9: TR-PIV results obtained from a single jet mixing in the upper plenum for $Re_1 =$ 3,413 *(left)*, $Re_3 =$ 7,912 *(center)*, and $Re_5 =$ 12,819 *(right)*. *(a)* r.m.s fluctuating transverse velocity u'_{rms} (m/s), and *(b)* Reynolds stress $\langle u'v' \rangle$, (m^2/s^2). (Region 1 is close to the jet inlet and Region 2 is close to the upper plenum top wall).

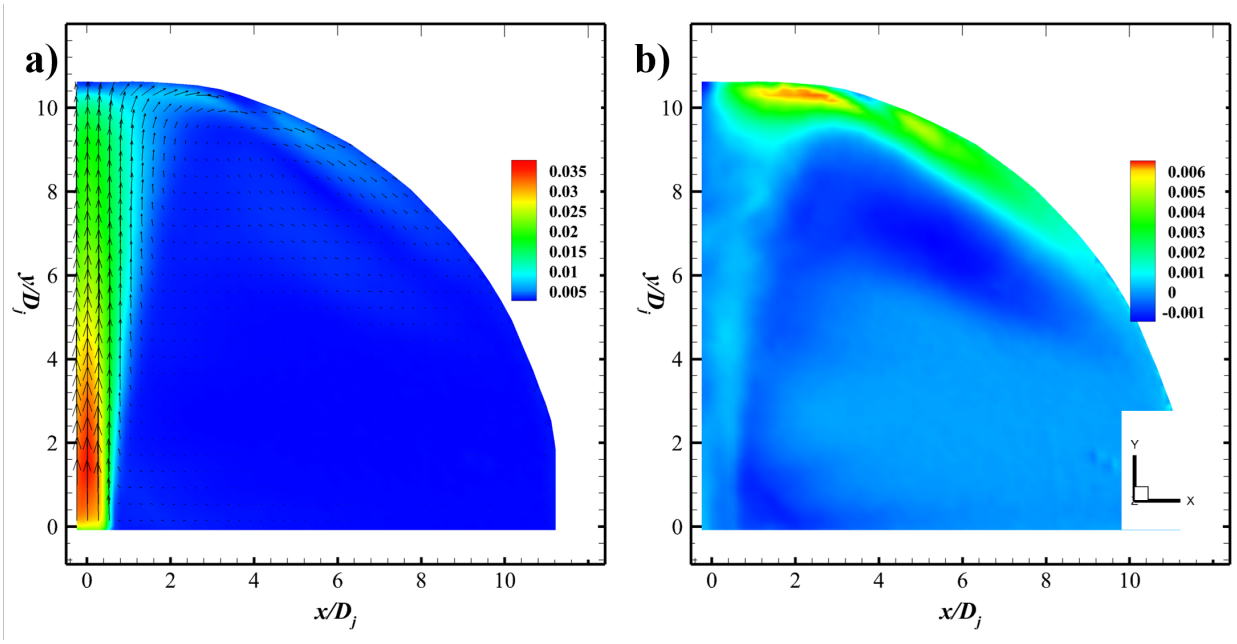

Figure 4.10: TR-PIV results obtained from a single plume mixing in the upper plenum. *(a)* Mean velocity vector fields and mean velocity magnitude contour (m/s), and color contours of *(b)* transverse velocity u'_{rms} (m/s).

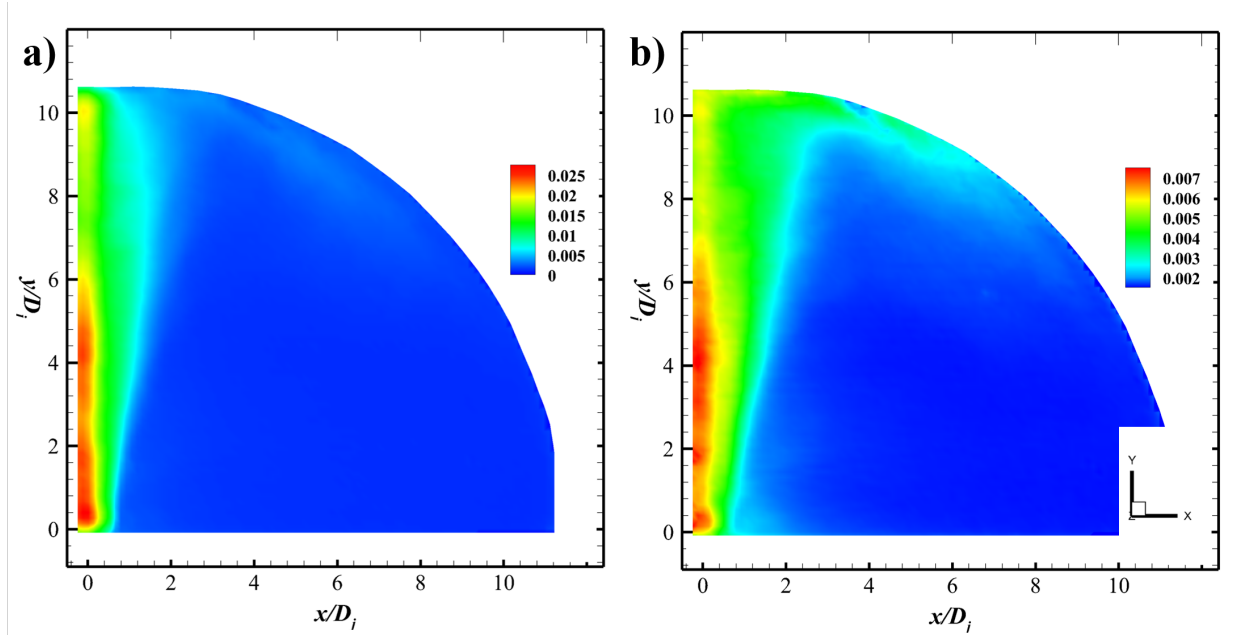

Figure 4.11: TR-PIV results obtained from a single plume mixing in the upper plenum. *(a)* r.m.s fluctuating horizontal velocity v'_{rms} (m/s), and *(b)* r.m.s fluctuating transverse velocity v'_{rms} (m/s).

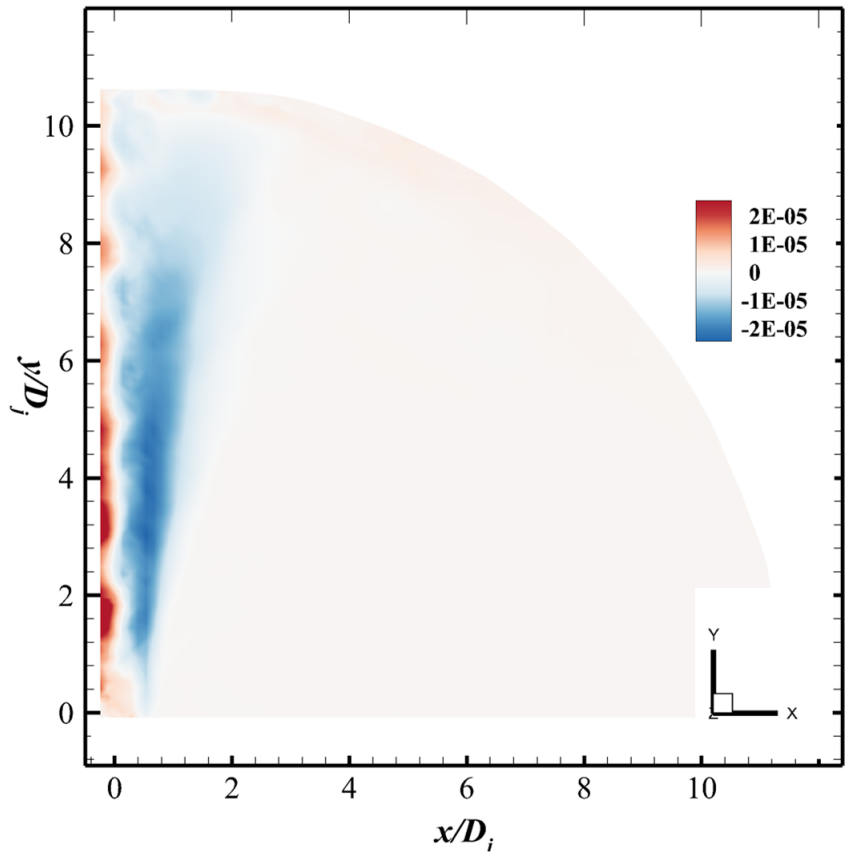

Figure 4.12: TR-PIV results obtained from a single plume mixing in the upper plenum for Reynolds stress $\langle u'v' \rangle$, (m^2/s^2).

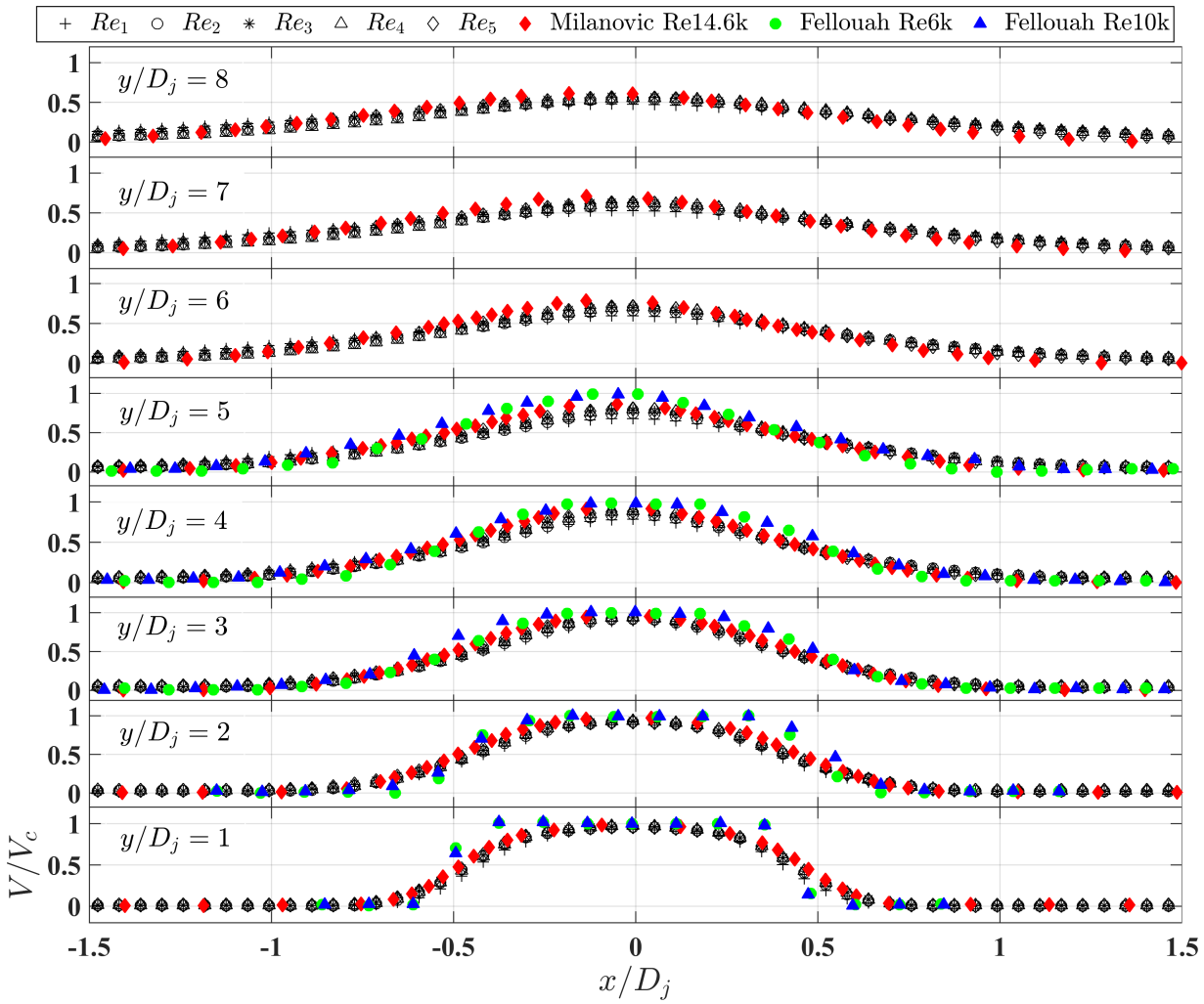

Figure 4.13: Profiles of normalized mean vertical velocity V/V_c obtained from TR-PIV measurements of a single jet mixing in the upper plenum for various Reynolds numbers ranging from Re_1 = 3,413 to Re_5 = 12,819. Results were interpolated to horizontal lines $y/D_j = 1$ to $y/D_j = 8$ and compared to other results from studies of Milanovic and Hammad [2010] (Re = 14,602), and Fellouah et al. [2009] (Re = 6,000 and Re = 10,000). Adapted from [Milanovic and Hammad, 2010] and [Fellouah et al., 2009]

plenum the centerline jet reached almost 50% of the jet velocity, V_c. Additionally, no large changes of different horizontal lines occurred after $x/D_j = 2$, where the flow is far from the plume core. Figure 4.18 shows the r.m.s fluctuating transverse velocity, v'_{rms} profile for different horizontal lines. The local peak was located at the center of plume core, $x/D_j = 0$ and decreased outward. The r.m.s fluctuating transverse velocity, u'_{rms} profile are plotted

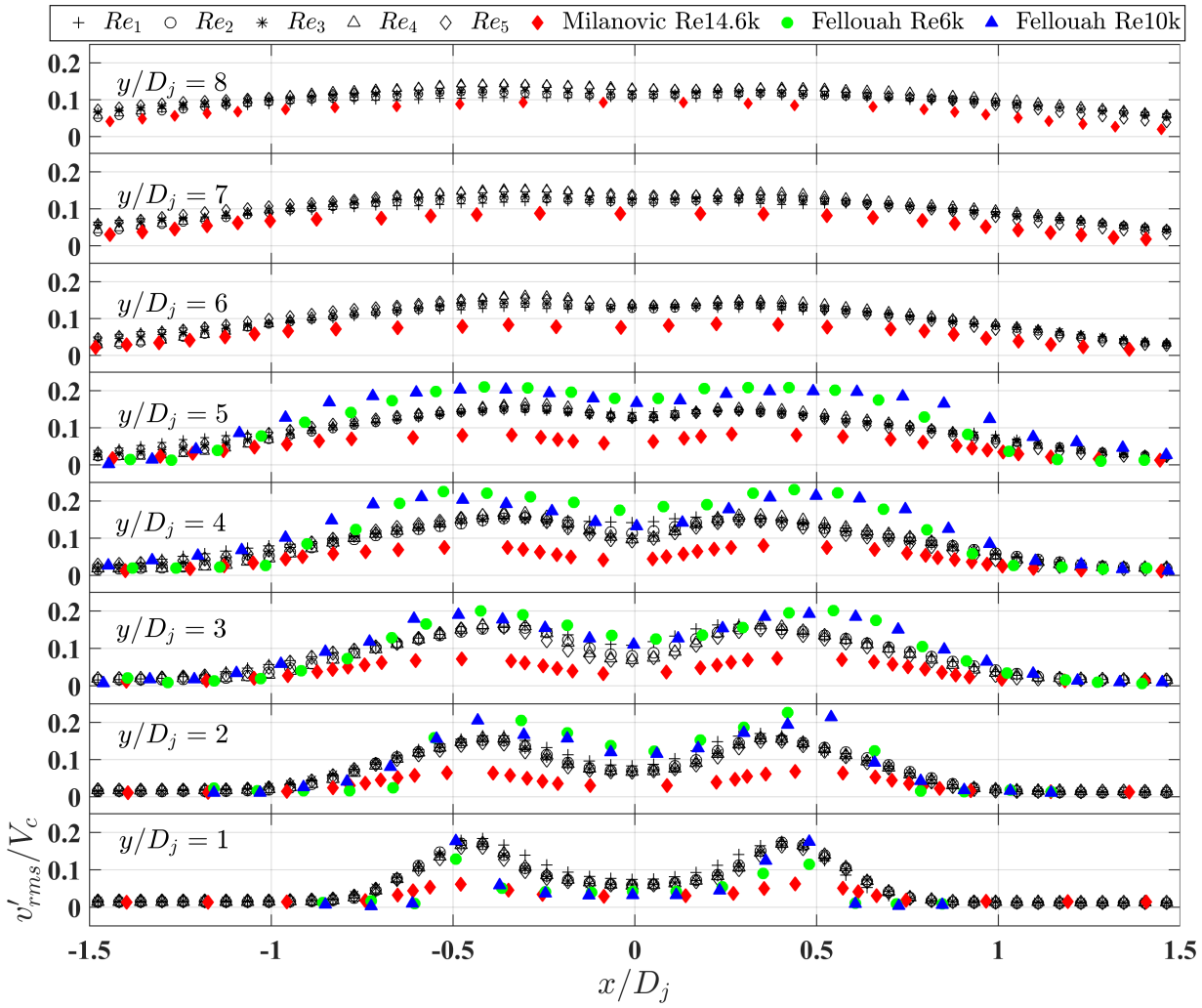

Figure 4.14: Profiles of normalized r.m.s fluctuating vertical velocity v'_{rms}/V_c obtained from TR-PIV measurements of a single jet mixing in the upper plenum for various Reynolds numbers ranging from $Re_1 = 3{,}413$ to $Re_5 = 12{,}819$. Results were interpolated to horizontal lines $y/D_j = 1$ to $y/D_j = 8$ and compared to other results from studies of Milanovic and Hammad [2010] ($Re = 14{,}602$), and Fellouah et al. [2009] ($Re = 6{,}000$ and $Re = 10{,}000$). Adapted from [Milanovic and Hammad, 2010] and [Fellouah et al., 2009]

in Figure 4.19. The peak increased downstream, and the local profile became wider as the upper plenum wall was reached.

Figure 4.20 illustrates the decay rates of the local velocity along the jet center-line (V_m) obtained from the current study of the isothermal case for different Reynolds numbers, for the non-isothemral case, and those extracted from the study of Or et al. [2011] for $Re =$

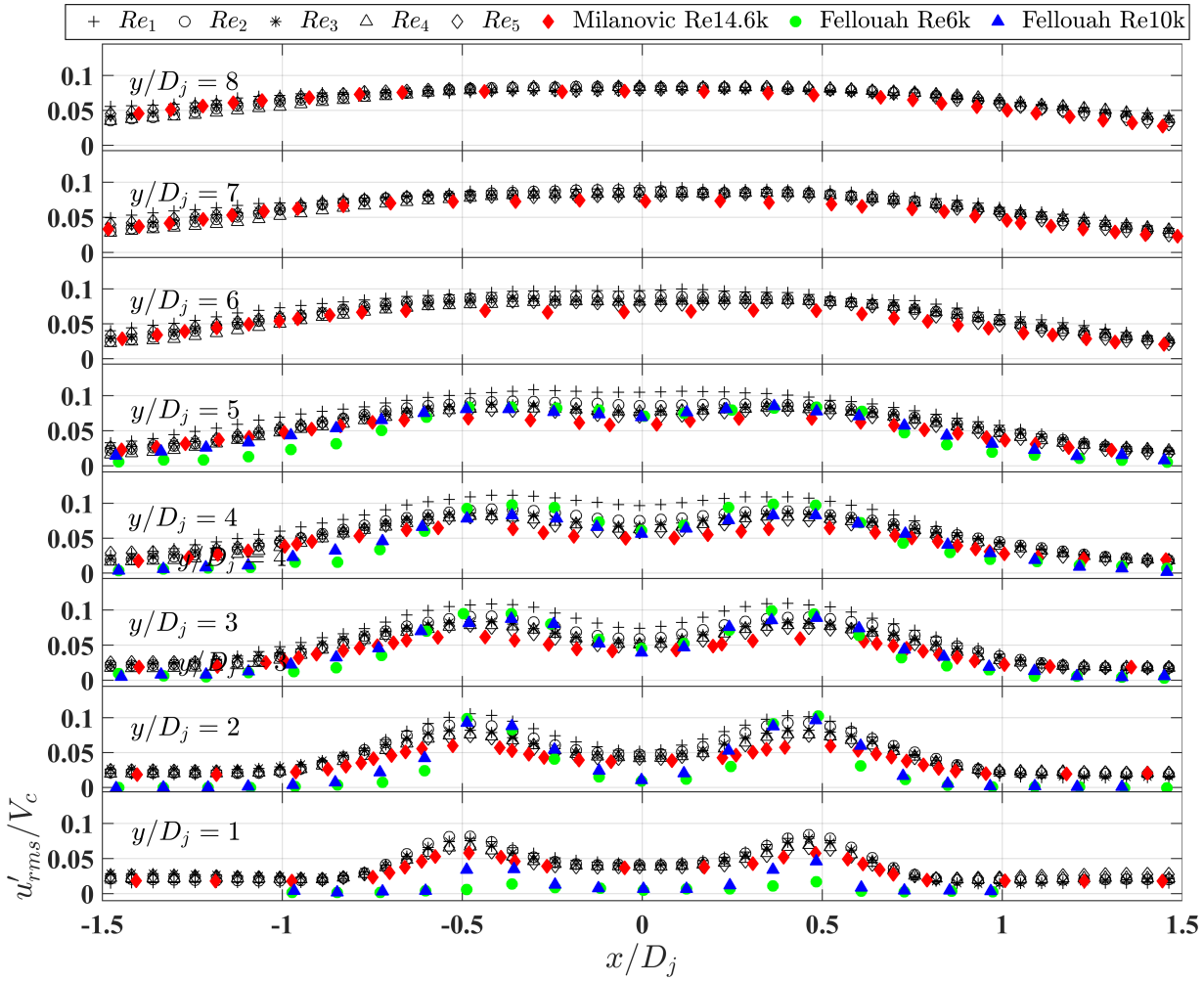

Figure 4.15: Profiles of normalized r.m.s fluctuating transverse velocity u'_{rms}/V_c obtained from TR-PIV measurements of a single jet mixing in the upper plenum for various Reynolds numbers ranging from $Re_1 = 3{,}413$ to $Re_5 = 12{,}819$. Results were interpolated to horizontal lines $y/D_j = 1$ to $y/D_j = 8$ and compared to other results from studies of Milanovic and Hammad [2010] ($Re = 14{,}602$), and Fellouah et al. [2009] ($Re = 6{,}000$ and $Re = 10{,}000$). Adapted from [Milanovic and Hammad, 2010] and [Fellouah et al., 2009]

4,000. The velocity decay profiles of jet flows in the current study depict high fluctuations within the axial height of $y/D_j = 2.5$. Farther downstream, profiles corresponding to $Re >$ 3,413 start to converge into a single profile with the same decay rate. In addition, from $y/D_j = 9$ the decay profiles exhibited an exponential increase due to the effects of jet impingement to the upper plenum top wall. When the flow impinged to the upper plenum

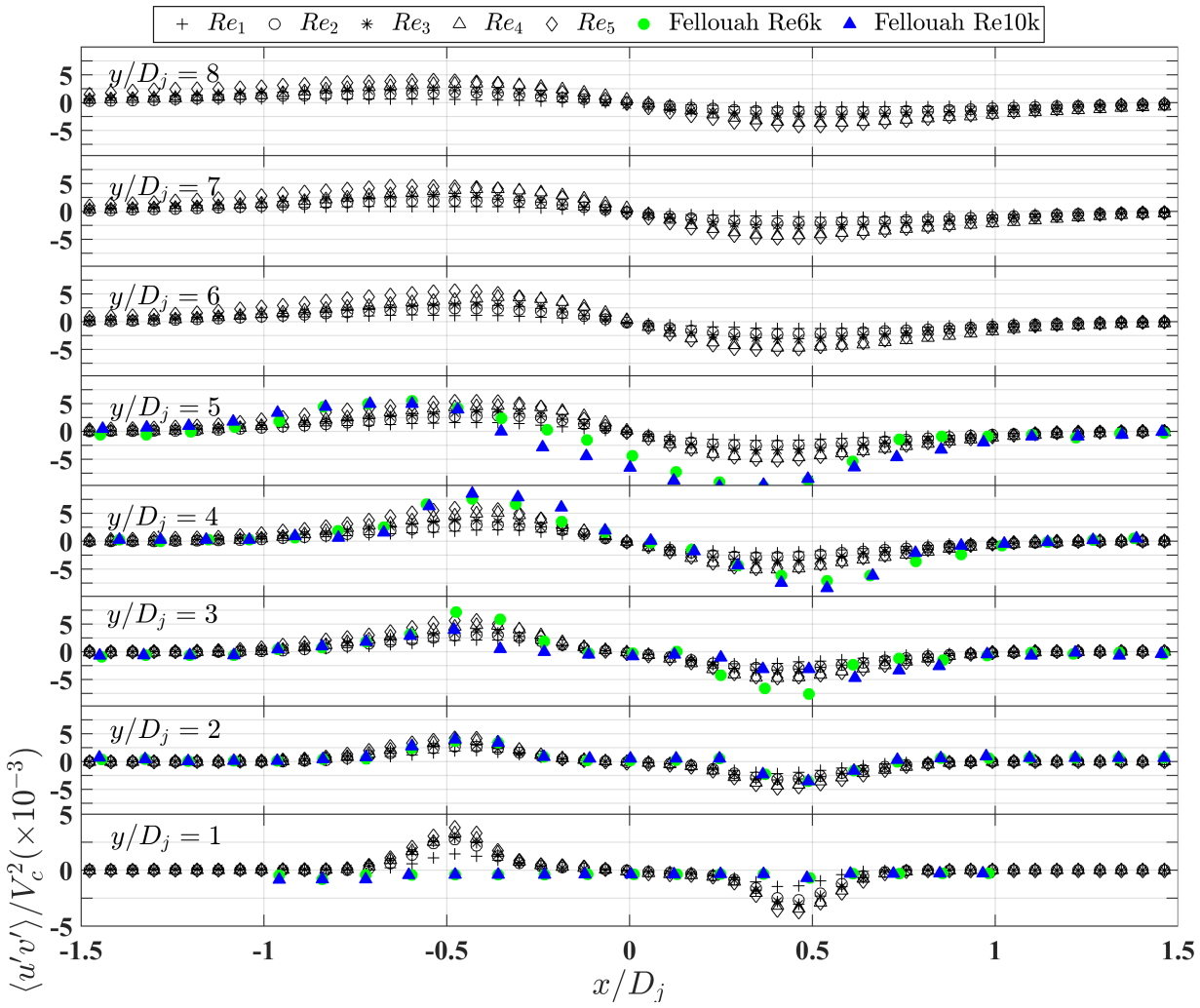

Figure 4.16: Profiles of normalized Reynolds stress $\langle u'v' \rangle / {V^2}_c$ obtained from TR-PIV measurements of a single jet mixing in the upper plenum for various Reynolds numbers ranging from Re_1 = 3,413 to Re_5 = 12,819. Results were interpolated to horizontal lines $y/D_j = 1$ to $y/D_j = 8$ and compared to other results from studies of Fellouah et al. [2009] (Re = 6,000 and Re = 10,000). Adapted from [Fellouah et al., 2009]

wall, the centerline velocity decreased thus the decay profiles increased. Profiles of V_c/V_m from our study with Re_1 = 3,413 and from Or et al. [2011] with Re = 4,000 show the same rate for $y/D_j > 3.5$. It is seen that the decay profiles of the two studies are different within the flow region near the jet exit, i.e., $y/D_j < 3$. The primary reason could be the two large re-circulation regions on both sides of the jet axis that were created by the impingement

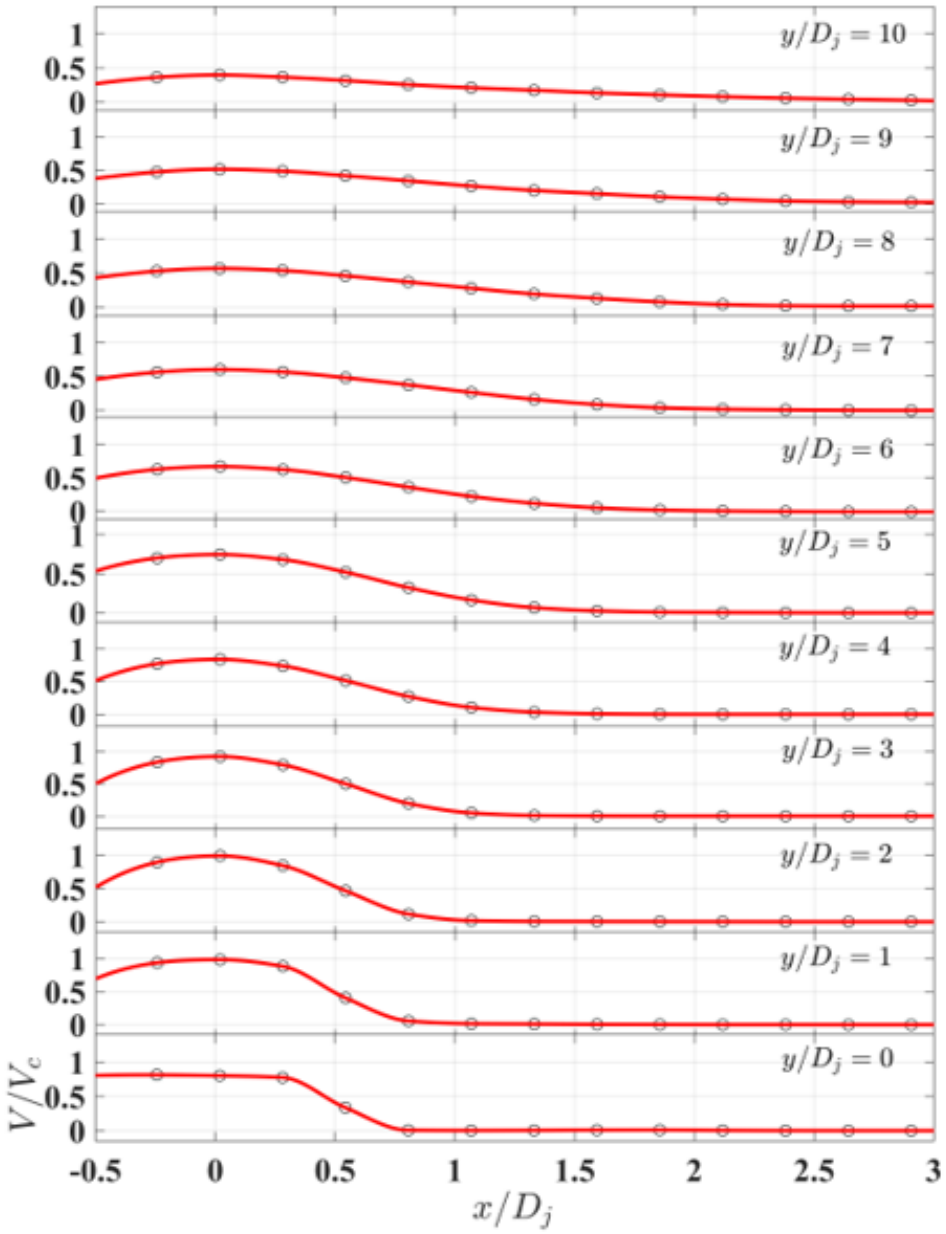

Figure 4.17: Profile of normalized mean vertical velocity V/V_c obtained from TR-PIV measurements of a single plume mixing in the upper plenum. Results were interpolated to horizontal lines $y/D_j \approx 0$ to $y/D_j = 10$

of the jet to the upper plenum' ceiling, the formation of wall jet along the plenum wall, and subsequently the return flow along the transverse direction of the jet exit. Such flow phenomena are illustrated by velocity streamlines in Figure 4.8, and could be reviewed in

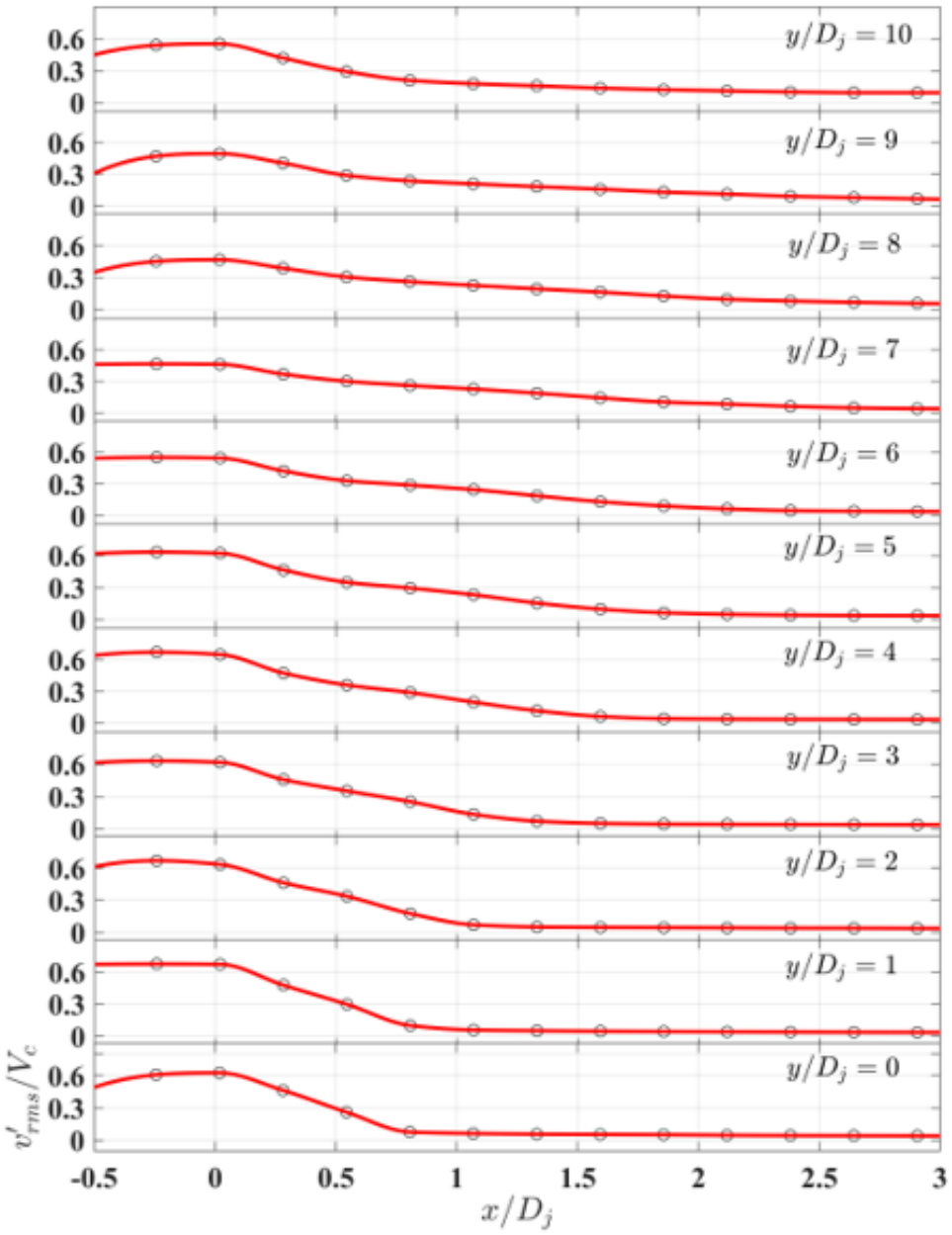

Figure 4.18: Profile of normalized r.m.s fluctuating axial velocity v'_{rms}/V_c obtained from TR-PIV measurements of a single plume mixing in the upper plenum. Results were interpolated to horizontal lines $y/D_j \approx 0$ to $y/D_j = 10$

Alwafi et al. [2018], in which the authors showed a large-view of velocity fields within the volume of the upper plenum. A close-up view in Figure 3.2 depicts the velocity streamlines of a single jet mixing in the upper plenum from the full-field velocity measurements of Alwafi

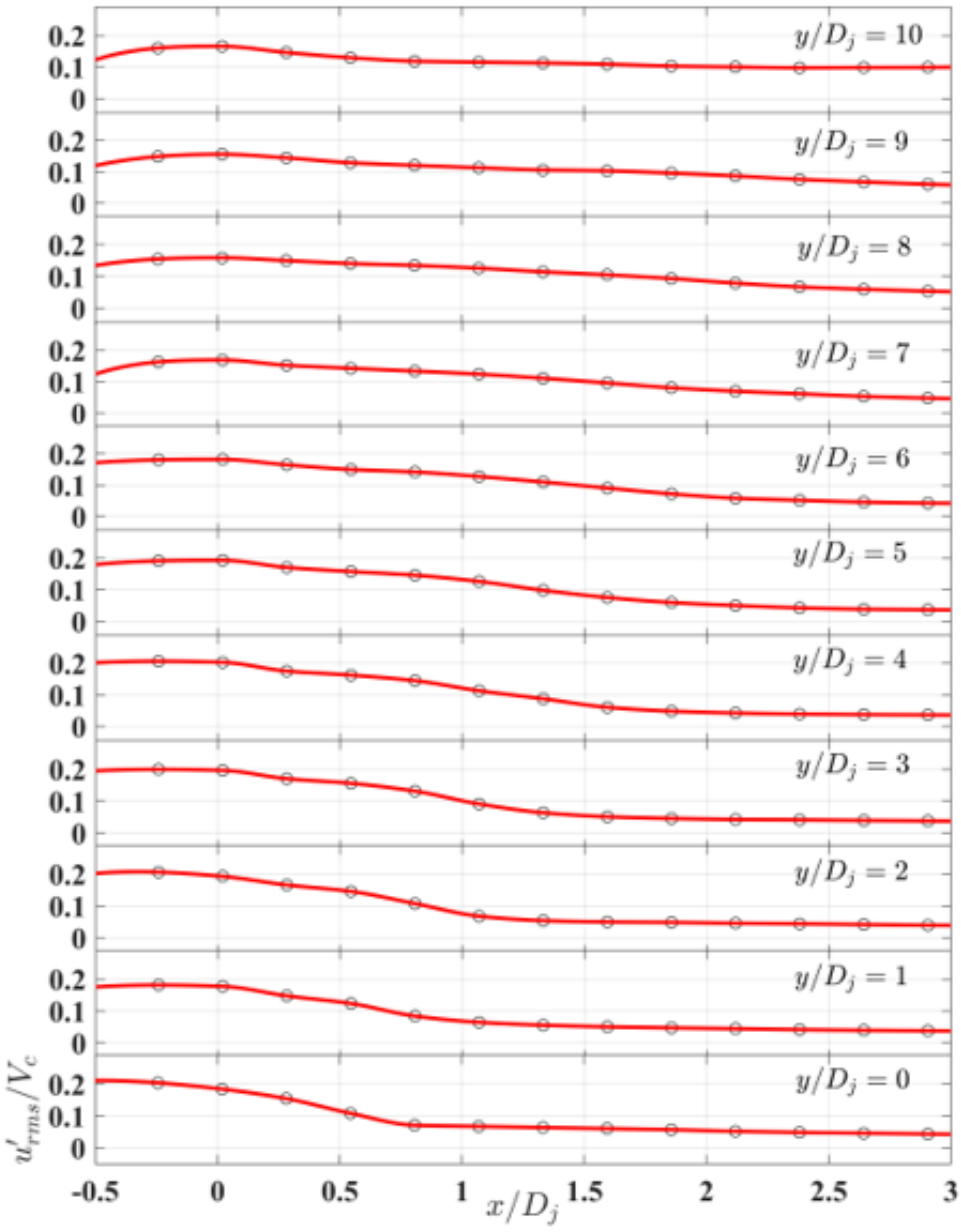

Figure 4.19: Profile of normalized r.m.s fluctuating transverse velocity u'_{rms}/V_c obtained from TR-PIV measurements of a single plume mixing in the upper plenum. Results were interpolated to horizontal lines $y/D_j \approx 0$ to $y/D_j = 10$

et al. [2018]. Preliminary results obtained from numerical simulations of the single jet mixing in the upper plenum for $Re_1 = 3{,}413$ can be reviewed in Busco et al. [2018].

The decay of the non-isotheraml case of the plume can be seen in Figure 4.20. The

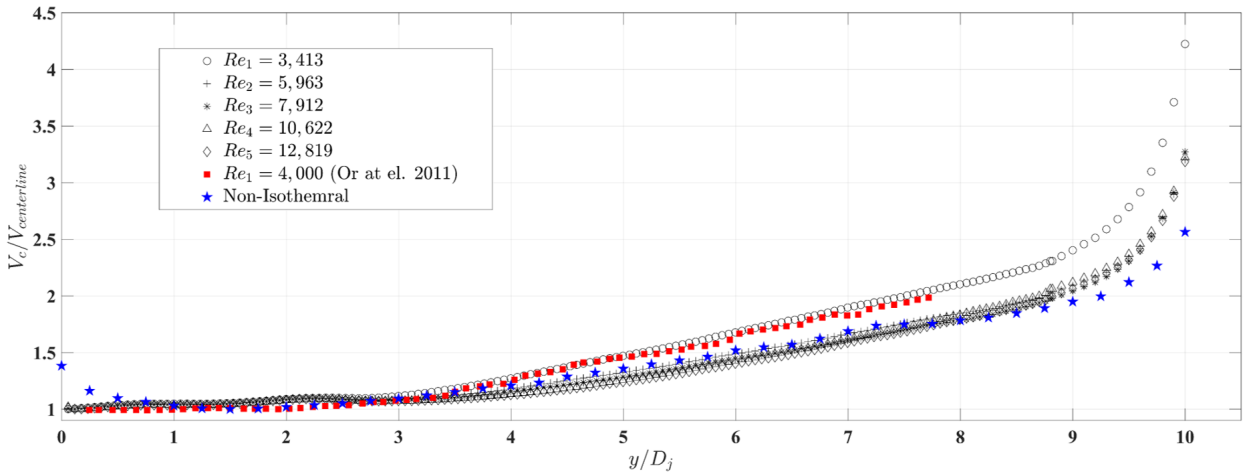

Figure 4.20: Decay profiles of local velocity along the jet center-line for current study with Re_1 to Re_5, and a profile from Or et al. [2011] is also overplotted for the isothemral case. and the blue line is for the non-isothermal case. The jet impingement is at $y/D_j = 10.3$

profile decreases from the plume inlet until it reaches a minimum at $y/D_j = 1$, and then gradually increases until $y/D_j = 9$, then the decay profiles change to an exponential increase. Comparing the decay profiles of the isothermal and non-isothermal cases, indicates they are similar, with the main difference occurring near the jet/plume inlet where the isothermal case shows a stable decay and then increase whereas the non-isothermal case shows an initial drop and after that an increase. This drop at the plume is caused by the plume having a maximum velocity farther from the inlet due to the return flow.

Figure 4.21 shows the self-similar profile of the mean axial velocity in different axial regions. The points fit with the Gaussian distribution line. This was done by finding the jet width $x_{1/2}$ (b); which defined as the radial location where the axial velocity is half its maximum. The velocity was then normalized by its maximum. It also should be mentioned that the near the jet inlet, $y/d_j = 0$ to $y = 4$, the points do not fit with the curves and this is due to the self-similarity occur far from the jet inlet [Alwafi et al., 2018].

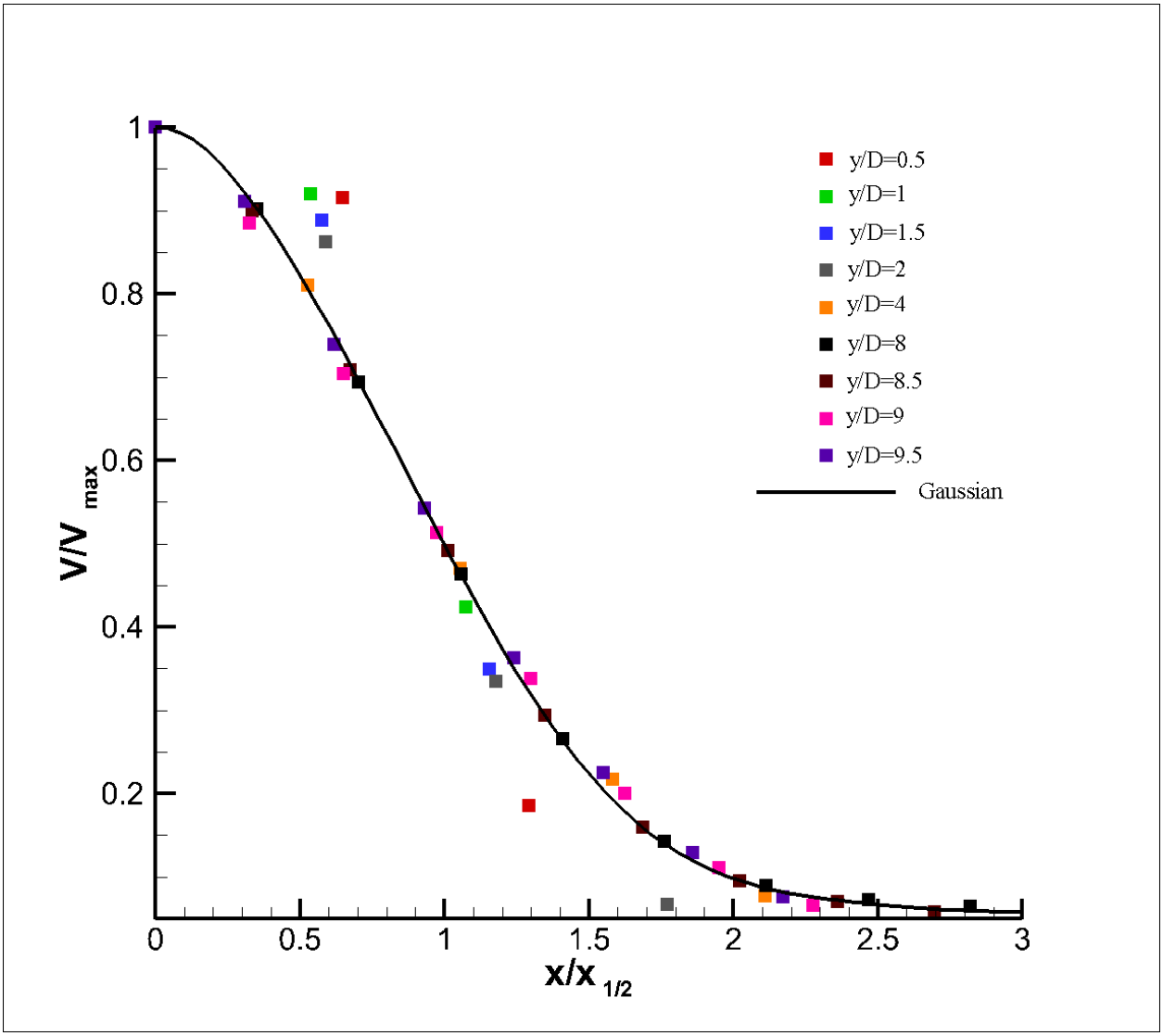

Figure 4.21: Self-similar profile of the mean axial velocity for Re_1, isotheraml case, reprinted from [Alwafi et al., 2018]

4.1.3 Spatial-temporal velocity cross-correlation analysis

In this section, to gain an insight into the flow characteristics of a single jet/plume mixing in the upper plenum, spatial-temporal turbulent velocity cross-correlations on the TR-PIV velocity vector fields obtained for both cases, isothermal and non-isothermal, were performed. The previous studies of Romano [1995], Ruiz et al. [2010], Nguyen et al.

[2017], Nguyen and Hassan [2017a], Nguyen et al. [2018], and Nguyen et al. [2019b] have illustrated that velocity correlation functions can provide more insight into the shapes, sizes and contributions of the coherent structures to the flow mixing. It is noted that the calculations of two-point velocity cross-correlations are enabled by the full-field TR-PIV velocity measurements, while such calculations are not feasible for the single point measurement techniques, such as hot-wire and LDV. The spatial-temporal velocity cross-correlation functions are defined as

$$R_{\boldsymbol{uu}}(\boldsymbol{x}_r, \boldsymbol{\eta}, \tau) = \frac{\langle \boldsymbol{u}'(\boldsymbol{x}_r, t) \times \boldsymbol{u}'(\boldsymbol{x}_r + \boldsymbol{\eta}, t + \tau) \rangle}{\sqrt{\langle \boldsymbol{u}'^2(\boldsymbol{x}_r, t) \rangle} \sqrt{\langle \boldsymbol{u}'^2(\boldsymbol{x}_r + \boldsymbol{\eta}, t) \rangle}}. \tag{4.2}$$

where $\langle . \rangle$ is the ensemble-averaged operator, $\boldsymbol{u}'$ is the fluctuating velocity, τ is the time delay, $\boldsymbol{x}_r$ is the spatial location of the reference point, and $\boldsymbol{\eta}$ is the spatial separation between two points. A special case in this equation occurs when $\tau = 0$, allowing the calculation of spatial correlation length scale, i.e., $R_{\boldsymbol{uu}0} = R_{\boldsymbol{uu}}(\boldsymbol{x}_r, \boldsymbol{\eta}, 0)$ as a function of the separation $\boldsymbol{\eta}$. The integral length scale can then be found from the correlation length scale as

$${}^{k}L_{\boldsymbol{x}} = \int_0^{\infty} R_{\boldsymbol{uu}}(\boldsymbol{x}_r, \boldsymbol{\eta}_k, 0) d\boldsymbol{\eta}, \tag{4.3}$$

where the superscript k is the direction of the separation along with the integration, and ${}^{k}L_{\boldsymbol{x}}$ are the characteristic length scales of the energy containing the turbulent eddies. Following the calculations previously performed by Romano [1995], Falchi and Romano [2009], Nguyen and Hassan [2017b], and Nguyen et al. [2017], for this experiment the integral length scales ${}^{k}L_x$ and ${}^{k}L_y$ were estimated by searching for the separation lengths where R_{uu0} and R_{vv0}

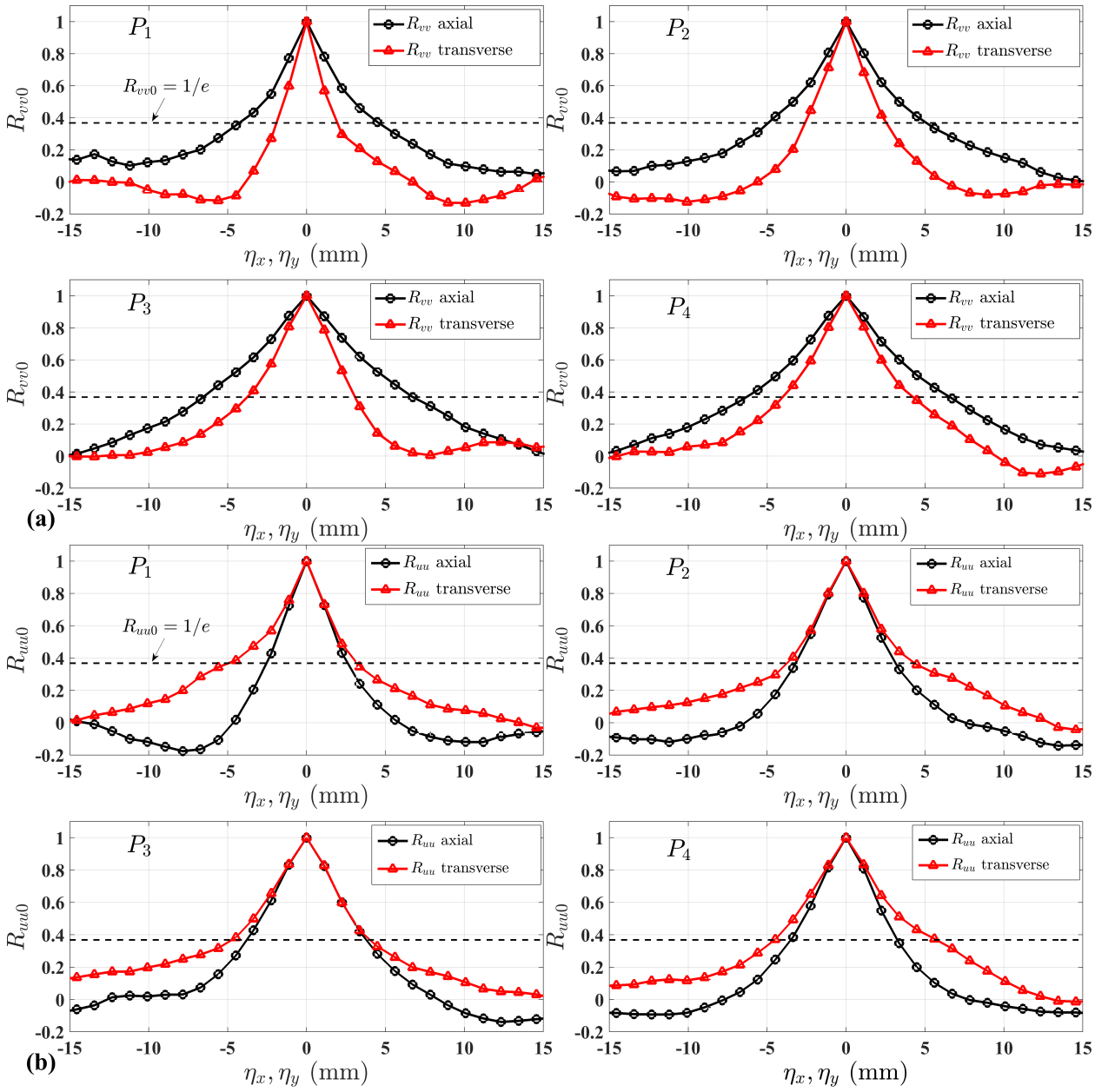

Figure 4.22: Spatial turbulent velocity cross-correlations (a) R_{vv0} and (b) R_{uu0} computed at four referenced points, i.e. $P_1(-9.5, 19.05)$ mm, $P_2(-9.5, 38.1)$ mm, $P_3(-9.5, 57.15)$ mm, and $P_4(-9.5, 76.2)$ mm, using TR-PIV velocity vector fields obtained at $Re_1 = 3{,}413$.

reached $1/e \cong 0.37$ instead of integration up to infinity.

Figures 4.22 and 4.23 display the profiles of the spatial turbulent velocity cross-correlations computed in both the axial and transverse directions using the TR-PIV

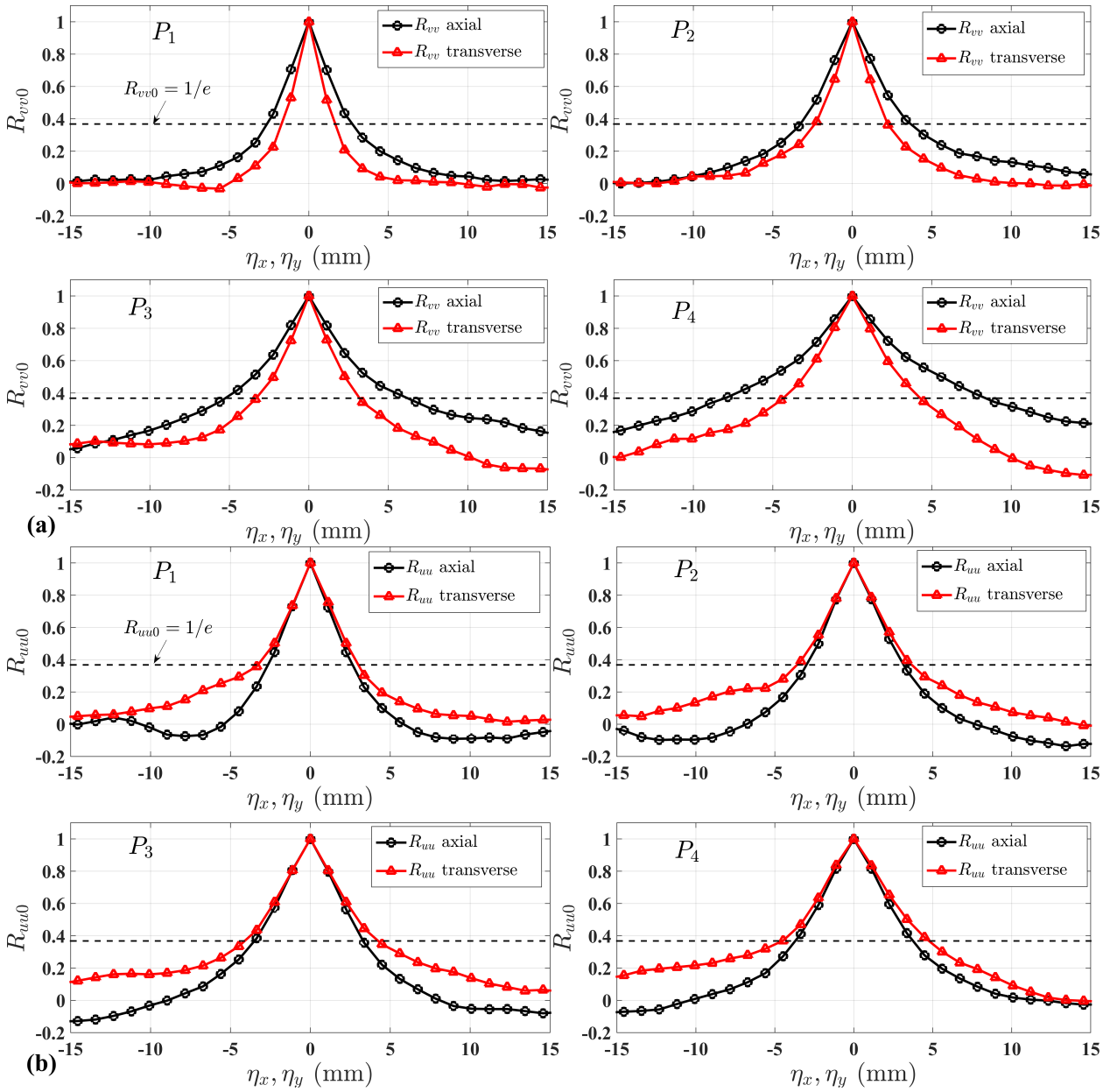

Figure 4.23: Spatial turbulent velocity cross-correlations (a) R_{vv0} and (b) R_{uu0} computed at four referenced points, i.e. $P_1(-9.5, 19.05)$ mm, $P_2(-9.5, 38.1)$ mm, $P_3(-9.5, 57.15)$ mm, and $P_4(-9.5, 76.2)$ mm, using TR-PIV velocity vector fields obtained at $Re_4 = 10{,}622$.

velocity fields for the isothermal case of $Re_1 = 3{,}413$ and $Re_4 = 10{,}622$, respectively. Four referenced points, whose coordinates were $P_1(-9.5, 19.05)$ mm, $P_2(-9.5, 38.1)$ mm, $P_3(-9.5, 57.15)$ mm, and $P_4(-9.5, 76.2)$ mm, were selected. These points were located along

the jet shear layer as shown in Figure 4.8, and Figure 4.26 shows the profiles of the spatial turbulent velocity cross-correlations in the non-isothermal case. Four referenced points were also chosen and their coordinates were $P_1(9.5, 19.05)$ mm, $P_2(9.5, 57.15)$ mm, $P_3(9.5, 114.3)$ mm, and $P_4(9.5, 171.45)$ mm. In Figures 4.22, 4.23, and 4.26, the abscissa, η_x and η_y, represent the spatial distances from the referenced points to others along the corresponding $x-$ and $y-$ directions, respectively. The two-point cross-correlations R_{uu0} and R_{vv0} exhibited the maximum value when $\eta = 0$, and decreased when the separation length increased. In Figures 4.22, 4.23, and 4.26, one could directly estimate the integral length scales by searching for the intersections between the spatial correlation profiles and horizontal lines $R_{uu0} = 0.37$ and $R_{vv0} = 0.37$. It is seen that the integral length scales had greater values when estimated along the primary directions, i.e., ${}^{x}L_x > {}^{y}L_x$ and ${}^{y}L_y > {}^{x}L_y$. In addition, the profiles of the two-point correlations depict the local maximum and minimum with periodically alternating peaks as η increases. An explanation for such observations is the spatially correlated flow regions along the axial and transverse directions induced by the movement of vertices generated from the jet shear layers [Nguyen and Hassan, 2017a; Romano, 1995]. For Re_1 = 3,413 (c.f. Figure 4.22), the integral length scales estimated at points P_{1-4} are $({}^{x}L_y, {}^{y}L_y) = (1.74, 4.54)$, $(2.54, 4.94)$, $(3.04, 6.74)$, and $(4.24, 6.54)$, and $({}^{y}L_x, {}^{x}L_x) = (3.14, 2.54)$, $(4.34, 3.04)$, $(3.94, 3.74)$, and $(5.54, 3.24)$, respectively. For Re_4 = 10,622 (c.f. Figure 4.23) the values at P_{1-4} were estimated as $({}^{x}L_y, {}^{y}L_y) = (1.44, 2.64)$, $(2.14, 3.54)$, $(3.14, 5.94)$, and $(4.24, 8.24)$, and $({}^{y}L_x, {}^{x}L_x) = (2.94, 2.54)$, $(3.64, 3.14)$, $(4.04, 3.34)$, and $(4.74, 3.64)$, respectively.

Another way of calculating and showing the two-point spatial cross correlation is depicted in Figures 4.24 and 4.25. These figures show the calculated color contours

of the two-point spatial cross correlation for the fluctuating velocities, u' and v', along the shear layers of the jet and for different vertical locations, using the TR-PIV velocity vector fields for the Reynolds numbers Re_1 = 3,413 and Re_2 = 12,819. The reference points were located at the shear layers for the transverse direction and for the axial direction. They were chosen to be $(2 \times D_j)$, $(4 \times D_j)$, $(6 \times D_j)$, and $(9.5 \times D_j)$. Their coordinates $P_{n_{(\pm)}}(x, y)$ are $P_{2_{(\pm)}}(\pm 11.34, 38.1)mm$, $P_{4_{(\pm)}}(\pm 15.82, 76.2)mm$, $P_{6_{(\pm)}}(\pm 16.94, 114.3)mm$, $P_{8_{(\pm)}}(\pm 21.42, 152.4)mm$, and $P_{9.5_{(\pm)}}(\pm 23.8, 181)mm$, where n is the point number in reference to D_j and $(\pm)$ is their location in the transverse direction. Figure 4.24 (top) illustrates the locations of these points. In both Figures 4.24 and 4.25, the correlations R_{uu0} and R_{vv0} reach their maximum unity values at the selected points and then decrease in both directions as the separation distance increases. In Figure 4.24, the shape of the spatial cross correlations of the fluctuating velocity u', i.e. R_{uu0}, are approximately the same for both the Reynolds numbers; moreover, they are starting to increase downstream. The shape of the R_{uu0} is wide on the x direction, forming an oval shape. It is not a symmetrical shape since the decreasing near the center line $x = 0$ is much faster than that of the other direction and since the y decrease is slower. This phenomena occurs because of the return flow that comes after the flow impinges the wall of the upper plenum and changes from axial direction to transverse direction. On the other hand, Figure 4.25 shows that the shape of the spatial cross correlations of the fluctuating velocity v', i.e. R_{vv0}, is more uniform than that of the R_{uu0}. It starts to increase as it goes downstream. The effect of the return flow is seen at points P_8 and $P_{9.5}$ where the decrease in correlation is slower than it is at points P_2, P_4, and P_6.

Similarly, the integral length scales were estimated for various points distributed

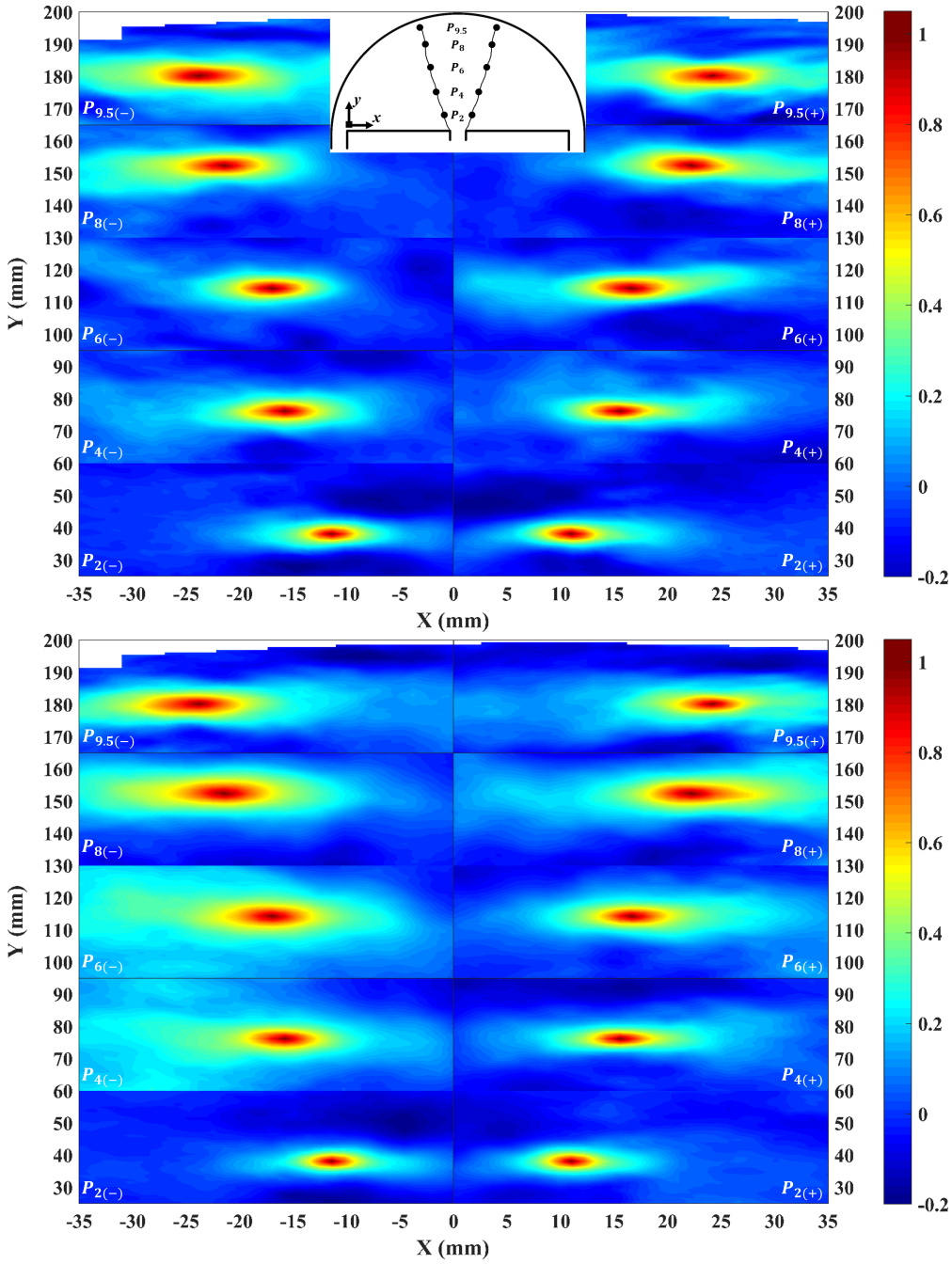

Figure 4.24: The contour maps of two-point spatial cross correlations of the fluctuating u' of Re_1 = 3,413 (top) and Re_2 = 12,819 (bottom) calculated by using TR-PIV velocity vector fields. The reference points, as shown in the figure, are located at the shear layers of the jet for different vertical locations, $P_{2_{(\pm)}}(\pm 11.34, 38.1)mm$, $P_{4_{(\pm)}}(\pm 15.82, 76.2)mm$, $P_{6_{(\pm)}}(\pm 16.94, 114.3)mm$, $P_{8_{(\pm)}}(\pm 21.42, 152.4)mm$, and $P_{9.5_{(\pm)}}(\pm 23.8, 181)mm$.

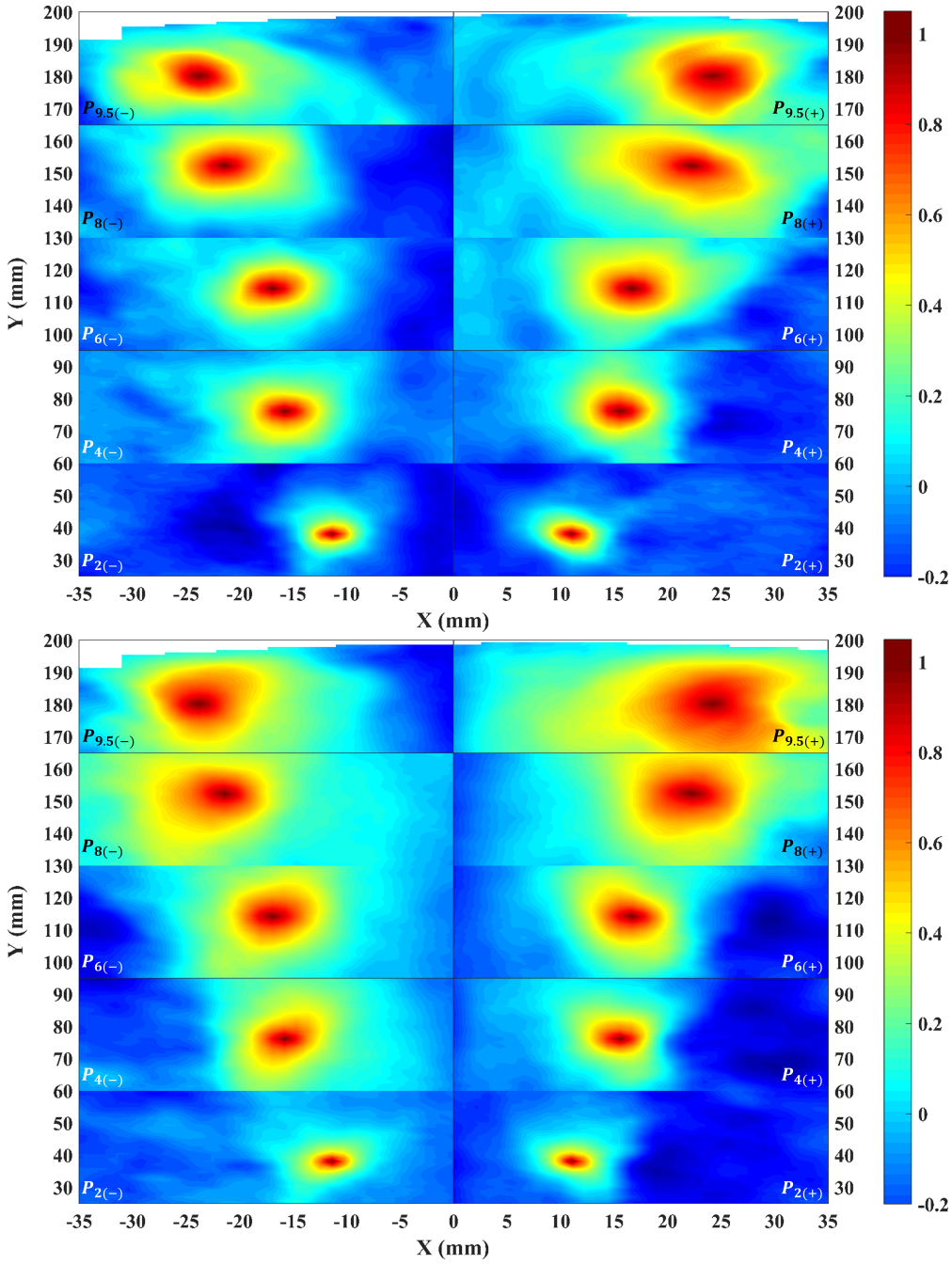

Figure 4.25: The contour maps of two-point spatial cross correlations of the fluctuating v' of $Re_1 = 3{,}413$ (top) and $Re_2 = 12{,}819$ (bottom) calculated by using TR-PIV velocity vector fields. The reference points, as shown in the figure 4.24, are located at the shear layers of the jet for different vertical locations, $P_{2_{(\pm)}}(\pm 11.34, 38.1)mm$, $P_{4_{(\pm)}}(\pm 15.82, 76.2)mm$, $P_{6_{(\pm)}}(\pm 16.94, 114.3)mm$, $P_{8_{(\pm)}}(\pm 21.42, 152.4)mm$, and $P_{9.5_{(\pm)}}(\pm 23.8, 181)mm$.

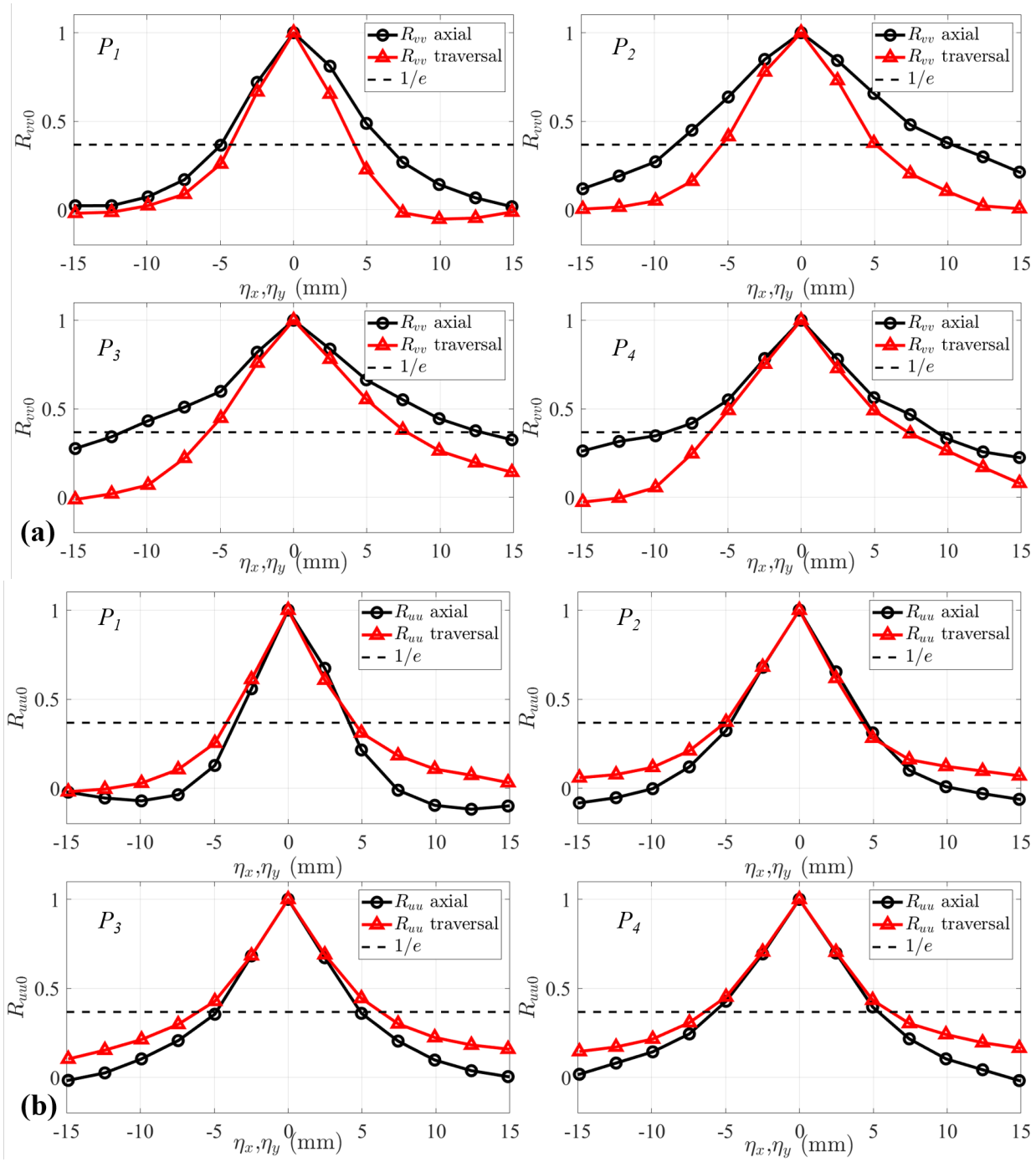

Figure 4.26: Spatial turbulent velocity cross-correlations (a) R_{vv0} and (b) R_{uu0} computed at four referenced points, i.e. $P_1(9.5, 19.05)$ mm, $P_2(9.5, 57.15)$ mm, $P_3(9.5, 114.3)$ mm, and $P_4(9.5, 171.45)$ mm, using TR-PIV velocity vector fields obtained for the non-isothermal case.

along the axial line ($x/D_j = -0.5$) with y/D_j ranging from 1 to 10 for various Reynolds numbers of the isothermal case and non-isothermal case. Figure 4.27 illustrates the estimated integral length scales that are normalized by D_j and plotted for all the studied Reynolds numbers. Figure 4.27 shows that for all the Reynolds numbers, the integral length scales linearly increase farther downstream direction, such observation was similarly found and discussed in the free jet flow previous study of Yuu et al. [1979]. However, from $y/D_j =$ 8 to 10, the effects of jet flow impingement can be seen as the decrease of the integral length scales. This could be related to the spanwise vortices created from the shear layers that evolved and enlarged while moving farther downstream. When the jet flow impinged to the upper plenum top wall, the direction of the flow changed from the axial to transverse direction. Such flow interaction caused the decreasing at the integral length scale. For the ${}^{y}L_y$ of the non-isothermal case, we are seeing a peak at $y/D_j = 6$ and decreased after that. One may also find that the integral length scale ${}^{y}L_y$ exhibits the highest value compared to the others because they were estimated along the dominant flow direction.

4.1.4 Spectral analysis of TR-PIV results

The calculations of two-point turbulent velocity cross-correlations R_{uu0} and R_{vv0} allow for the estimation of integral length scales related to the sizes of the vortices appearing in the jet flow mixing. The spectral analysis on the turbulent velocities can provide the information on the shedding frequency of the large scale coherent structures. Spectral analyses to the fluctuating velocities u' and v' obtained at spatial points P_1, P_2, P_8 and P_9 were performed. The spatial locations of these points are denoted as $(x_{P_{1-3}}, y_{P_{1-3}})$ In addition, we computed the squared coherent functions between points P_{1-3} and the surrounding points

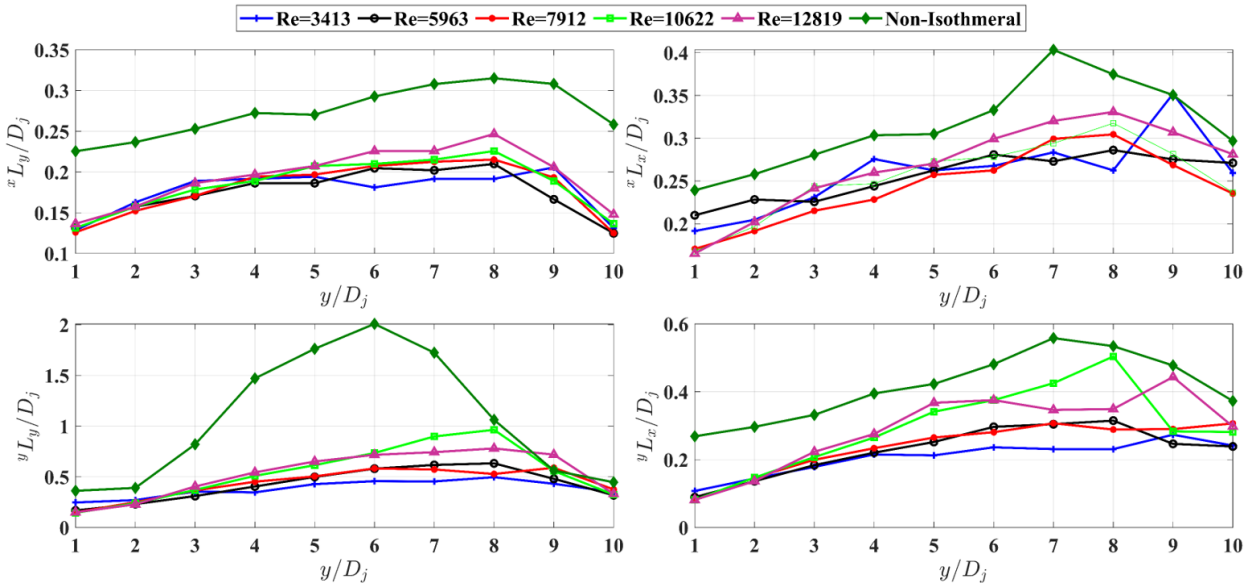

Figure 4.27: Normalized integral length scales, ${}^{x}L_y/D_j$, ${}^{x}L_x/D_j$, ${}^{y}L_y/D_j$, and ${}^{y}L_x/D_j$, computed along the axial line ($x/D_j = -0.5$) for various Reynolds numbers (isothermal), Re_1 = 3,413, Re_2 = 5,963, Re_3 = 7,912, Re_4 = 10,622, and Re_5 = 12,819 and non-isothermal case.

with various separation distances along the axial direction, i.e., ($x_{P_{1-3}}$,$y_{P_{1-3}}+\eta$). The squared coherent function between two points is calculated as

$$C_{AB}(f) = \frac{|P_{AB}(f)|^2}{P_{AA}(f) \cdot P_{AB}(f)} \tag{4.4}$$

where $P_{AA}(f)$, $P_{BB}(f)$ and $P_{AB}(f)$ are the power spectral densities (PSDs) and the cross power spectral density of points A and B, respectively. Romano [1995] discussed that the coherent function $C_{AB}(f)$ represents the portion of the signal at B and at a frequency f that is accounted for by the signal at A.

Figures 4.28 and 4.29 depict the spectral analysis to the fluctuating velocities u' and v' obtained from the TR-PIV measurements of a single jet mixing in the upper plenum for Re_5 = 12,819. The PSDs calculated at points P_1, P_2, and P_3 (near the jet inlet) and P_8 and P_9

(near the upper plenum wall) are displayed as curves with $\eta = 0$. In addition, PSDs computed at the surrounding points with a separation length of $\eta = 2.13$ mm, i.e., approximately the integral length scale estimated at $y/D_j = 1$, are illustrated. The PSD was computed using Welch's periodogram method [Welch, 1967], where the window length had 1,024 samples and 50% sample overlapping. Figures 4.28 and 4.29 show that the PSDs computed at points P_{1-2},P_{8-9} and those computed at points with $\eta = 2.13$ mm exhibit the similar patterns with the same peaks and frequencies. Overall, the PSDs computed at points P_1 and P_2 exhibited strong peaks at 2 Hz and 6 Hz, and 5 Hz and 10 Hz, respectively, while the PSDs calculated at points P_8 and P_9 showed strong peaks at 4 Hz and 10 Hz. The analysis of the square coherent function was performed to study the signal relations between various spatial points with respect to the signal frequency. Figure 4.30 shows the squared coherent functions $C_{xy}(f)$ computed at points P_{1-4} and the surrounding points with different separation distances of $\eta = 1.12$, 2.24, 3.36, and 19.04 mm, while Figure 4.31 shows the squared coherent functions $C_{xy}(f)$ computed at points P_8 and P_9 with different separation distances of $\eta = 0.8$, 1.6, 2.4, and 24 mm. The calculations of $C_{xy}(f)$ were performed using the fluctuating transverse velocity u' obtained from the TR-PIV measurements at $Re_4 = 10{,}622$. Figures 4.30 and 4.31 show that the coherent functions $C_{xy}(f)$ remained close to 1 for small separation distances η, at low frequencies up to 50 Hz for points P_{1-2}, up to 15 Hz for points P_{3-4} and up to 40 Hz for points P_{7-8}. This observation indicates that the low-frequency signal content at these points are linearly related. Similar findings were found in Romano [1995], and Nguyen and Hassan [2017a]. These authors discussed that the interactions of the mean flow, and the energy transfer process at the referenced points could occur at low frequencies. When the separation distances increased, however, the linear relations of the signal content were lost

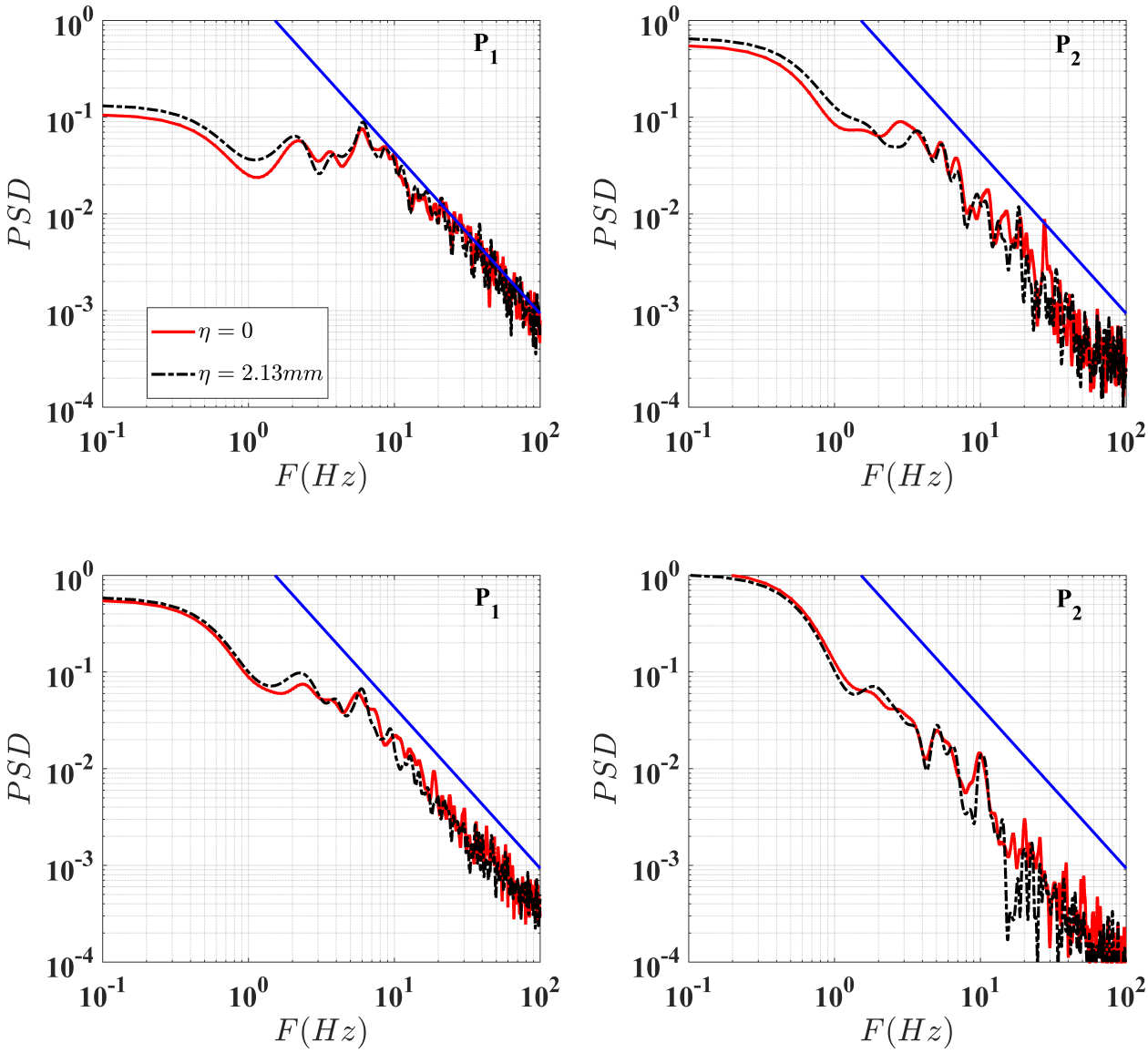

Figure 4.28: Spectral analysis of the fluctuating velocities u' (top) and v' (bottom) at points P_1 ($y/D_j = 1$), and P_2 ($y/D_j = 2$) computed from TR-PIV measurements at $Re_5 = 12{,}819$. PSDs computed at other points with a separation distance of $\eta = 2.13$ mm were overplotted. The straight line indicates $-5/3$ slope.

and the coherent function $C_{xy}(f)$ was reduced.

4.1.5 Computational fluid dynamics validation and verification (CFD V&V)

As was mentioned before, one of this research goals is to acquire high fidelity data urgently needed for validation of advanced computer codes. The flow should be fully

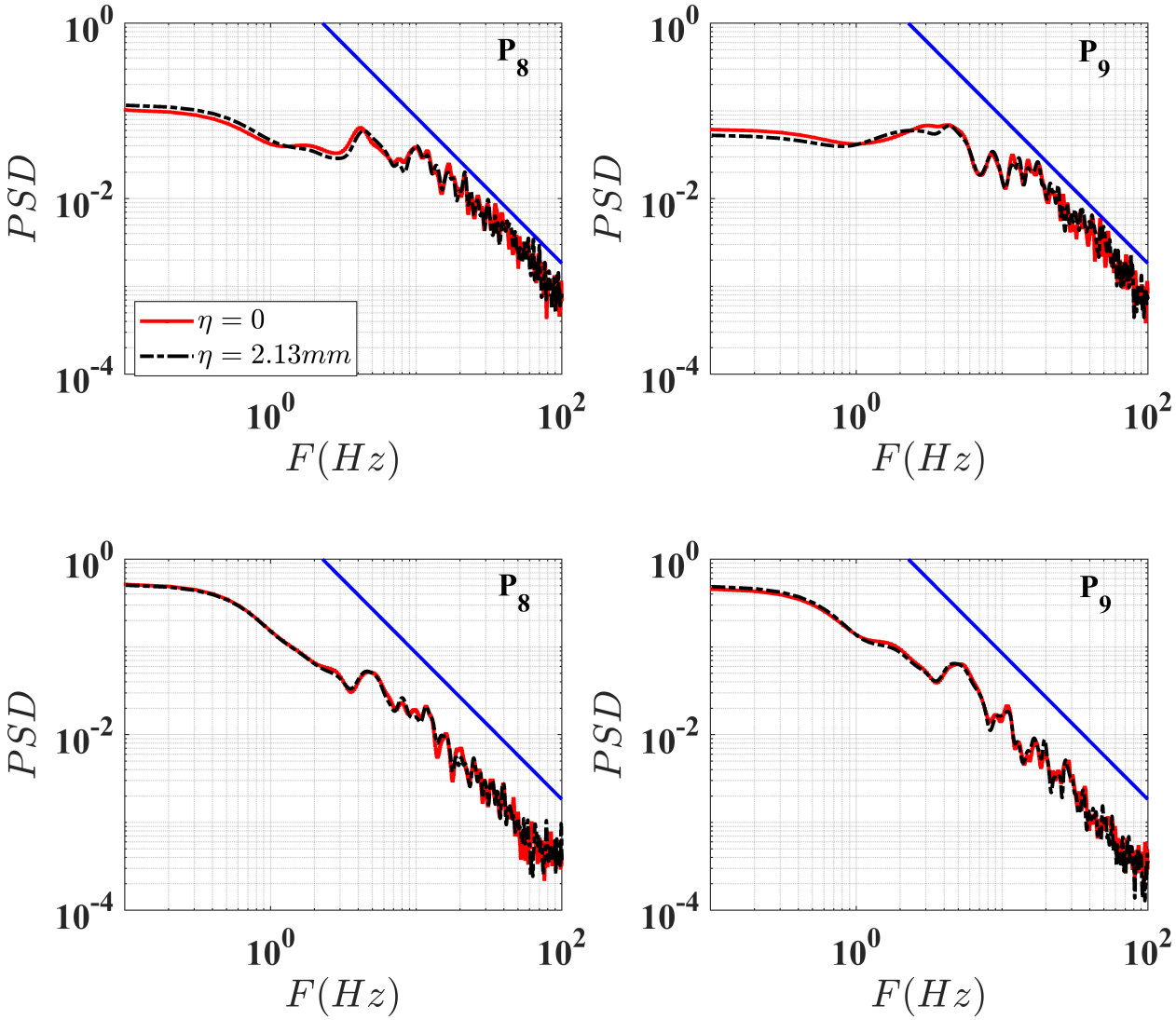

Figure 4.29: Spectral analysis of the fluctuating velocities u' (top) and v' (bottom) at points P_8 ($y/D_j = 8$), and P_9 ($y/D_j = 9$) computed from TR-PIV measurements at Re_5 = 12,819. PSDs computed at other points with a separation distance of $\eta = 2.13$ mm were overplotted. The straight line indicates $-5/3$ slope.

developed inside the coolant channel pipe to accurately simulate the flow coming into the upper plenum from the core. A TR-PIV experiment was performed by adding an extending acrylic tube at the upper plenum inlet. Figure 4.32, a is showing the diagram of the extending tube. It is made by acrylic to visualize the flow during the TR-PIV experiment, and Figure 4.32b shows the mean Color contours of the mean velocity magnitude. A data was extracting

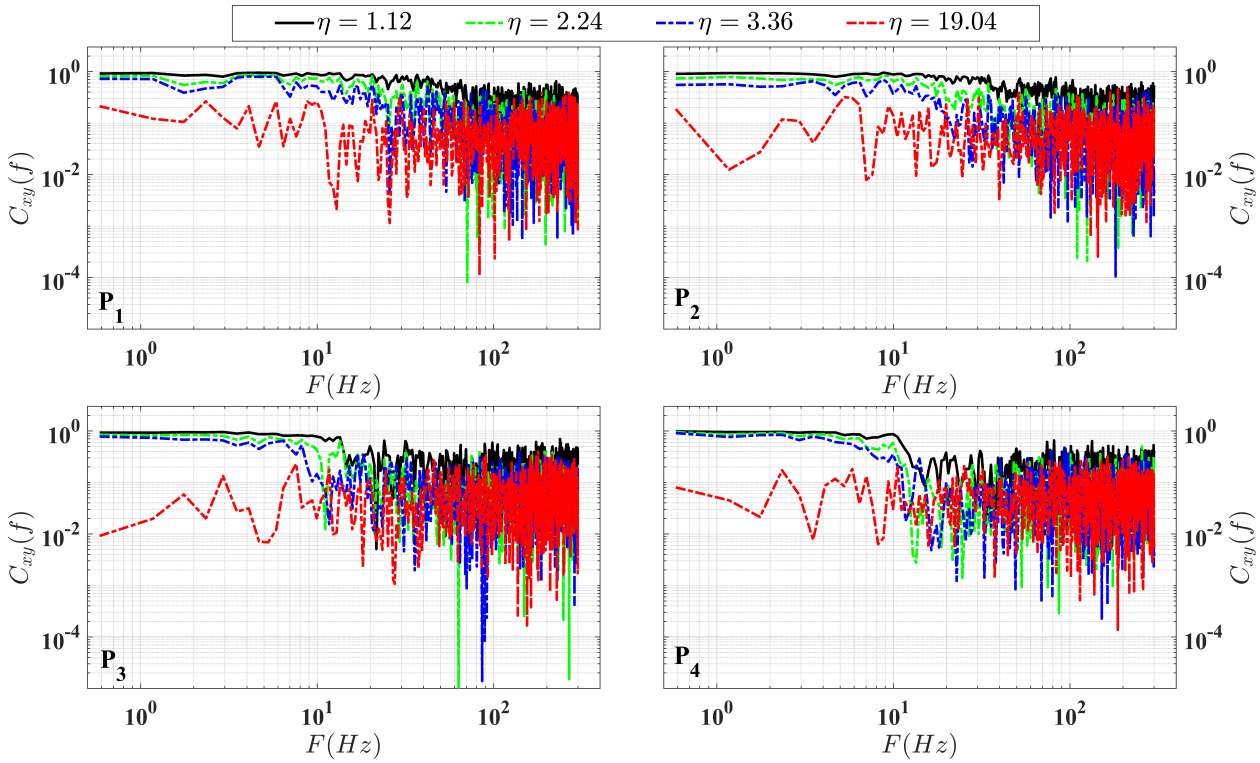

Figure 4.30: Squared coherent functions computed at points P_{1-4} and other points with separation distances of $\eta = 1.12$, 2.24, 3.36, and 19.04 mm. Values of $C_{xy}(f)$ were computed by using the fluctuating velocity u' from TR-PIV measurements at $Re_4 = 10{,}622$.

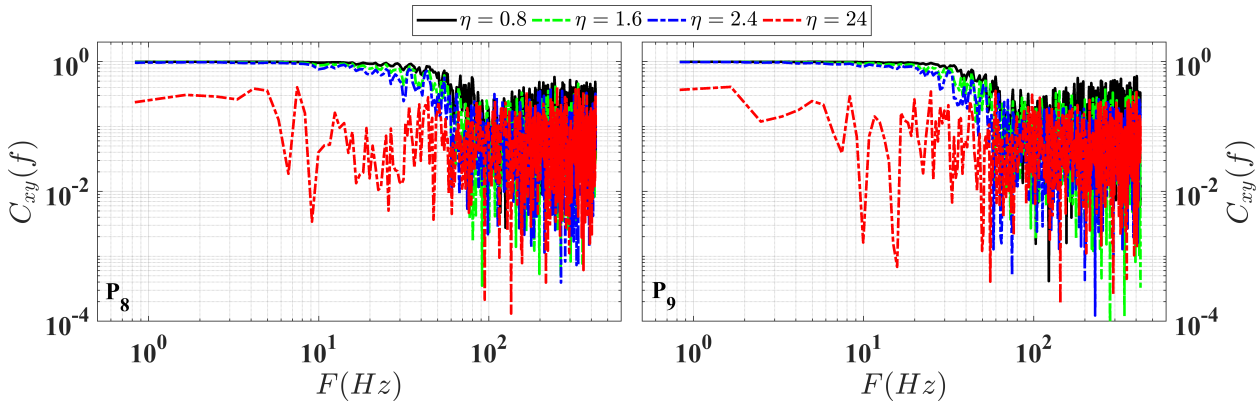

Figure 4.31: Squared coherent functions computed at points P_8 and P_9 and other points with separation distances of $\eta = 0.8$, 1.6, 2.4, and 24 mm. Values of $C_{xy}(f)$ were computed by using the fluctuating velocity u' from TR-PIV measurements at $Re_4 = 10{,}622$.

and interpolate it at $y/D_j = 10$ to plot the horizontal and vertical velocities, Figures 4.32c and d. The results show the flow inside the coolant channel is fully developed before coming inside the upper plenum

4.2 Results from the P-LIF Measurements

The single plume, non-isothermal, case is driven by the bounce of the source, meaning that heat is applied to the core and natural circulation forces the flow to mix with the cold fluid at the upper plenum. Fluid temperature, because of this, changes and study of temperature differences are critical. One way to measure the temperature is using the P-LIF technique. Note that this was used only for the non-isothermal case as the isothermal case has no temperature change. The test was done on the full half of the upper plenum at measurement area 3 (Figure 3.2a).

4.2.1 Convergence of statistical results computed from P-LIF Measurements

A total of 50,000 instantaneous temperature fields was obtained, representing four tests each with 12,500 temperature fields.The same approach is used as in section 4.33. The $\epsilon_{N_{1-3}}$ was defined as the absolute differences between the statistical values computed using $N_1 = 10{,}000$, $N_2 = 20{,}000$, $N_3 = 40{,}000$, and those computed using N_{max} temperature snapshots. Figure 4.33 shows the the convergence of the statistical results at several horizontal lines from $y/Dj = 1$ to $y/D_j = 9$. The shaded areas show the normalized absolute differences and for a better visitation; they were multiplied by arbitrary factors, $m = 10$. This shows that as the number of images are increasing the error is decreasing. Also, for N_3 the absolute error was significantly less than N_1 and N_2. It can be concluded that using 40,000 instantaneous temperature fields are enough for experiments such as this .

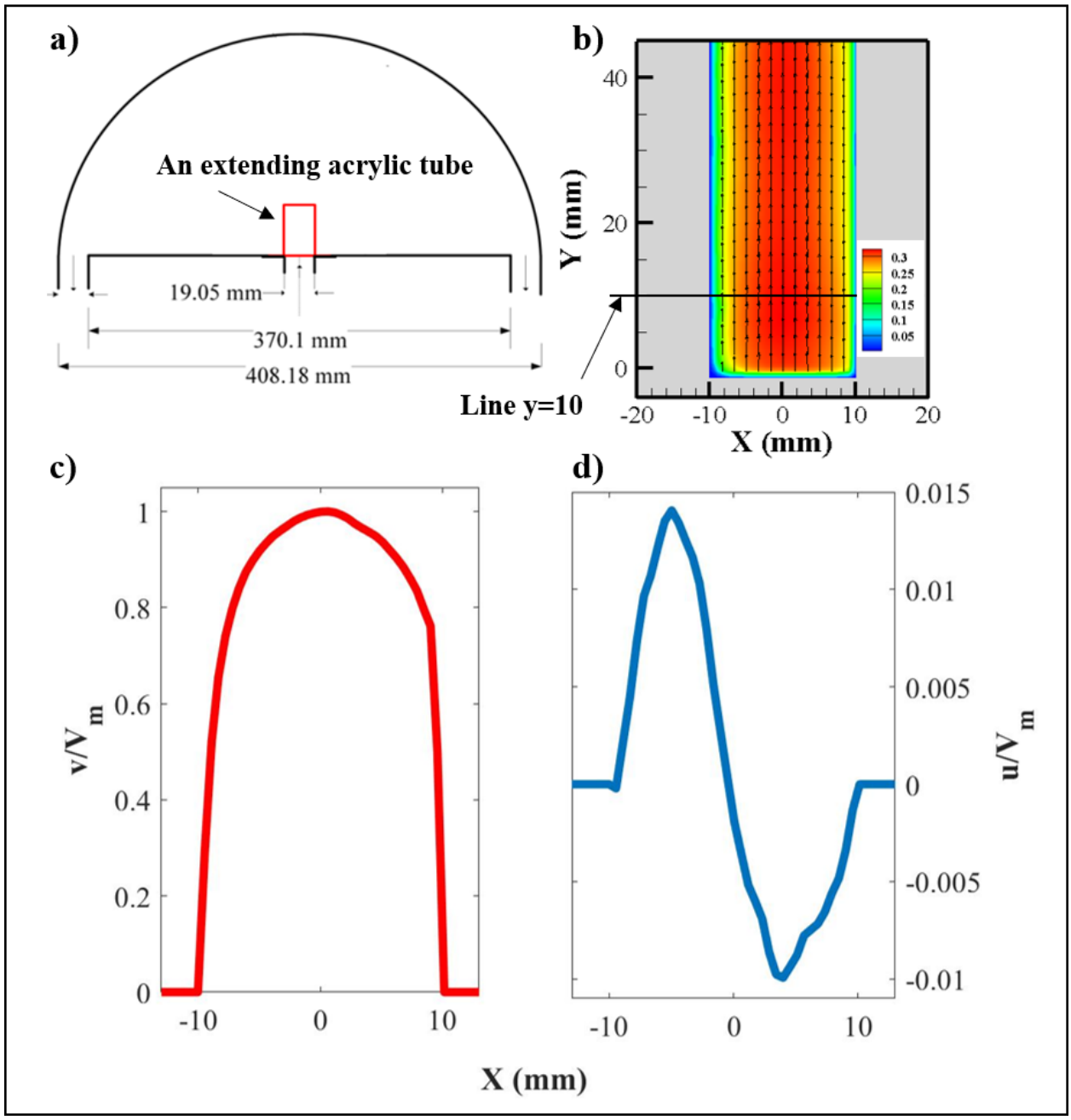

Figure 4.32: a) overview of the extending acrylic tube coming out of the upper plenum inlet, b) Color contours of the mean velocity magnitude (m/sec), c) Profile of normalized mean vertical velocity v/V_m obtained from TR-PIV measurements at horizontal line $y/D_j = 10$ (m/sec), and d) the profile for the horizontal velocity u/V_m.

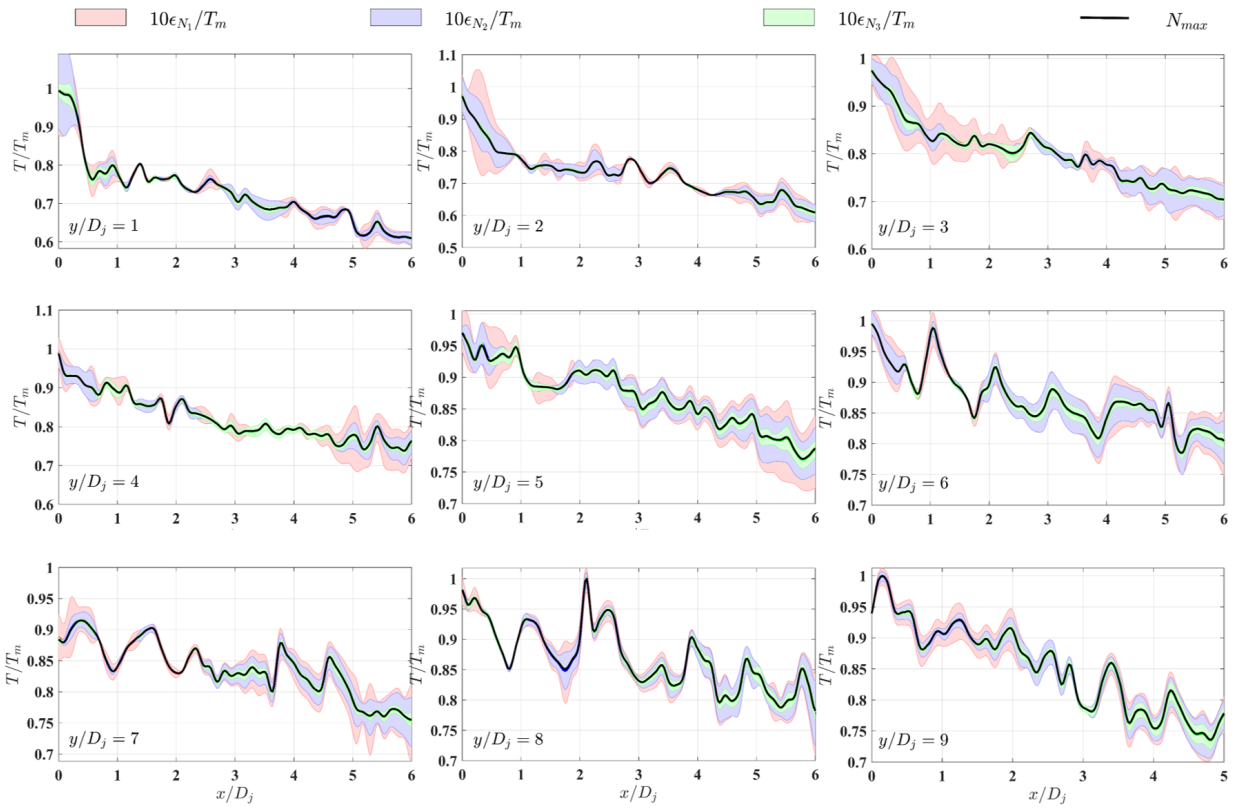

Figure 4.33: Convergence of P-LIF statistical results for the non-isothermal single plume. Profiles of normalized temperatures T/T_m, were computed along the lines from $y = Dj = 1$ to $y/Dj = 9$. Shaded colors show the normalized absolute differences $\epsilon_{N_{1-3}}/T_m$ between the statistics computed using N_{1-3} and those using the entire N_{max} snapshots. Note that the shaded areas were amplified by $m_{=}10$ to aid visualization

4.2.2 Statistical Results from the P-LIF Measurements

Figure 4.34 shows the ensemble-averaged temperature field in the upper plenum obtained from PLIF measurements of a single plume. The highest temperature is located near the upper plenum, from $y/D_j = 0$ to $y/D_j = 1.5$, at $40°C$. The temperature decreased downstream rapidly. We do not see any major difference in temperature far from the plume inlet. This might be because the flow is slow and the upper plenum volume is high, causing the flow to cool quickly after entering the upper plenum. The flow exits the upper plenum

at near room temperature. Moreover, stripes can be seen in the Figure 4.34 and this occurs because of the reflection of the laser sheet from the bubbles; this was common for several other studies.

The interpolation of temperature profiles along the horizontal lines, $y/D_j = 0$ to $y/D_j = 9$ are plotted in Figure 4.35, which shows the profile of mean temperature from P-PLIF measurements for a single plume mixing in the upper plenum. The profile from $y/D_j = 0$ to $y/D_j = 4$ shows the same trend, with maximum temperature at the center of the core inlet and a quick drop in temperature toward the end of the core, $x/D_j = 1$. After that, we see a slow decrease in temperature. However, the trend differs downstream from $y/D_j = 4$ to $y/D_j = 7$ where temperature follows a linear decrease. The profiles of $y/D_j = 8$ and 9 show a decrease, then an increase and another decrease. This pattern in the temperature could be from the effect of the upper plenum wall, where hot flow is coming back and increasing the temperature in that location.

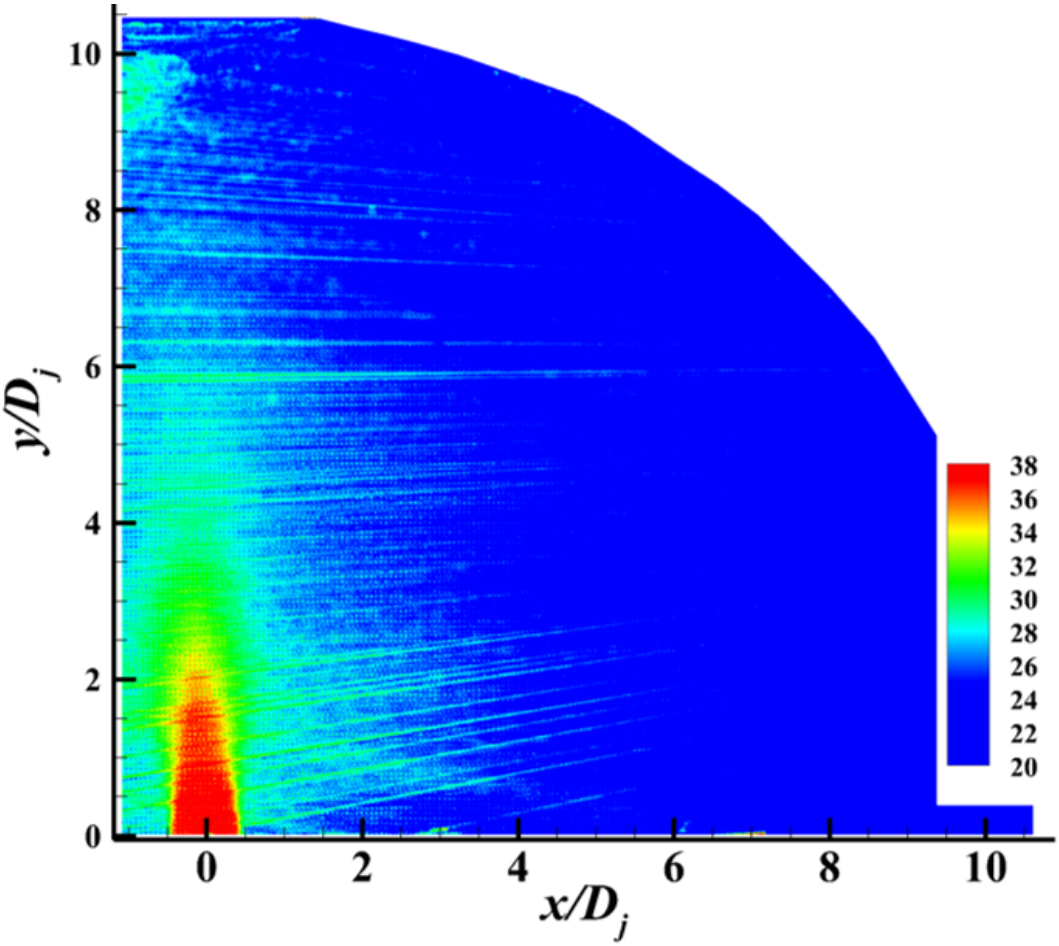

Figure 4.34: Ensemble-averaged of the temperature field in the upper plenum obtained from PLIF measurements of a single plume, in $^{\circ}C$ unit

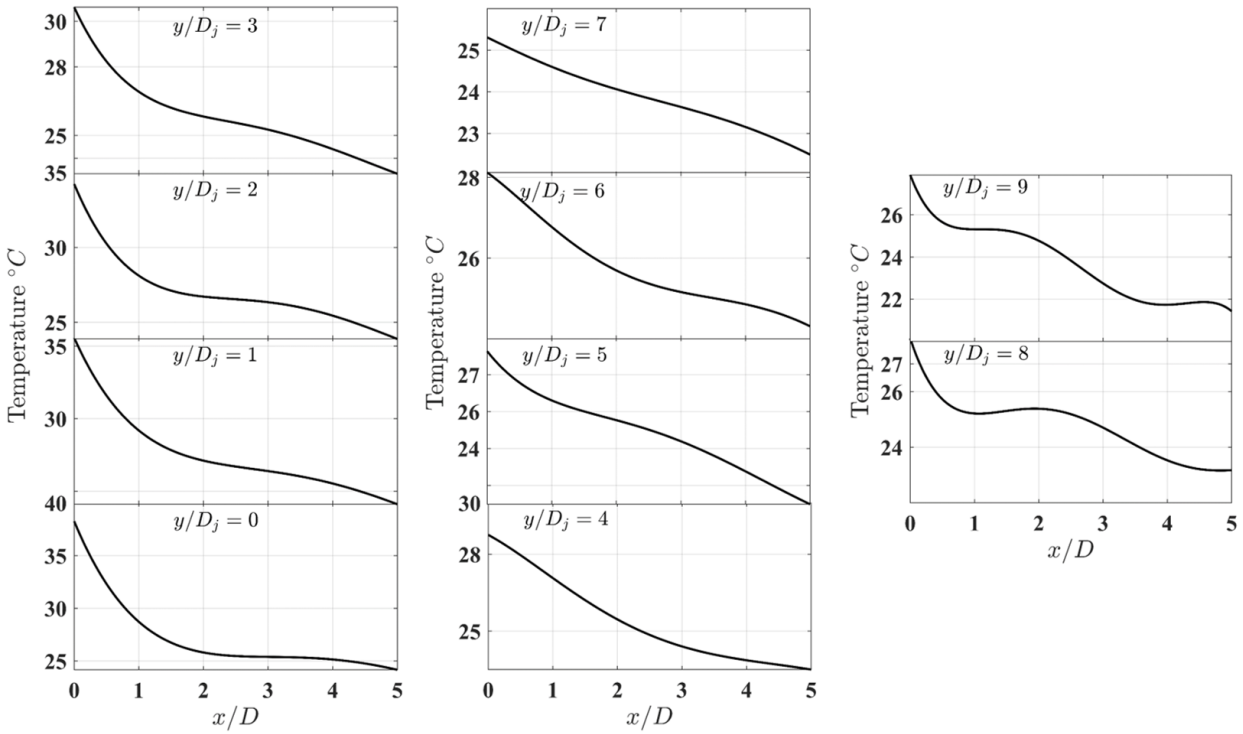

Figure 4.35: Profile of mean temperature from P-PLIF measurements of a single plume mixing in the upper plenum. Results were interpolated to horizontal lines $y/D_j = 0$ to $y/D_j = 9$.

5. CONCLUSIONS AND FUTURE WORK

5.1 Conclusions

I have presented TR-PIV measurements of a single jet and plume impinging and mixing in the upper plenum of a 1/16th scaled HTGR for two main cases. The first was the isothermal case for five different Reynolds numbers ranging from 3,413 to 12,819. The second case was the non-isothermal case for Reynolds number 500. Several measurements areas were used to analyze and study flow behavior. From the velocity vector fields of two cases, flow statistics such as mean velocity, r.m.s. fluctuating velocity, and Reynolds stress were computed and discussed. The statistical profiles extracted from the TR-PIV measurements were assessed at different Reynolds numbers, and compared to statistical results obtained from previous single jet experiments most compatible to this study's experimental configurations.

The results of the single jet analysis indicate that in the region of $y/D_j = 0$ to 8, flows have similar characteristics to free jet flows. The effects of confinement and impingement are observed in the region of $y/D_j > 8$ and in the vicinity of the upper plenum top wall, where the flow started to decrease and change direction, and where stagnation region was formed. The v'_{rms} peaks occurred along the shear layers in the vicinity of the jet inlet, while the u'_{rms} peaks occurred farther downstream at $y/D_j = 2.3$, 4.99, and 7.45 for Reynolds numbers Re_1, Re_3, and Re_5. In addition, results from the single plume show that the maximum velocity of the plume is far from the plume inlet and that its velocity decreases downstream. A highly turbulent velocity v'_{rms} was observed near the plume inlet.

Decay profiles of local velocities along the jet centerline show a linear increase up to $y/D_j = 8$, where the profiles begin an exponential increase due to the effects of jet impingement on the top wall.

To gain insight into the characteristics of jet flow mixing within the upper plenum, an analysis of two-point turbulent velocity cross-correlations were performed for various spatial points along the jet shear layers and for the jet and the plume.

The integral length scales estimated from the two-point spatial cross-correlations depict a linear increase, indicating the generation, evolution and movement of spanwise vortices along the jet shear layers. The profiles of integral length scales start to decrease from $y/D_j = 9$ to 10 as the flow changed its direction from axial to transverse near the impinging wall. Both the isothermal and non-isothermal cases show the same trend but for the non-isothermal case, values were higher in magnitude at all locations than for the isothermal case.

Spectral analysis and calculations of squared coherent functions were performed on the fluctuating velocity of the TR-PIV vector fields. The computed square coherent functions exhibited high values for small separation distances, at lower frequencies of up to 50 Hz for points P_{1-2}, 15 Hz for points P_{3-4} and 10 Hz for points P_{8-9}..

Finally, the P-LIF measurements were done on the non-isothermal case to study temperature change during flow mixing in the upper plenum. Maximum temperature occurred close to the plume inlet with temperature decreases downstream.

5.2 Future work

These experimental results will be used to verify and validate a system of codes and CFD models. Further experimental measurements are needed. For non-isothermal case, more temperature profiles are needed. This could be done by using different experimental measurements such as using fiber optic to measure the temperature.

For both the isothermal and non-isothermal cases, more experimental work can be done for several jets arraignments. This research was done only to the study the behavior of a single jet. Twin, triple jets, and a single jet near the upper plenum sidewall can be performed to see the arraignment's effect on the flow mixing at the upper plenum.

BIBLIOGRAPHY

Adrian, R. J. [2005]. Twenty years of particle image velocimetry, *Experiments in fluids* **39**(2): 159–169.

Alkhudhiri, B. [2019]. *Temperature and Velocity Measurements in Sub-cooled Boiling Through a Vertical Rectangular Test Channel*, PhD thesis, Texas A&M University, College Station, Texas.

Alwafi, A. [2015]. *Investigation of the flow of the upper plenum of a scaled very high temperature reactor during a depressurized cooldown conduction accident*, Master's thesis, Texas A&M University, College Station, Texas.

Alwafi, A., Nguyen, T., Anand, N. and Hassan, Y. [2018]. Time-resolved particle image velocimetry measurements and proper orthogonal decomposition analysis of jet impingement in a HTGR upper plenum, *Transactions of the American Nuclear Society* **118**: 1120–1122.

Anderson, N., Hassan, Y. and Schultz, R. [2008]. Analysis of the hot gas flow in the outlet plenum of the very high temperature reactor using coupled relap5-3d system code and a cfd code, *Nuclear Engineering and Design* **238**(1): 274–279.

Ball, C., Fellouah, H. and Pollard, A. [2012]. The flow field in turbulent round free jets, *Progress in Aerospace Sciences* **50**: 1–26.

Ball, C. G. and Pollard, A. [2008]. A review of experimental and computational studies of

flow from the round jet, *Technical report*, Internal Report: Department of Mechanical and Materials Engineering, Queen's University.

Ball, S. J., Corradini, M., Fisher, S. E., Gauntt, R., Geffraye, G., Gehin, J. C., Hassan, Y., Moses, D. L., Renier, J.-P., Schultz, R. et al. [2008]. Next generation nuclear plant phenomena identification and ranking tables (pirts) volume 2: Accident and thermal fluids analysis pirts, *Technical report*, Oak Ridge National Laboratory (United States). Funding organisation: ORNL work for others (United States).

Boomsma, A., Bhattacharya, S., Troolin, D., Pothos, S. and Vlachos, P. [2016]. A comparative experimental evaluation of uncertainty estimation methods for two-component PIV, *Measurement Science and Technology* **27**(9): 094006.

Busco, G., Nguyen, T. and Hassan, Y. A. [2018]. Cfd study of the coolant flow mixing inside VHTR upper plenum, *Proceedings of the Meeting on Advances in Thermal Hydraulics ATH 18*.

Button, B. and Wilcock, D. [1978]. Impingement heat transfer—a bibliography 1890–1975, *Previews Heat Mass Transfer* **4**(3): 83–89.

Charonko, J. J. and Vlachos, P. P. [2013]. Estimation of uncertainty bounds for individual particle image velocimetry measurements from cross-correlation peak ratio, *Measurement Science and Technology* **24**(6): 065301.

Coolen, M., Kieft, R., Rindt, C. and Van Steenhoven, A. [1999]. Application of 2-d lif temperature measurements in water using a nd: Yag laser, *Experiments in Fluids* **27**(5): 420–426.

Corrsin, S. [1943]. Investigation of flow in an axially symmetrical heated jet of air.

dos Santos, A. A. C., Childs, M., Nguyen, T. D. and Hassan, Y. [2019]. Convergence study and uncertainty quantification of average and statistical piv measurements in a matched refractive index 5× 5 rod bundle with mixing vane spacer grid, *Experimental Thermal and Fluid Science* **102**: 215–231.

Dowling, D. R. and Dimotakis, P. E. [1990]. Similarity of the concentration field of gas-phase turbulent jets, *Journal of Fluid Mechanics* **218**: 109–141.

Eckstein, A. and Vlachos, P. P. [2009a]. Assessment of advanced windowing techniques for digital particle image velocimetry (dpiv), *Measurement Science and Technology* **20**(7): 075402.

Eckstein, A. and Vlachos, P. P. [2009b]. Digital particle image velocimetry (dpiv) robust phase correlation, *Measurement Science and Technology* **20**(5): 055401.

EIA [2019]. International energy outlook 2019 with projections to 2050, *Technical report*, Office of Energy Analysis, U.S. Department of Energy.
URL: *https://www.eia.gov/outlooks/ieo/*

Estrada-Pérez, C. E., Hassan, Y. A. and Tan, S. [2011]. Experimental characterization of temperature sensitive dyes for laser induced fluorescence thermometry, *Review of Scientific Instruments* **82**(7): 074901.

Falchi, M. and Romano, G. P. [2009]. Evaluation of the performance of high-speed piv compared to standard piv in a turbulent jet, *Experiments in Fluids* **47**(3): 509–526.

Fellouah, H., Ball, C. and Pollard, A. [2009]. Reynolds number effects within the development region of a turbulent round free jet, *International Journal of Heat and Mass Transfer* **52**(17-18): 3943–3954.

Fiedler, H. E. [1998]. Control of free turbulent shear flows, *Flow Control*, Springer, pp. 335–429.

Gardon, R. and Akfirat, J. C. [1965]. The role of turbulence in determining the heat-transfer characteristics of impinging jets, *International journal of heat and mass transfer* **8**(10): 1261–1272.

Geers, L. [2004]. *Multiple impinging jet arrays: an experimental study on flow and heat transfer*, PhD thesis, Delft University of Technology, Delft, Netherlands.

George, W. K. [1989]. The self-preservation of turbulent flows and its relation to initial conditions and coherent structures, *Advances in turbulence* **3973**.

Goth, N., Jones, P., Nguyen, T. D., Vaghetto, R., Hassan, Y., Salpeter, N. and Merzari, E. [2018]. Ptv/piv measurements of turbulent flows in interior subchannels of a 61-pin wire-wrapped hexagonal fuel bundle, *International Journal of Heat and Fluid Flow* **71**: 295–304.

Hassan, Y. and Philip, O. [1997]. A new artificial neural network tracking technique for particle image velocimetry, *Experiments in Fluids* **23**(2): 145–154.

Humphreys, W., Bartram, S. and Blackshire, J. [1993]. A survey of particle image velocimetry applications in langley aerospace facilities, *31st Aerospace Sciences Meeting*, p. 411.

Hussein, H. J., Capp, S. P. and George, W. K. [1994]. Velocity measurements in a high-reynolds-number, momentum-conserving, axisymmetric, turbulent jet, *Journal of Fluid Mechanics* **258**: 31–75.

Jahanmiri, M. [2011]. Particle image velocimetry: Fundamentals and its applications, *Technical report*, Chalmers University of Technology.

Jambunathan, K., Lai, E., Moss, M. and Button, B. [1992]. A review of heat transfer data for single circular jet impingement, *International journal of heat and fluid flow* **13**(2): 106–115.

Jones, B. J. [2010]. *Fundamental studies of thermal transport and liquid-vapor phase change using microscale diagnostic techniques*, PhD thesis, Purdue University, West Lafayette, Indiana.

Lee, J. and Lee, S.-J. [2000]. The effect of nozzle aspect ratio on stagnation region heat transfer characteristics of elliptic impinging jet, *International journal of heat and mass transfer* **43**(4): 555–575.

Martin, H. [1977]. Heat and mass transfer between impinging gas jets and solid surfaces, *Advances in heat transfer*, Vol. 13, Elsevier, pp. 1–60.

McCreery, G. E. and Condie, K. G. [2006]. Experimental modeling of VHTR plenum flows during normal operation and pressurized conduction cooldown, *Idaho National Laboratory, Idaho Falls, Idaho* **83415**.

McVay, K. L., Park, J.-H., Lee, S., Hassan, Y. A. and Anand, N. [2015]. Preliminary tests of particle image velocimetry for the upper plenum of a scaled model of a very high temperature gas cooled reactor, *Progress in Nuclear Energy* **83**: 305–317.

Milanovic, I. M. and Hammad, K. J. [2010]. PIV study of the near-field region of a turbulent round jet, *ASME 2010 3rd Joint US-European Fluids Engineering Summer Meeting collocated with 8th International Conference on Nanochannels, Microchannels, and Minichannels*, American Society of Mechanical Engineers, pp. 1353–1361.

Neal, D. R., Sciacchitano, A., Smith, B. L. and Scarano, F. [2015]. Collaborative framework for PIV uncertainty quantification: the experimental database, *Measurement Science and Technology* **26**(7): 074003.

Nguyen, D. T., Maher, B. and Hassan, Y. [2019a]. Effects of nozzle pressure ratio and nozzle-to-plate distance to flowfield characteristics of an under-expanded jet impinging on a flat surface, *Aerospace* **6**(1): 4.

Nguyen, D. T., Maher, B. and Hassan, Y. [2019b]. Effects of nozzle pressure ratio and nozzle-to-plate distance to flowfield characteristics of an under-expanded jet impinging on a flat surface, *Aerospace* **6**(1): 4.

Nguyen, T., Goth, N., Jones, P., Lee, S., Vaghetto, R. and Hassan, Y. [2017]. PIV measurements of turbulent flows in a 61-pin wire-wrapped hexagonal fuel bundle, *International Journal of Heat and Fluid Flow* **65**: 47–59.

Nguyen, T. and Hassan, Y. [2017a]. Stereoscopic particle image velocimetry measurements of flow in a rod bundle with a spacer grid and mixing vanes at a low reynolds number, *International Journal of Heat and Fluid Flow* **67**: 202–219.

Nguyen, T. and Hassan, Y. [2017b]. Stereoscopic particle image velocimetry measurements

of flow in a rod bundle with a spacer grid and mixing vanes at a low reynolds number, *International Journal of Heat and Fluid Flow* **67**: 202–219.

Nguyen, T., Kappes, E., King, S., Hassan, Y. and Ugaz, V. [2018]. Time-resolved piv measurements in a low-aspect ratio facility of randomly packed spheres and flow analysis using modal decomposition, *Experiments in Fluids* **59**(8): 127.

Nguyen, T., Muyshondt, R., Hassan, Y. and Anand, N. [2019b]. Experimental investigation of cross flow mixing in a randomly packed bed and streamwise vortex characteristics using particle image velocimetry and proper orthogonal decomposition analysis, *Physics of Fluids* **31**(2): 025101.

NIRS [2016]. Wishful thinking: the basis of new nuclear economics, *Technical report*, NUCLEAR INFORMATION AND RESOURCE SERVICE.

Nishino, K., Samada, M., Kasuya, K. and Torii, K. [1996]. Turbulence statistics in the stagnation region of an axisymmetric impinging jet flow, *International Journal of Heat and Fluid Flow* **17**(3): 193–201.

Oh, C. H., Davis, C., Siefken, L., Moore, R., No, H. C., Kim, J., Park, G. C., Lee, J. C. and Martin, W. R. [2006]. Development of safety analysis codes and experimental validation for a very high temperature gas-cooled reactor, *Technical report*, Idaho National Laboratory (INL).

Or, C., Lam, K. M. and Liu, P. [2011]. Potential core lengths of round jets in stagnant and moving environments, *Journal of Hydro-environment Research* **5**(2): 81–91.

Panchapakesan, N. and Lumley, J. [1993]. Turbulence measurements in axisymmetric jets of air and helium. part 1. Air jet, *Journal of Fluid Mechanics* **246**: 197–223.

Park, J. H. [2016]. *Natural Circulation in the Upper Plenum of a Scaled Model of a Very High Temperature Reactor in the Event of Loss-of-Coolant Accident*, PhD thesis, Texas A&M University, College Station, Texas.

Pauls, J. P., Bartnikowski, N., Jansen, S.-H., Lim, E. and Dasse, K. [2018]. Preclinical evaluation, *Mechanical circulatory and respiratory support*, Elsevier, pp. 407–438.

PIRT, H. C.-G. [2008]. Next generation nuclear plant phenomena identification and ranking tables (pirts).

Raffel, M., Willert, C. E., Wereley, S. and Kompenhans, J. [2013]. *Particle image velocimetry: a practical guide*, Springer.

Romano, G. [1995]. Analysis of two-point velocity measurements in near-wall flows, *Experiments in Fluids* **20**(2): 68–83.

Ross, D., Gaitan, M. and Locascio, L. E. [2001]. Temperature measurement in microfluidic systems using a temperature-dependent fluorescent dye, *Analytical chemistry* **73**(17): 4117–4123.

Ruiz, T., Sicot, C., Brizzi, L., Borée, J. and Gervais, Y. [2010]. Pressure/velocity coupling induced by a near wall wake, *Experiments in Fluids* **49**(1): 147–165.

Sakakibara, J. and Adrian, R. [2004]. Measurement of temperature field of a

rayleigh-benard convection using two-color laser-induced fluorescence, *Experiments in fluids* **37**(3): 331–340.

Schabel, W. and Martin, H. [2010]. *G10 Impinging Jet Flow Heat Transfer*, Springer Berlin Heidelberg, Berlin, Heidelberg, pp. 745–752.
URL: *https://doi.org/10.1007/978-3-540-77877-6*$_4$3

Sciacchitano, A., Neal, D. R., Smith, B. L., Warner, S. O., Vlachos, P. P., Wieneke, B. and Scarano, F. [2015]. Collaborative framework for PIV uncertainty quantification: comparative assessment of methods, *Measurement Science and Technology* **26**(7): 074004.

Sciacchitano, A. and Wieneke, B. [2016]. PIV uncertainty propagation, *Measurement Science and Technology* **27**(8): 084006.

Shukla, A. K. and Dewan, A. [2017]. Flow and thermal characteristics of jet impingement: comprehensive review, *International Journal of Heat and Technology* **35**(1): 153–166.

Sutton, J. A., Fisher, B. T. and Fleming, J. W. [2008]. A laser-induced fluorescence measurement for aqueous fluid flows with improved temperature sensitivity, *Experiments in Fluids* **45**(5): 869.

Tango, W. J., Link, J. K. and Zare, R. N. [1968]. Spectroscopy of k2 using laser-induced fluorescence, *The Journal of Chemical Physics* **49**(10): 4264–4268.

Thomson, S. and Maynes, D. [2001]. Spatially resolved temperature measurements in a liquid using laser induced phosphorescence, *J. Fluids Eng.* **123**(2): 293–302.

Timmins, B. H., Wilson, B. W., Smith, B. L. and Vlachos, P. P. [2012]. A method for

automatic estimation of instantaneous local uncertainty in particle image velocimetry measurements, *Experiments in Fluids* **53**(4): 1133–1147.

Uddin, M. and Pollard, A. [2007]. Self-similarity of coflowing jets: the virtual origin, *Physics of Fluids* **19**(6): 068103.

Viskanta, R. [1993]. Heat transfer to impinging isothermal gas and flame jets, *Experimental thermal and fluid science* **6**(2): 111–134.

Welch, P. [1967]. The use of fast fourier transform for the estimation of power spectra: a method based on time averaging over short, modified periodograms, *IEEE Transactions on audio and electroacoustics* **15**(2): 70–73.

Westerweel, J. [1994]. Efficient detection of spurious vectors in particle image velocimetry data, *Experiments in Fluids* **16**(3-4): 236–247.

Wilson, B. M. and Smith, B. L. [2013]. Uncertainty on PIV mean and fluctuating velocity due to bias and random errors, *Measurement Science and Technology* **24**(3): 035302.

WNA [2008]. The economics of nuclear power, *Technical report*, World Nuclear Association.

WNA [2019]. Nuclear power in saudi arabia, *Technical report*, World Nuclear Association.

Wygnanski, I. and Fiedler, H. [1969]. Some measurements in the self-preserving jet, *Journal of Fluid Mechanics* **38**(3): 577–612.

Yuu, S., Shimoda, F. and Jotaki, T. [1979]. Hot wire measurement in the interacting two-plane parallel jets, *AIChE Journal* **25**(4): 676–685.

APPENDIX A

UPPER PLENUM DRAWING

The Upper Plenum revised drawing is shown here; the dimensions are in inches and the material is clear acrylic.

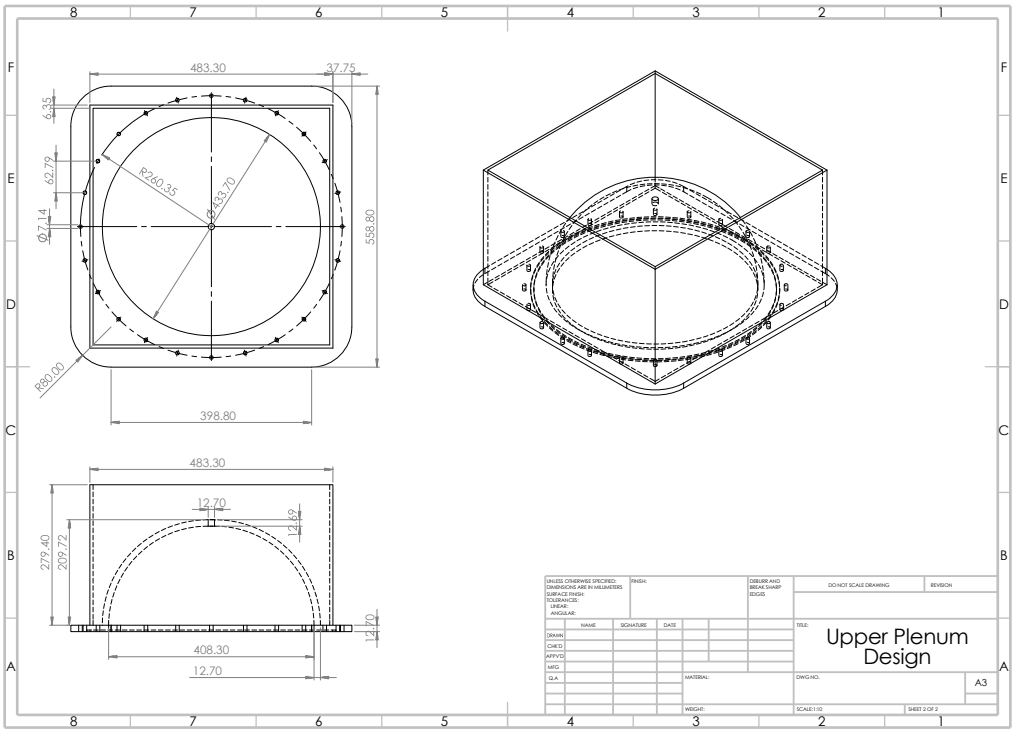

Figure A.1: The Upper plenum Hemisphere dimensions